Thermocatalytic Decomposition of Methane in a Gas Fluidized Bed Reactor

Citation for published version (APA):
Hadian, M. (2023). *Thermocatalytic Decomposition of Methane in a Gas Fluidized Bed Reactor: Numerical Modeling and Experimental Study*. [Phd Thesis 1 (Research TU/e / Graduation TU/e), Chemical Engineering and Chemistry]. Eindhoven University of Technology.

Document status and date:
Published: 17/10/2023

Document Version:
Publisher's PDF, also known as Version of Record (includes final page, issue and volume numbers)

Please check the document version of this publication:

• A submitted manuscript is the version of the article upon submission and before peer-review. There can be important differences between the submitted version and the official published version of record. People interested in the research are advised to contact the author for the final version of the publication, or visit the DOI to the publisher's website.
• The final author version and the galley proof are versions of the publication after peer review.
• The final published version features the final layout of the paper including the volume, issue and page numbers.

Link to publication

General rights
Copyright and moral rights for the publications made accessible in the public portal are retained by the authors and/or other copyright owners and it is a condition of accessing publications that users recognise and abide by the legal requirements associated with these rights.

- Users may download and print one copy of any publication from the public portal for the purpose of private study or research.
- You may not further distribute the material or use it for any profit-making activity or commercial gain
- You may freely distribute the URL identifying the publication in the public portal.

If the publication is distributed under the terms of Article 25fa of the Dutch Copyright Act, indicated by the "Taverne" license above, please follow below link for the End User Agreement:

www.tue.nl/taverne

Take down policy
If you believe that this document breaches copyright please contact us at:

openaccess@tue.nl

providing details and we will investigate your claim.

Download date: 17. Nov. 2023

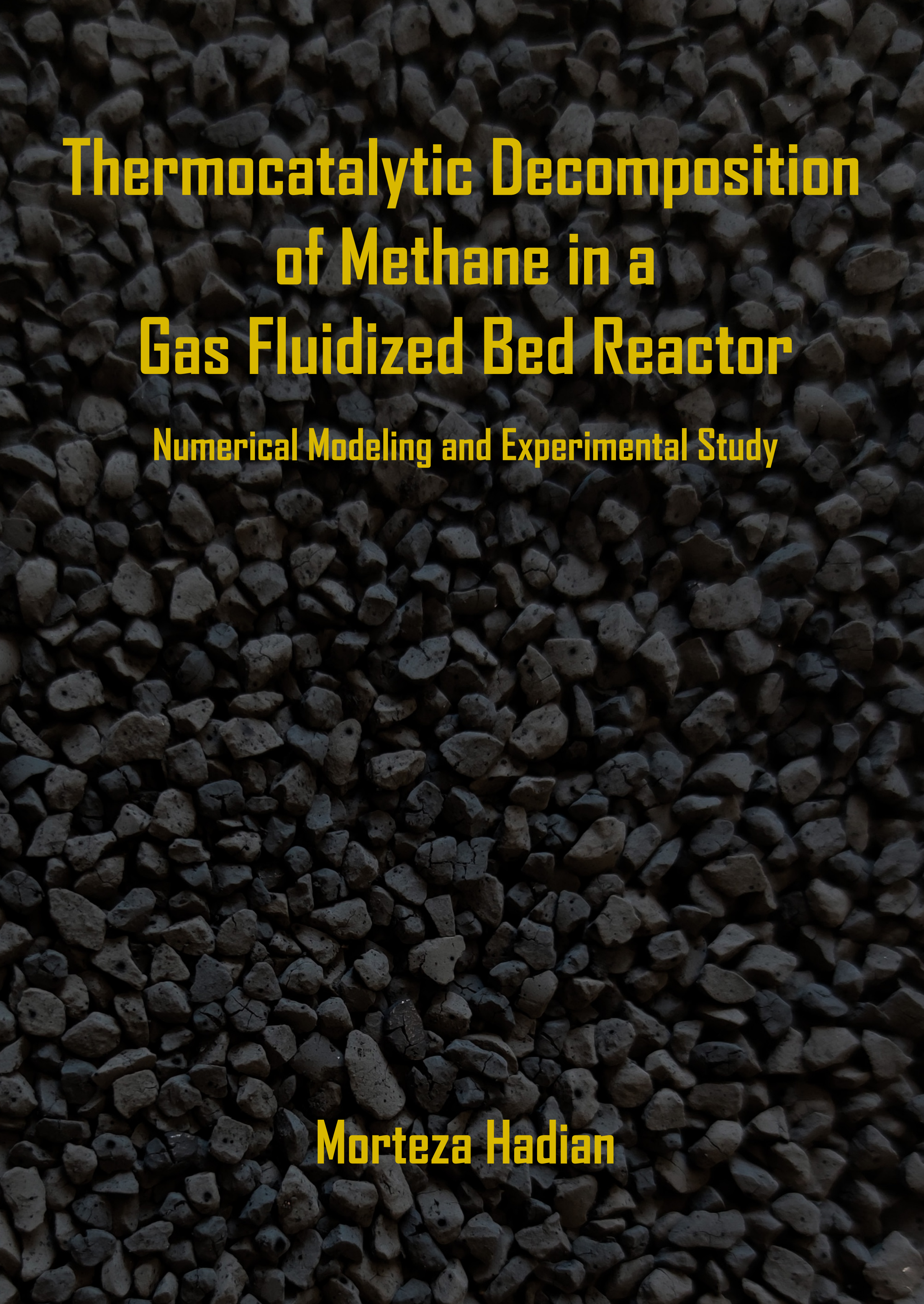

Thermocatalytic Decomposition of Methane in a Gas Fluidized Bed Reactor

Numerical Modeling and Experimental Study

Morteza Hadian

Thermocatalytic Decomposition of Methane in a Gas Fluidized Bed Reactor

Numerical Modeling and Experimental Study

PROEFSCHRIFT

ter verkrijging van de graad van doctor aan de
Technische Universiteit Eindhoven, op gezag van de
rector magnificus, prof. dr. S. K. Lenaerts, voor een
commissie aangewezen door het College voor
Promoties, in het openbaar te verdedigen
op dinsdag 17 october 2023 om 13:30 uur.

door

Morteza Hadian

geboren te Tabas, Iran

Dit proefschrift is goedgekeurd door de promotoren en de samenstelling van de promotiecommissie is als volgt:

Voorzitter:	prof.dr.ir. E. Rebrov
Promotor:	prof.dr.ir. J.A.M. Kuipers
Co-promotor:	dr. ir. K.A. Buist
Leden:	prof.dr. F. Gallucci
	prof.dr.ir. D.M.J. Smeulders
	prof.dr. P.E. de Jongh (Universiteit Utrecht)
	prof.dr. K. van Geem (Universiteit Gent)
	prof.dr.ir. M. van Sint Annaland

Het onderzoek dat in dit proefschrift wordt beschreven is uitgevoerd in overeenstemming met de TU/e Gedragscode Wetenschapsbeoefening.

This work is part of the Advanced Research Center for Chemical Building Blocks, ARC CBBC, which is co-founded and co-financed by the Netherlands Organisation for Scientific Research (NWO) and the Netherlands Ministry of Economic Affairs.

Copyright © 2023 by Morteza Hadian
All rights reserved. No part of the material protected by this copyright notice may be reproduced or utilised in any form or by any means, electronic or mechanical, including photocopying, recording or by any information storage and retrieval system, without the prior permission of the author.

A catalogue record is available from the Eindhoven University of Technology Library
ISBN 978-94-6469-577-9

Author email: mhadian1990@outlook.com
Cover designed, layout and graphics by: Morteza Hadian

Table of contents

Summary **IX**

Nomenclature **XVII**

1 General Introduction **1**

1.1 Decomposition of methane 2
1.2 Insight to the kinetics of the reaction 4
1.3 Reactor development and modeling 5
1.4 Objectives and outline 7

2 Experimental kinetic study of TCD in a fluidized bed **11**

2.1 Introduction 12
2.2 Experimental materials and methods 15
  2.2.1 Catalyst and reactants 15
  2.2.2 Experimental setup and procedure 15
  2.2.3 Product characterization methods 17
2.3 Reactor Model 17
  2.3.1 The plug flow reactor model 17
  2.3.2 Dynamic model 18
2.4 Results and discussion 19
  2.4.1 The effect of operating conditions 19
  2.4.2 Characterization of the products 28
  2.4.3 Kinetic Model 31
2.5 Conclusions and outlook 33

3 Numerical modeling of intra-particle phenomena and the catalyst particle growth - A MGM model 37
3.1 Introduction 38
3.2 Short review of kinetics in literature 40
  3.2.1 Initial reaction rate 40
  3.2.2 Deactivation factor 42
3.3 Model description 42
  3.3.1 Mass transfer 43
  3.3.2 Heat transfer 45
  3.3.3 Reaction kinetics 46
3.4 Verification of the model 47
3.5 Results and discussion 49
  3.5.1 Mass and heat transfer limitations 50
  3.5.2 Reaction kinetic effect 52
  3.5.3 Bulk gas concentration effect 52
  3.5.4 Temperature effect 54
  3.5.5 Effect of number of micro grain layers 54
3.6 Conclusions 55

4 Coupling of MGM with CFD-DEM 57
4.1 Introduction 58
4.2 Model description 60
  4.2.1 Gas phase modeling 60
  4.2.2 Discrete phase modeling 62
4.3 Verification and validation of the model 66
  4.3.1 Temperature coupling 66
  4.3.2 Components coupling 70
  4.3.3 Added/removed mass to/from the gas phase 72
  4.3.4 Integral mass balance of the reactor 73
4.4 Results and discussion 74
  4.4.1 Case description 74
  4.4.2 Particle size growth 75
  4.4.3 Fluidization regime 77
  4.4.4 Diffusion limitation 77
4.5 Conclusions 82

5 Numerical modeling of TCD in fluidized bed reactors 85
5.1 Introduction 86
5.2 Model description 88
5.2.1 Case description 91
5.3 Results and discussion 93
5.3.1 Catalyst deactivation 93
5.3.2 Particle size growth 95
5.3.3 Bed hydrodynamics 97
5.3.4 Gas conversion 99
5.3.5 Mass transfer limitations 102
5.4 Conclusions 103

6 Epilogue 105
6.1 Conclusions 106
6.1.1 Experimental study of TCD in an FBR 106
6.1.2 Numerical modeling of TCD 106
6.2 Outlook 108

References 111

Appendix A Weisz-Prater Criterion 125

Publications and Contributions 127

Acknowledgements 129

Curriculum vitae 135

Summary

The utilization of renewable sources is crucial for long-term sustainability, but in the meantime, methane remains a valuable energy carrier and feedstock. However, the emissions associated with methane usage must be mitigated through alternative approaches. ThermoCatalytic Decomposition of Methane (TCD) offers a way to produce carbon nanofibers (CNFs) and hydrogen without CO_2emissions. CNFs possess unique properties that make them suitable for various applications across different industries, such as composite materials, energy storage, catalysis, etc.

TCD involves the direct decomposition of methane via utilization of a catalyst and energy. Catalysts play a crucial role in enhancing the methane decomposition process by lowering the required reaction temperature, and synthesizing specific CNFs depending on the catalyst characteristics and operating conditions. Metal-based supported catalysts specially nickel/silica catalysts exhibit superior performance and activity. TCD is a one-step reaction process and with its potential economic and environmental advantages, is considered a promising approach for large-scale methane decomposition compared to alternative approaches. Despite the potential advantages and catalyst advancements, industrial-scale implementation of TCD faces significant challenges. Catalyst deactivation due to carbon encapsulation is a primary concern, as it affects the process performance. The carbon yield, defined as the grams of produced carbon per gram of fresh catalyst, ideally must be high, leading to an increased particle size and complexity in reactor design and operation. Successful large-scale application of TCD requires a comprehensive understanding of the chemical kinetics and hydrodynamics involved. The focus of this thesis is to make the first steps and try to obtain such knowledge via experimental and detailed modelling studies.

In **Chapter 1**, a general introduction of the different technologies for decomposition of methane is reported. Further it provides an overview of experimental studies on the kinetics of the TCD reaction. It also discusses the state-of-the-art, implications for reactor development and modeling. The main body of the thesis is structured in two sub-parts. The first part (i.e., Chapters 2) is dedicated to the experimental studies of TCD in a fluidized bed reactor (FBR), while the second part (i.e., Chapters 3, 4, and 5) is dedicated to modeling of TCD from particle scale, toward reactor scale. Chronologically, the completion and composition of Chapter 3 preceded that of Chapter 2, owing to the unfortunate delays in conducting experiments caused by the lockdown measures and other associated challenges during the initial stages of the COVID-19 pandemic. Consequently, the outcomes and observations of Chapter 2 were not incorporated or utilized in Chapter 3.

The first part of this thesis (i.e. **Chapter 2**) focuses on examining the reaction kinetics of TCD using a specially designed fluidized bed reactor, employing a nickel catalyst supported on silica. The chapter investigates the impact of various operating conditions, including temperature, methane and hydrogen concentrations, and space velocity (SV), on the performance of the catalyst. Three key parameters, namely the maximum reaction rate, lifetime, and carbon yield, are used to evaluate the catalyst's efficacy. Significant results were obtained, with carbon yields exceeding $70\,\mathrm{g_C/g_{cat}}$ and lifetimes surpassing 12 h at specific conditions (550 °C, 70 vol%CH_4-5 vol%H_2). The carbon product exhibits a distinctive fish bone structure. Notably, the investigation reveals that lower temperatures and the presence of modest amounts of hydrogen (10%) contribute to higher carbon yields. Conversely, reducing the methane concentration (resulting in a higher inert gas concentration) leads to decreased reaction rates, shorter lifetimes, and subsequently lower carbon yields. To determine the maximum reaction rate and associated deactivation factor, a dual kinetic approach has been employed. Furthermore, kinetic parameters have been estimated within the temperature range of 550 °C to 600 °C.

The second part of the thesis, including Chapters 3, 4, and 5 focuses on numerical models, adapted for catalytic reactions with solid formation, specially TCD. **Chapter 3** presents a comprehensive particle growth model due to formation of functional carbon on catalyst particles. The model integrates kinetic equations and deactivation rates, which have been obtained from relevant literature. To account for the combined effects of particle growth, kinetics, and internal heat and mass transfer, the Multi-Grain Model (MGM) is employed. The findings of the study indicate that, with the employed kinetic model, heat and mass transfer limitations do not significantly affect the carbon yield. However, as more active catalysts become accessible, these limitations are anticipated to become more significant. Temperature plays a crucial role as it regulates the kinetic rate, which subsequently influences the growth rate of carbon and, consequently, the deactivation of the catalyst. Therefore, selecting the optimal temperature for nano-carbon production within a reasonable process time is highly dependent on the choice of catalyst.

Chapter 4 integrates the MGM with Computational Fluid Dynamics - Discrete Element Method (CFD-DEM) approach. The model encompasses intra-particle phenomena with inter-particle and fluid-particle interactions within the reactor. This comprehensive framework treats each individual particle as a distinct entity, considering temporal and spatial variations of the process conditions that affect particle properties. The model further investigates the influence of particle growth on the characteristics of the fluidized bed reactor, particularly the hydrodynamic regime, fluidization behavior, and solids mixing. Notably, particle growth gives rise to a size gradient among the particles along the reactor's height. The coupled CFD-DEM-MGM approach enables the examination of both external and internal mass transfer limitations. Given the adopted reaction kinetics, growth rate, and particle properties, the internal mass transfer limitation emerged as a significant factor affecting the overall performance of the process.

In **Chapter 5**, the CFD-DEM-MGM model was employed to investigate the performance of two fluidized bed reactors, both sharing identical dimensions, in the context of TCD. Case-1 involved a batch reactor, while Case-2 incorporated continuous removal of catalyst particles from the bottom and simultaneous introduction of fresh particles from the side. The findings from this chapter demonstrated notable distinctions between the two reactor configurations. In the continuous reactor (Case-2), the limited residence time of catalyst particles resulted in reduced growth and deactivation compared to the batch reactor (Case-1). Conversely, the continuous reactor exhibited higher rates of carbon production and gas conversion due to the continuous introduction of fresh catalyst particles. Furthermore, it was observed that the presence of larger catalyst particles in Case-1 led to a significant decrease in the bubble formation frequency during the later stages of the process. In contrast, the continuous removal and introduction of particles in Case-2 prevented the formation of larger bubbles and enhanced horizontal solids mixing within the reactor. The study also emphasized the significance of internal diffusional limitations on the overall performance of the reactors.

Finally, **Chapter 6** concludes the main outcomes of this work and briefly discusses recommendation on TCD's prospects for the future.

Samenvatting

De toepassing van hernieuwbare grondstoffen is cruciaal voor de duurzaamheidsdoelstellingen op de lange termijn, in de tussentijd blijft methaan een waardevolle energiedrager en grondstof. De emissies die gekoppeld zijn aan het gebruik van methaan moeten daarentegen worden beperkt met behulp van alternatieve methoden. Thermo Katalytische Decompositie van Methaan (TCD) biedt een manier aan voor de productie van Carbon Nanofibers (CNFs) en waterstof zonder de uitstoot van CO_2. CNFs hebben unieke eigenschappen die ze geschikt maakt voor toepassing in verschillende industrieën als composiet materiaal, energie drager, katalysatoren etc.

TCD is een directe decompositie van methaan met behulp van een katalysator en energie. Het gebruik van een katalysator heeft een cruciale rol in het verbeteren van de decompositie van methaan door het verlagen van reactie temperatuur en maakt CNFs waarbij het type CNF afhankelijk is van de karakteristieke eigenschappen van de katalysator en de proces condities. Katalysatoren gebaseerd op overgangsmetalen op een support materiaal, meer specifiek nikkel/silica katalysatoren hebben een superieure opbrengst en activiteit. TCD is een 1-staps reactie en wordt vanwege de economische potentie en voordeel voor het milieu als een zeer veelbelovend proces voor het gebruik van methaan beschouwd ten opzichte van alternatieve processen. Ondanks de vele voordelen en de vooruitgang die geboekt wordt met katalysator ontwikkeling ondervindt de industriële toepassing van TCD nog de nodige uitdagingen. Deactivering van de katalysator doormiddel van inkapseling door koolstof formatie is van primair belang omdat het de prestaties van het proces direct beïnvloed. Het koolstofrendement, gedefinieerd als het aantal gram koolstof per gram katalysator is ideaal gezien hoog, wat leidt tot groeiende deeltjes grootte en een complex reactor ontwerp en operatie. Succesvolle toepassing van TCD op grootte schaal behoeft dus een totaal begrip

van de kinetiek en hydrodynamica van de reactor. De focus van dit proefschrift ligt in het verkrijgen van de eerste stappen van dat begrip via experimenten en gedetailleerde modelering studies.

In **Hoofdstuk 1** wordt een algemene introductie gegeven over de verschillende technologieën voor decompositie van methaan. Verder geeft het een overzicht van de experimentele studies naar de kinetiek van de TCD reactie alsmede een discussie van de state-of-the-art met betrekking tot de implicaties voor reactor ontwikkeling en modelering. Het hoofdgedeelte van het proefschrift bestaat uit twee onderdelen. Het eerste onderdeel (hoofdstuk 2) is toegespitst op het experimentele onderzoek naar TCD in een gefluïdiseerd bed reactor (FBR). Het tweede onderdeel (Hoofdstukken 3, 4 en 5) beschrijft de modellering van TCD van de schaal van de deeltjes tot de schaal van de reactor. Hoofdstuk 3 is chronologisch gezien eerder afgerond dan hoofdstuk 2. Door de beperkingen van de lockdown en de daarbij behorende uitdagingen konden de experimenten in het lab helaas niet tijdig plaatsvinden. Dit betekend dat de bevindingen van hoofdstuk 2 niet zijn opgenomen in de analyse van hoofdstuk 3.

Hoofdstuk 2 beschrijft de bevindingen van de experimenten naar de reactie kinetiek van TCD, met een nikkel op silica katalysator, in een speciaal daarvoor ontworpen gefluïdiseerd bed reactor. Dit hoofdstuk onderzoekt de impact van verscheidene operationele condities zoals; temperatuur, methaan en waterstof concentraties en ‘space velocity’ (SV) op de prestaties van de katalysator. Drie ‘key’ parameters zijn gebruikt om effectiviteit van de katalysator te karakteriseren; de maximale reactie snelheid, de levensduur en de koolstofopbrengst. Met een koolstofopbrengst rond de 70 $\mathrm{g_c/g_{cat}}$ en levensduur van 12 uur zijn zeer significante resultaten behaald voor sommige proces condities. Het koolstof product heeft een zeer distinctieve ‘fish bone’ structuur. Het onderzoek laat zien dat lagere temperaturen en de aanwezigheid van bescheiden hoeveelheden waterstof (10%) een veel hogere koolstofopbrengst opleveren. Daarentegen levert een verlaagde methaan concentratie (onder verhoogde inert concentratie) een lagere reactiesnelheid, verkorte levensduur en bijbehorend een lagere koolstofopbrengst op. Om de maximale reactiesnelheid en de bijbehorende deactivatiefactor te bepalen is een duale kinetiek aanpak toegepast. De bijbehorende parameters voor het kinetiek model zijn bepaald in het temperatuurbereik van 550-600 °C.

Het tweede deel, welke hoofdstukken 3, 4 en 5 omvat, focust op de numerieke modellen welke zijn ontwikkeld voor toepassing voor katalytische reacties met formatie van vaste stoffen, en specifiek TCD. **Hoofdstuk 3** beschrijft een groei model voor deeltjes doormiddel van formatie van functioneel koolstof op de katalysator deeltjes. Het model integreert de vergelijkingen voor de kinetiek met die voor deactivatie, welke zijn omschreven in de literatuur. Om rekening te houden met de combinatie van deeltjes groei, kinetiek en interne alsmede externe warmte en stoftransport is een ‘Multi-Grain Model’ (MGM) ontwikkeld. De bevindingen van dit onderzoek tonen aan dat met de gekozen modellen voor de kinetiek er geen massa en warmtetransport limitaties zijn, die de koolstofopbrengst significant beïnvloeden. Daarbij moet echter wel worden aangemerkt dat met een verhoging van het aantal 'active sites' deze limitaties wel degelijk een rol kunnen gaan spelen. Temperatuur heeft een cruciale rol in het reguleren van de reactiesnelheid, wat de groei van koolstof en daarmee de deactivatie van de katalysator beïnvloed. Het kiezen van een optimale temperatuur voor de productie van nano-koolstof binnen acceptabele procestijden is daarom sterk afhankelijk van de keuze van het soort katalysator.

Hoofdstuk 4 integreert het MGM met Computational Fluid Dynamics - Discrete Element Method (CFD-DEM). Dit model omvat zowel de fysica van de processen in de deeltjes alsmede de fysica van de processen tussen de deeltjes onderling en de interactie van de deeltjes met het gas in de reactor. Dit raamwerk beschouwd elk katalysator deelt als een aparte eenheid, wat het mogelijk maakt om het effect van de tijdsafhankelijke en ruimtelijke variatie van het proces op de deeltjes te onderzoeken. Dit model bestuurd het effect van de deeltjesgroei op het fluïdisatie gedrag en de invloed van deeltjesmenging. De deeltjesgroei leidt tot een gradiënt in de deeltjesgrootte over de lengte van de reactor. Het gekoppelde CFD-DEM-MGM model maakt het mogelijk om zowel de externe als interne massa transport limitaties te bestuderen. Met de gekozen reactie kinetiek, deeltjesgroei en deeltjes eigenschappen blijkt dat interne massa transport limitaties optreden die de algehele prestaties van het proces beïnvloeden. In **Hoofdstuk 5** is het CFD-DEM-MGM model toegepast voor TCD om de prestaties van twee gefluïdiseerde bed reactoren te bestuderen, beide hebben identieke dimensies. Case-1 is een batch reactor, terwijl in Case-2 continu katalysator deeltjes worden verwijderd vanuit de bodem van de reactor en verse deeltjes van de zijkant. De resultaten uit dit hoofdstuk laten een duidelijk verschil zien tussen de twee verschillende configuraties. In de continue reactor (case-2) de gelimiteerde verblijftijd van de katalysator deeltjes resulteert in een gereduceerde groei en deactivatie van de deeltjes in vergelijking met de batch reactor (Case-1). Daarentegen heeft de continue reactor een hogere snelheid van koolstof formatie en methaan conversie door de continue toevoeging van verse katalysator deeltjes. De aanwezigheid van grotere deeltjes in Case-1 resulteert in een significante afname van de vorming en frequentie van bellen. In contrast, in de continue reactor in Case-2 is door verversing van de deeltjes de formatie van grotere bellen gedempt en wordt een verbeterde deeltjes menging waargenomen. De studie laat verder zien dat in dit proces interne massa transport limitaties wel degelijk een effect hebben op de algehele prestaties van de reactor.

In **Hoofdstuk 6** worden de algemene conclusies en uitkomsten van dit werk besproken, tevens worden aanbevelingen gedaan voor verder onderzoek naar TCD.

Nomenclature

Variables

A	Heat or mass exchange area (m^2)
A_c	Cross section area of the reactor (m^2)
a_d	Exchange surface area per unit length of the reactor (m^2/m)
CF	Reaction rate unit conversion factor ($kg_{reactant} \cdot g_{cat} \cdot min/mol_{reactant}/m_{cat}^2/s$)
Cp	Specific heat capacity ($J/K/kg$)
$\mathscr{D}_f, D$	Diffusivity (m^2/s)
$D(\mathbf{r}-\mathbf{r_{p,a}})$	Distribution function (-)
$\langle d \rangle$	Sauter mean diameter (m)
dt	time step size (s)
h	Heat transfer coefficient ($W/m^2/K$)
$\mathbf{I}$	Unity tensor (-)
I	Moment of inertia ($kg \cdot m^2$)
k_m	Mass transfer coefficient (m/s)
K	Thermal conductivity in the gas phase ($W/m/K$)
k	Thermal conductivity in the porous particle ($W/m/K$)
$\hat{k}_1$	Reaction rate constant of pseudo-first-order reaction ($1/s$)
M	Mass concentration (kg/m^3)
m	mass (kg)
MW	Molar mass (kg/mol)
N	Number of particles (-)
n_p	number of particles per unit height of the reactor (-)

P	Pressure (Pa)
Q_p	Energy source term in the cell (W/m^3)
q_p	Heat transfer of particle (W)
$r(t)$	Actual reaction rate ($mol_{reactant}/g_{cat}/s$)
$r'(t)$	Pseudo-first-order reaction rate ($mol_{reactant}/m^3/s$)
r	Radial position in the particle (m)
$\mathbf{r}_{p,a}$	Position vector of particle a in reactor (m)
r_g	Radial position in the grain (m)
$r_{g,p}$	Position of the grain in the particle (m)
$R(r,t)$	Volumetric average rate of reaction ($kg/m^3/s$)
S_m	Mass source term in the cell ($kg/m^3_{cell}/s$)
$\mathbf{S}_p$	Momentum Source term in the cell ($kg \cdot m/m^3/s^2$)
t	time (s)
T	Temperature (K)
$\mathbf{T}$	Torque ($kg \cdot m^2/s^2$)
$\mathbf{u_f}$	Fluid velocity vector (m/s)
$\mathbf{v_p}$	Particle velocity vector (m/s)
V	Volume (m^3)
w	Rotational velocity ($1/s$)

Dimensionless numbers

Bi	Biot number (-)
Nu	Nusselt number (-)
Pr	Prandtl number (-)
Re	Reynolds number (-)
Sh	Sherwood number (-)
Sc	Schmidt number (-)

Greek letters

β	Inter-phase momentum exchange coefficient (-)
ε	Gas volume fraction (m^3_{gas}/m^3_{cell})
ρ	Density (kg/m^3)
μ	Shear viscosity ($Pa \cdot s$)

τ	Viscous stress tensor (Pa)
θ	Dimensionless temperature (-)
Ψ	Mass source term of each particle (kg/m^3/s)

Subscripts and Superscripts

f	Fluid
p	Particle
a	DEM particle a
i	Component i
in	Inlet
mix	Gas mixture
g	Grain in MGM
eff	Effective
$bulk$	Local conditions in the gas phase
s	Particle's surface conditions
$cell$	CFD computational grid cell
$prod$	Solid product layer in grains of MGM

To My Family

To Mahdokht

ای بی خبر بکوش که صاحب خبر شوی
تا راهرو نباشی کی راهبر شوی

حافظ

Oh, unaware soul, strive to be aware,
Leading without treading the road, how will you fare?

Hafez

1

General Introduction [1]

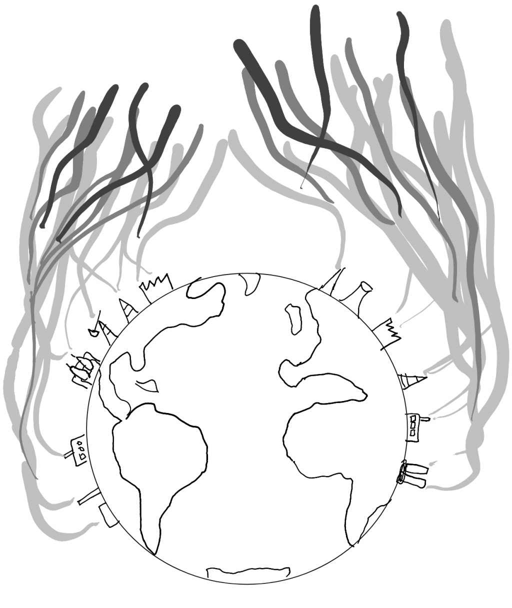

---

[1] This chapter is based on *Hadian, M., Buist, K. A., Kuipers, J. A. M. (2023), An overview of production of hydrogen and carbon nanomaterials via thermocatalytic decomposition of methane. Current Opinion in Chemical Engineering 2023*

1.1 Decomposition of methane

It is necessary to develop and exploit renewable energy sources as a long-term solution, however the use of energy carriers such as methane will last for some time [1–3]. The use of methane however, can be performed in a way that reduces emissions compared to conventional methods. Methane can be converted into hydrogen, which is one of the most promising energy carriers many industries rely on. Different routes of converting methane to hydrogen exist, the most common one being steam methane reforming that coproduces CO_2. The decomposition of methane (reaction 5.18) however, does not produce CO_2[4]. In this process, which can be performed by non-catalytic or catalytic approaches, methane is directly decomposed into its constituent elements, hydrogen and solid forms of carbon.

$$\mathrm{CH_4(g)} \longrightarrow \mathrm{C(s)} + \mathrm{H_2(g)} \qquad \Delta H_{(298K)} = +74.52\,kJ/mol \tag{1.1}$$

Thermal non-catalytic decomposition of methane, also termed methane pyrolysis or thermal decomposition, requires high temperatures, typically ≥1300 °C [5, 6]. The carbon formed in this process is mostly amorphous carbon and can be used as activated carbon, filler in rubber or in tires, or as pigment in different technologies [5, 7]. Utilization of a medium of molten metals in the reactor is suggested and studied in order to achieve a continuous process of non-catalytic decomposition of methane and convenient separation of deposited carbon in the reactor [4, 5, 7–9]. Other non-catalytic routes of the decomposition of methane involve the application of thermal or non-thermal plasma reactors. Several studies have already been reported on the decomposition of hydrocarbons and plasma reactors [10].

Utilization of a catalyst enhances the methane decomposition process. Firstly, the catalyst reduces the required temperature for the reaction ranging between 500 °C and 950 °C, making ThermoCatalytic Decomposition of methane (TCD) [1] less energy demanding. Secondly, specific forms of carbon nanomaterials can be generated, depending on the catalyst as well as the operating conditions employed [11]. These carbon nanomaterials, due to their intrinsic characteristics such as high conductivity, high tenacity and mechanical strength, and large specific surface area, can be valuable for different industrial applications such as building materials, catalytic materials and energy storage [12–14]. These advantages, together with the less complex gas separation unit for the products, make TCD an environmentally and economically promising approach [15]. Compared with plasma reactors, TCD is more suitable for large-scale decomposition of methane [10]. Therefore, TCD has gained significant attention from academia and industries in recent years [16].

---

[1] Also called Catalytic Decomposition of Methane (CDM)

Various catalysts are established for TCD that can be divided into two categories of metal-based and carbon-based catalysts. Carbon-based catalysts bring some advantages of availability, low cost and not requiring separation of products from the catalyst. On the other hand, metal-based catalysts have shown superior performance and activity. The most common materials for metal-based catalysts are nickel, iron and copper supported on alumina or silica in both single or bi-metallic modes [11, 16, 17]. Extensive studies have been performed on the different catalyst types, including the importance and the effects of catalyst preparation, including composition, reduction and calcination of the catalyst that provides an evaluation and review of the performance of the catalyst for application in TCD [10, 14, 16–19].

The reaction mechanism entails the initial molecular adsorption of methane, followed by a series of successive dehydrogenation reactions, resulting in the formation of isolated adsorbed carbon and hydrogen atoms. Subsequently, every two adsorbed hydrogen atoms combine to produce an H_2 molecule, which is then released from the catalytic surface. The carbon atom, on the other hand, dissolves into the metal catalyst and forms nanomaterials on the other side of the metal particle. If the decomposition step occurs faster than the diffusion and construction rate of carbon nano-structures, carbon atoms accumulate on the surface of the metal active site and deactivate it by encapsulation [20–22]. Therefore, the reaction initiates at the highest kinetic rate and it decays over time due to fewer available active site until full deactivation at a time considered to be the lifetime of the catalyst. The rate-limiting step of the reaction is considered to be the detachment of the first hydrogen from CH_4. If, due to local conditions, the transfer of carbon atoms through metal and subsequent formation of nanomaterials becomes slower than the decomposition reaction, then the carbon atoms accumulate on the surface of the metal and encapsulate it [6, 23–26]. Schoemaker et al. observed two different regimes of CNF formation at different temperature windows [22].

Despite all the potential advantages and catalyst developments, TCD is not yet used on an industrial scale and commercialized, stemming from the presence of considerable challenges ahead. The first challenge is deactivation of the catalysts due to encapsulation by carbon. The inclusion of the catalyst inside the product also forces one to design and select the catalyst according to the desired application of carbon nanomaterials. The carbon yield, which is defined as grams of produced carbon per gram of fresh catalyst used, can be as high as over $70\,\mathrm{g_c/g_{cat}}$. This excessive growth of the size of the particulate phase containing the catalyst introduces extra complexities to the reactor design and operation and requires a thorough understanding of the involved phenomena. The chemical kinetics of the reaction, as well as the hydrodynamics of the reactor, must be mastered to enable the large-scale industrial application of TCD.

1.2 Insight to the kinetics of the reaction

In TCD, the functionality and activity of the catalyst decline over time. It is of paramount importance to capture this process quantitatively. Kinetic studies revealed that the actual rate of the chemical reaction at a given time, $r(t > 0)$, is characterized by two distinct factors: the maximum reaction rate, r_0, and a deactivation factor that is dependent on time $a(t)$, Equation **??** [6, 13, 27–29].

$$r(t) = a(t) \times r_0 \tag{1.2}$$

Despite the numerous studies on the effect of different promoters and the performance of different catalysts at specific operating conditions, only a few works proposed a kinetic model of reaction rate and especially the deactivation factor. Saraswat et al. [25] have presented a comprehensive expression for the reaction rate, given by equation 3.8, that incorporates the impact of the partial pressures of both hydrogen and methane within the framework of the Langmuir-Hinshelwood model [25]. A variety of empirical or semi-empirical equations that have been formulated to describe the deactivation factor, $a(t)$, are summarized in reference [11]. Equation 1.4 obtained from a species balance on the catalyst's active sites, can describe nickel catalyst deactivation during TCD [6, 29]. Some in-situ TEM measurements have been done on TCD, showing the growth of carbon nanomaterials in real-time [30, 31]. Further in-situ TEM measurements would help to understand better the mechanisms of CNF growth and catalyst deactivation.

$$r_0 = \frac{k_1 P_{CH_4} - k_2 {P_{H_2}}^2}{\left(1 + k_3 P_{CH_4} + k_4 {P_{H_2}}^{0.5} + k_5 P_{H_2} + k_6 {P_{H_2}}^{1.5}\right)^2} \tag{1.3}$$

$$a(t) = \left(\frac{1}{1 - 0.5 k_d \left(k_{d,C} + k_{d,CH_4} P_{CH_4} + k_{d,H_2} P_{H_2}^{0.83} \right) t} \right)^{-0.8} \tag{1.4}$$

Most kinetic studies have been limited to micro-scale reactors under mild reaction conditions such as; low methane concentrations. Hadian et al. [29] conducted experiments on nickel-supported catalyst in a fluidized bed reactor, under conditions closer to what is required for industrial applications. Such studies can potentially offer valuable insights into the kinetic behavior of catalysts under more realistic operating conditions and aid in the development of efficient and cost-effective catalysts.

1.3 Reactor development and modeling

Muradov [32] compared different reactor types, such as Packed Bed reactor (PBR), Fluidized Bed Reactor (FBR), free-volume reactor, spouted-bed and tubular reactors, and concluded that FBRs are preferred for large-scale TCD, due to higher interphase mass and heat transfer rates and solids mobility [2]. Most conducted studies in recent years have been limited to small-scale PBRs under mild reaction conditions because of their relatively simple reactor design and operation. However, PBRs suffer from significant drawbacks for large-scale TCD, including a high probability of clogging, particle crushing, increasing pressure drop, and eventually fracturing the reactor's body due to the massive increase of the size of the catalyst particle over time [19, 32, 33]. Therefore, in order to discover the potential and limitations of TCD and to be able to step toward commercializing this process, it is imperative to research TCD in FBRs. Furthermore, the up-scaling of the reactor would result in the alienation of the reactor from differential conditions and introduces additional complexities arising from the interplay of multiple phenomena and emphasizes the necessity of studying TCD in FBRs. Figure 1.1 illustrates these different scales of phenomena in TCD reactor.

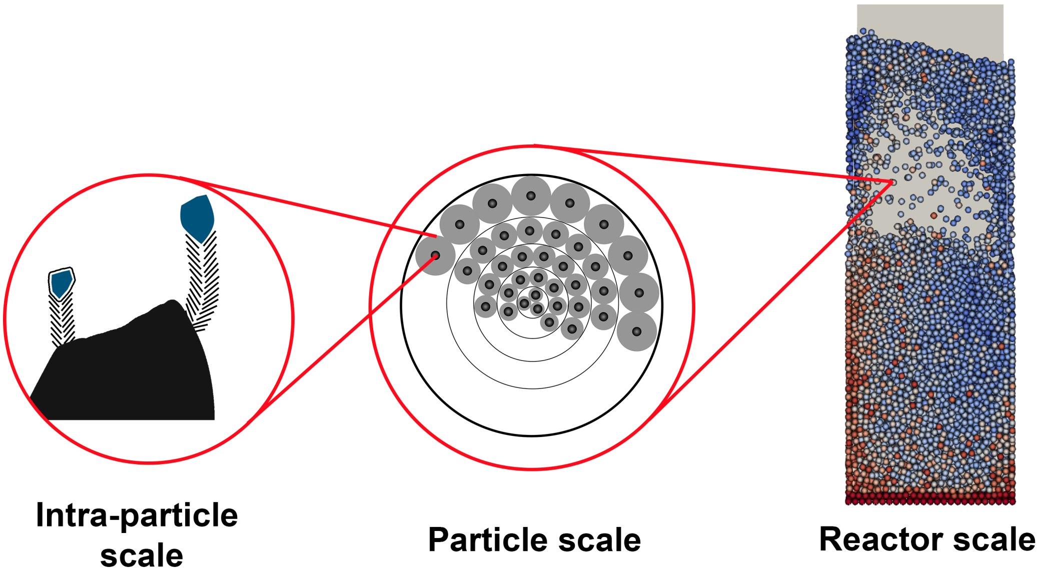

Fig. 1.1 Models of phenomena in TCD reactor at different scales. Intra-particle scale: intrinsic reaction and deactivation mechanism, Particle scale: mass and heat transfer and solid deposition, Reactor scale: momentum, mass and heat transfer in fluid phase and between fluid and solid phases.

Some studies have employed FBRs, mostly with fine catalyst powders. Using small catalyst particle sizes implies low gas space velocities (SV) to minimize particle carryover in the reactor. For instance, Torres et al. [34] and Pinilla et al. [35, 36] conducted experiments utilizing 20 g of fine catalyst powder in a fluidized bed, with space velocities limited to $0.2\,\mathrm{L_n/g_{cat}/min}$. Due to the higher minimum fluidization velocity of heavier particles, a limited space velocity fails to provide the required minimum fluidization velocity for grown particles.

To date, only a limited number of studies have explored reactor and process design solutions for addressing the challenges associated with TCD. Weizhong et al. [37] demonstrated that a two-stage FBR incorporating different temperatures and enabling solid transfer can significantly extend catalyst lifetime and improve methane conversion. The highest concentrations of the reactants are introduced into the stage with a lower temperature, which effectively limits the reaction rate and prolongs the catalyst's lifetime. The partially converted gas from the first stage then enters the high-temperature reactor, leading to an enhanced methane conversion. Similarly, Shah et al. [38] implemented a flow rate increase strategy to fluidize the bed at regular intervals in a PBR. Although this led to a temporary reduction in conversion efficiency, it effectively prevented clogging and allowed for the replacement of used catalysts, including solid products, with fresh catalysts.

Depending on the quality and desired application of the carbon nanomaterials as well as the type of catalyst, separation of solid products from the catalyst may be required or not [39]. Kaushal et al. [15] used a Ni-Cu bimetallic catalyst and proposed an ultrasonication method for the separation of carbon nanomaterials from the catalyst. The separated catalyst can be regenerated by oxidation of the catalyst (by air [15] or steam [40]). The activity recovery was very good after five cycles. Preliminary comparison of the obtained carbon nanomaterials with market prices showed that the potential price would be higher than 2 \$/g which makes TCD financially more favorable than steam methane reforming [15, 41]. More research is required on the possible approaches for CNF and catalyst separation is required. However, for certain applications, such as utilizing CNF as lightweight and robust building materials for vehicles, the separation of the catalyst and solid product may not be necessary, and a combination of CNF and the original catalyst can be employed. Nonetheless, further research is crucial in the pursuit of designing a catalyst with the utmost yield and the lowest metal loading.

Undoubtedly, further research is essential to develop efficient and effective TCD reactors and processes that can address the challenges associated with this technology. However, experimental evaluation and optimization of each proposed setup can be a time-consuming and expensive process. Therefore, the availability of multi-scale computational models becomes increasingly important for engineers to evaluate and optimize TCD reactors and processes. Such models can provide a cost-effective and efficient method to analyze the complex fluid dynamics and heat transfer mechanisms in TCD reactors. These models simulate the behavior of gas-solid flows and provide valuable insights into the flow characteristics, temperature distribution, and reaction kinetics within the reactor. Moreover, these models can facilitate the optimization of reactor design, catalyst selection, and operating conditions, enabling engineers to predict and control the performance of the TCD reactor.

Muradov [42] employed the well-known 1D Kunii-Levenspiel phenomenological bubbling fluidized bed model to scale-up a TCD reactor for the production of $50\,\mathrm{ton_{H_2}/day}$. The reported bed diameter of $4.2\,\mathrm{m}$ is comparable to that of industrial reactors used for fluid catalytic cracking and fluid coking, roughly indicating the technical feasibility of industrial-scale reactor design. Additionally, a 1D plug flow reactor model was used to represent the turbulent flow regime in the reactor [42]. Although these simple models provide a better understanding and overview of the potential of TCD, they suffer from many questionable assumptions and do not incorporate critical phenomena involved in TCD, such as the effect of particle growth on the hydrodynamics of the bed and the complete interplay between mass and heat transfer and chemical conversion.

1.4 Objectives and outline

This thesis focuses on performing TCD in an FBR and evaluating the importance and effects of operating conditions and reactor design through experimental and modeling studies. The primary objective of this thesis is to utilize fundamental principles of reaction and reactor engineering to explore TCD and expand the existing knowledge base, which has predominantly focused on the catalysis field.

This thesis consists of several chapters that investigate various aspects of TCD of methane. In **Chapter 2**, the reaction kinetics of TCD are examined using a specially designed fluidized bed reactor with a nickel catalyst supported on silica. The study explores the effects of operating conditions on catalyst performance, such as temperature, methane and hydrogen concentrations, and space velocity. Key parameters, including maximum reaction rate, lifetime, and carbon yield, are evaluated.

Chapters 3, 4, and 5 focus on numerical modeling approaches for catalytic reactions, particularly TCD. **Chapter 3** presents a particle growth model that considers the formation of functional carbon on catalyst particles. The Multi-Grain Model (MGM) incorporates the combined effects of particle growth, kinetics, and internal heat and mass transfer.

Chapter 4 integrates MGM with the Computational Fluid Dynamics - Discrete Element Method (CFD-DEM) approach, allowing for examining intra-particle phenomena and interactions within the reactor. The model investigates the impact of particle growth on the hydrodynamic regime, fluidization behavior, and solids mixing within the fluidized bed reactor.

In **Chapter 5**, the CFD-DEM-MGM model is used to study the performance of two fluidized bed reactors, one operating as a batch reactor and the other with continuous catalyst removal and introduction of fresh particles. The extent of growth and deactivation of catalyst particles, the hydrodynamic behavior of the bed, and gas conversion are compared between the two cases.

Finally, **Chapter 6** concludes the thesis by summarizing the main findings and discussing the future prospects of TCD.

هر خوشی فوت شد از تو مباش اندوهگین
کو به نقشی دیگر آید سوی تو می‌دان یقین

مولانا

Grieve not for what you lose in this domain,
In another guise, it shall return again.

Rumi

2

Experimental kinetic study of TCD in a fluidized bed[1]

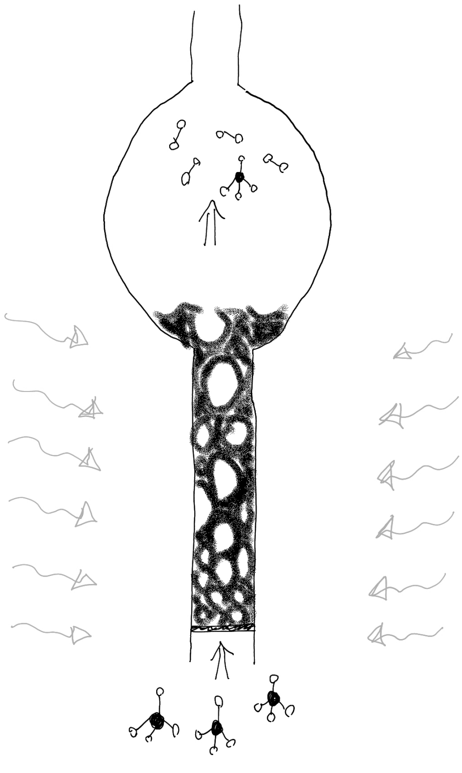

---

[1] This chapter is based on *Hadian, M., Marrevee, D. P. F., Buist, K. A., Reesink, B. H., Bos, A. N. R., Bavel, A. P., Kuipers, J. A. M. (2022), Kinetic study of thermocatalytic decomposition of methane over nickel supported catalyst in a fluidized bed reactor. Chemical Engineering Science,, 260, 117938 [29].*

Abstract

ThermoCatalytic Decomposition of methane (TCD) offers an interesting route to convert natural gas into hydrogen and functional carbon. In this chapter, the reaction kinetics of TCD is studied for a nickel-supported catalyst using a special fluidized bed reactor. The effect of operating conditions such as temperature, concentrations of methane and hydrogen and space velocity (SV) was studied on a commercial nickel catalyst on a silica support. The catalyst's performance was evaluated in terms of three parameters: maximum reaction rate, lifetime and carbon yield. Values up to and in excess of 70 $g_C/gcat$ and 12 h (at 550 °C and 70 vol.%CH_4-5 vol.%H_2) have been achieved for carbon yield and lifetime, respectively. The carbon product has fish bone structure. Our study has revealed that at lower temperatures and in the presence of small amounts of hydrogen ($\leq 10\%$) a higher carbon yield is obtained. A lower concentration of methane (a higher concentration of the inert) lowers the reaction rate, the lifetime and therefore, the carbon yield. A dual kinetic approach has been adopted to determine the maximum reaction rate and the associated deactivation factor. The kinetic parameters were estimated for the temperature range of 550 −600 °C.

2.1 Introduction

The destructive consequences of the climate change crisis followed by ongoing efforts toward emission-free technologies have instigated a growing interest in low CO_2 and CO_2-free hydrogen production [6, 14, 27, 43, 44]. Various approaches such as chemical looping reforming, steam methane reforming integrated with Carbon Capture and Sequestration processes (CCS), water splitting, and thermal and thermocatalytic decomposition of methane have been studied for this purpose. Among those, thermocatalytic decomposition of methane (TCD) is one the most promising [11]. A major advantage of TCD is the potential capability of producing highly valuable carbon nanomaterials instead of CO_2, next to hydrogen. The intrinsic characteristics of carbon nanomaterials make them suitable for many industrial applications such as building materials, semiconductors, catalytic materials and energy storage [12–14, 17]. In addition, TCD requires less complex down stream purification or separation units than conventional processes. These advantages make TCD an environmentally and economically attractive approach for CO_2-free hydrogen production [11]. In this chapter, a short overview of the methane decomposition reaction and its kinetics is presented. A more comprehensive literature study of the kinetic models for this reaction is given in chapter 3.

Methane is thermally decomposed to solid carbon and gaseous hydrogen in the absence of a catalyst or oxidizing agents at temperatures above 1300 °C (reaction 5.18). Alternatively, in TCD, a catalyst facilitates the same reaction at a much lower temperature (500 °C-950 °C) with the formation of nano-structured carbon materials. The structure of this material depends on operating conditions and foremost on the catalyst properties that are employed [11]. Nickel, iron, copper and carbon are the most studied active sites of the catalyst and among them, nickel on silica support, $Ni-SiO_2$, showed the highest methane decomposition activity [45–50].

$$CH_4(g) \longrightarrow C(s) + 2H_2(g) \quad \Delta H_{(298K)} = +74.52\,kJ/mol \tag{2.1}$$

A considerable amount of literature has been published on the preparation of single or bimetallic or carbonaceous catalysts. Their performance in very small lab-scale units and under mild reaction conditions have been established. Srilatha et. al [16] and Ashik et al. [14, 17] reviewed and compared these studies using carbonaceous and metallic catalysts, most of which have been employed in small-scale fixed bed reactors with up to 0.5 g of catalyst at limited space velocities and low concentrations of methane. Since the size of the catalyst particle in TCD increases over time due to carbon build-up, fixed bed reactors suffer from serious drawbacks such as a high probability of clogging, particle crushing, increasing pressure drop and fracturing the reactor's body. Therefore, fluidized bed reactors are preferred over fixed bed reactors for large-scale TCD. Indeed, few studies have used fluidized bed reactors or high space velocities (ratio of the total flow rate at normal conditions per gram of catalyst initially loaded), SV. For instance Torres et al. [34] performed experiments with 20 g of fine catalyst particles in a fluidized bed; however, the SV did not exceed $0.2\,L_n/g_{cat}/min$. Suelves et al. [51] used higher SV ($2\,L_n/g_{cat}/min$) in a fixed bed reactor that contained no more than 0.05 g of catalyst.

Alongside experimental parametric studies on the performance of the reaction, kinetic studies on TCD in a fixed bed reactor and mild conditions and the mechanism investigations of reaction 5.18 over metallic catalysts have been performed. These studies revealed that the actual rate of TCD is not constant over time and can be described by Equation 2.2, where r_0 is the maximum reaction rate and $a(t)$ is defined as the deactivation factor [6, 13, 27, 28]. In an earlier contribution, the authors summarized the kinetic studies and the proposed kinetic models, including the maximum reaction rate and deactivation factor of the catalyst [11]. Several researchers [6, 25] proposed a mechanism based on the molecular adsorption of methane followed by step-by-step dehydrogenation reactions until separate adsorbed atoms of carbon and hydrogen are obtained. The first dehydrogenation reaction was found to be the rate-limiting step. The remaining carbon atom of methane on the surface of the metal active site passes through the metal by diffusion and forms nanolayers of carbon on the other side. If the decomposition step occurs faster than the diffusion and construction rate of carbon nano-structures, carbon atoms accumulate on the surface of the metal active site and deactivate it by encapsulation [20, 21]. The maximum reaction rate is modelled by a Langmuir-Hinshelwood type equation that accounts for the thermodynamic equilibrium and the competition between hydrogen and methane adsorption over the active sites, as represented by equation 2.3. The semi-empirical deactivation factor expression is obtained from a species balance on the active sites of the catalyst, resulting in equation 2.4.

$$r(t) = a(t) \times r_0 \tag{2.2}$$

$$r_0[mol_{CH_4}/g_{cat}/min] = \frac{k(P_{CH_4}[atm] - {P_{H2}}^2[atm]/K_p)}{\left(1 + K_{H_2}{P_{H_2}}^{1.5}[atm] + K_{CH_4}P_{CH_4}[atm]\right)^2} \tag{2.3}$$

$$a = \left(\frac{1}{1 - 0.5k_d\left(k_{d,C} + k_{d,CH_4}P_{CH_4} + k_{d,H_2}P_{H_2}^{0.83}\right)t}\right)^{-0.8} \tag{2.4}$$

Although extensive research has been performed on catalyst preparation and reaction mechanism of TCD, very little is currently known about the feasibility of the TCD process in large-scale industrial fluidized beds at the harsh operating conditions encountered. The performance of the catalyst and the fluidized bed reactor need to be thoroughly investigated by performing experimental and numerical studies. This performance can be expressed in terms of the maximum reaction rate, r_0, the lifetime of the catalyst, LT, and carbon yield (the ratio of the mass of produced carbon to the initial mass of catalyst used, Equation 2.5), CY. The outline of this chapter is as follows: in section 2.2 we describe the experimental setup, materials as well as the adopted procedures. In section 2.3 we introduce the reactor model used for interpreting the experiments, whereas the results and discussion are given in section 5.3. Finally, in section 2.5 the conclusions are presented.

$$carbon\ yield\ (CY) = \frac{mass\ of\ produced\ carbon\ (g)}{initial\ mass\ of\ catalyst\ (g)} \tag{2.5}$$

2.2 Experimental materials and methods

2.2.1 Catalyst and reactants

In the experiments, a commercial catalyst made by BASF (Ni 5256 E RS) was used. The catalyst is originally designed as a hydrogenation fixed bed catalyst that contains 56% nickel on silica support and was supplied as extrudates and in a reduced and passivated state. Table 2.1 shows the characteristics of the fresh catalyst. All of the gases used in this study were at least 99.995% pure, supplied by Linde.

Table 2.1 Characteristics of the fresh catalyst and one sample of the used catalyst.

Parameter	Unit	Fresh catalyst	Used catalyst*
Specific surface area	m^2/g	267	115
Pore volume	$cm^3{}_{void}/g$	0.53	0.32
Material density	$g/cm^3{}_{material}$	3.6660	2.1797
Bulk density	$g/cm^3{}_{bulk}$	0.85	0.58
Particle diameter	μm	550	> 1000
Geldart classification	-	B	D

* at 550 °C and SV of 4.5 $L_n/g_{cat}/min$ of 100% CH_4

2.2.2 Experimental setup and procedure

The experiments were performed in a cylindrical quartz fluidized bed reactor equipped with a spherical free-board section, see Figure 2.1. The inner diameter and the height of the cylindrical part are 1 cm and 10 cm, respectively and the diameter of the free-board is 7.5 cm. The spherical free-board reduces the chance of entrainment by lowering the gas velocity and, at the same time, acts as an expansion space for the growing catalyst particles. The reactor was placed in an electric oven and the desired feed gas composition and flow rate were adjusted by calibrated Bronkhorst mass flow controllers. The local temperature in the reactor can be measured with the help of thermocouples. The outlet gas is transferred to a SICK gas analyzer model GMS815P (three measuring modules: Thermor, Oxor-P and Multor) for gas composition measurement after cooling down, Figure 2.2.

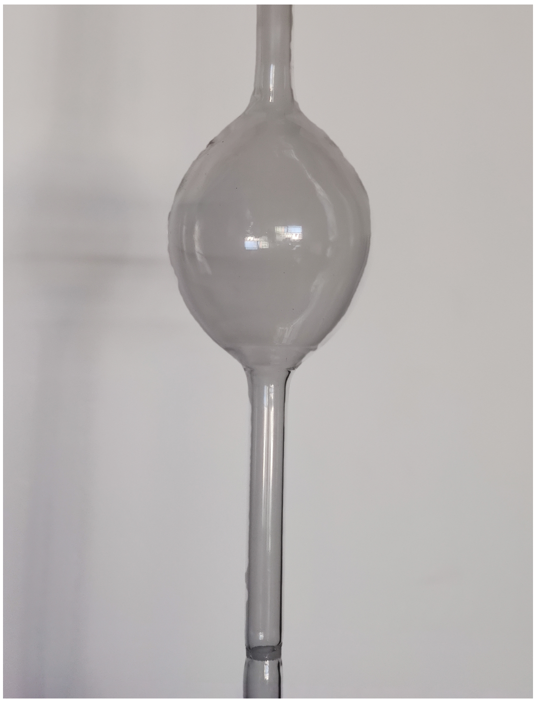

Fig. 2.1 The fluidized bed reactor with a spherical free-board section.

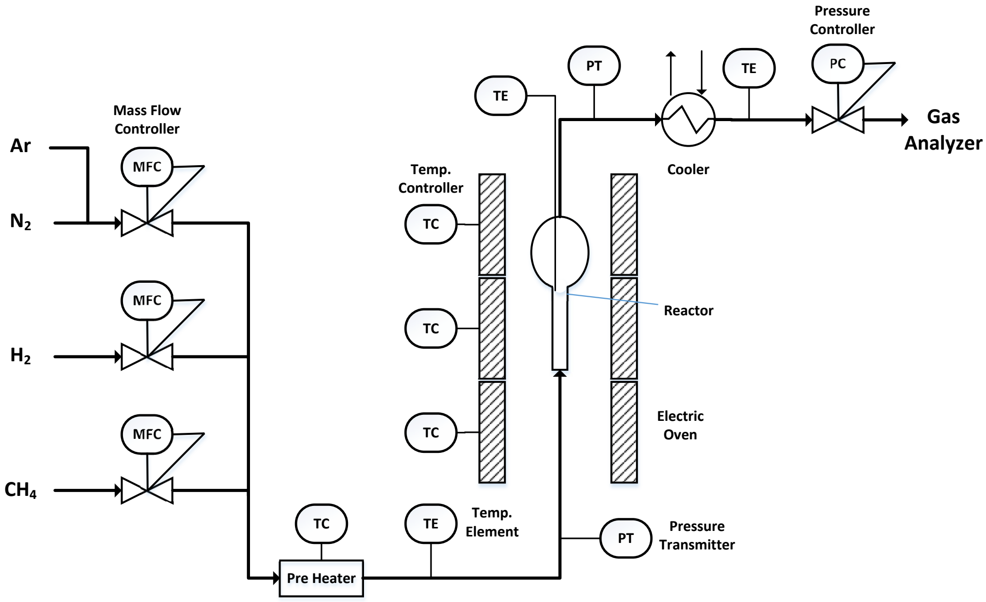
Pressure Controller
PC
TE
PT
TE
Gas Analyzer
Cooler
Mass Flow Controller
Ar
MFC
N_2
Temp. Controller
TC
Reactor
MFC
TC
H_2
Electric Oven
MFC
TC
CH_4
TC
TE
Temp. Element
PT
Pressure Transmitter
Pre Heater

Fig. 2.2 Schematic diagram of the experimental setup

In each experiment 1 g of crushed and sieved (500 −600 μm) catalyst was loaded into the reactor, unless otherwise stated (to examine the effect of the parameter). Prior to activation of the catalyst, the air in the porous catalyst particle was extracted by flowing 2 $\mathrm{L_n/g_{cat}/min}$ nitrogen to the reactor for 30 min. Subsequently the temperature of the reactor was increased to 250 °C by a ramp of 5 °C/min using 10 vol.%H_2 in the feed to actuate the catalyst. The catalyst was further reduced in 100 vol.%H_2 with the same ramp of temperature up to 500 °C. Afterward, the catalyst was heated up further in nitrogen. Once the reaction temperature was reached, 4.5 $\mathrm{L_n/g_{cat}/min}$ of the predefined gas composition of methane, hydrogen and the inert gas (nitrogen) was fed to the reactor, and the outlet composition was measured typically until the catalyst was fully deactivated. Finally, the reactor was cooled down and the product was collected and weighed.

2.2.3 Product characterization methods

BET surface area and pore volume measurements have been carried out for the used catalyst using Thermo Fisher Scientific Analyzer model Surfer. The oxidation temperature of the produced carbon was measured in the air via Thermo Gravimetric Analysis (TGA) to characterize the products. The surface composition of the fresh and used catalyst was analyzed by X-ray Photoelectron Spectroscopy (XPS) measurements on Thermo Scientific K-Alpha XPS with an Al source (1486.6 eV). The structure of carbon nanomaterials was obtained by performing Transmission Electron Microscopy (TEM) imaging of the samples of the products on a FEI cryo TEM TITAN 300 kV.

2.3 Reactor Model

2.3.1 The plug flow reactor model

The composition of the gas entering the reactor is known and the same as the predefined values for each experiment. However, as the gas passes through the reactor methane is consumed and hydrogen is produced. Therefore, the composition of the gas, and consequently the reaction rate, varies along the height of the bed, whereas only the outlet conversion can be compared with the experimental data. This conversion is calculated by a Plug-Flow Reactor (PFR) model, Equation 2.6. See Figure 2.3-a.

$$\frac{dX}{dw[g_{cat}]} = \frac{-r_0[mol/min/g_{cat}]}{F_{A_0}[mol/min]} \quad , \quad X(0) = 0 \tag{2.6}$$

where X is conversion, F_{A_0} is the molar flow rate of methane to the reactor, and dw is a fraction of the bed, such that the reaction can be considered constant over the fraction. r_0 is replaced by Equation 2.3. This differential equation is numerically integrated by Runge–Kutta fourth-order method (RK4). The equilibrium constant at the reaction temperature, K_p in equation 2.3, is calculated by equation 2.7 proposed by Kuvshinov et al. [52, 53].

$$K_p[atm] = 5.0215 \times 10^5 exp\left(-\frac{9.12 \times 10^4}{RT}\right) \tag{2.7}$$

The local partial pressures of methane and hydrogen are updated by Equation 2.8 and 2.9. Finally, the kinetic parameter of Equation 2.3 was fitted by comparing the conversion of the last section of the fluidized bed with the maximum conversion obtained from each of the experiments.

$$P_{CH_4} = \frac{(1-X)P_{CH_4}}{1+X} \tag{2.8}$$

$$P_{H_2} = \frac{2XP_{CH_4} + P_{H_2}}{1+X} \tag{2.9}$$

2.3.2 Dynamic model

Over time as the carbon products are being formed, the catalyst particles grow in size and weight with different rates. This growth can reach a point where some of the particles become too heavy to be fluidized by the available gas flow rate. Therefore, they settle down at the bottom of the reactor. These segregated particles are exposed to the fresh feed entering the reactor with a higher concentration of methane and lower concentration of hydrogen compared to the upper parts of the reactor. As a result, they grow faster and they also deactivate quicker than the rest of the particles. Over time more and more particles are segregated and deactivated until the whole bed is deactivated.

In order to predict the deactivation of the catalyst and determine the parameters of equation 2.4 it is crucial to model this complex behavior over time. In order to obtain a predictive model for the deactivation, the model described in section 2.3.1 is run for each time step starting from the beginning of the reaction until full deactivation. At the end of each time step, the total consumed methane and produced hydrogen and solid carbon are calculated and used to update the particle size. Then the minimum fluidization velocity of the particles is calculated for fine and coarse particles with equations 2.10 and 2.11, respectively [54].

$$Re_{p,mf} = [33.7^2 + 0.0408Ar]^{1/2} - 33.7 \tag{2.10}$$

$$Re_{p,mf} = [28.7^2 + 0.0494Ar]^{1/2} - 28.7 \tag{2.11}$$

where $Re_{p,mf}$ is the Reynolds number of the particles, equation 2.12, and Ar is the Archimedes number calculated by equation 2.13.

$$Re_{p,mf} = \frac{\rho_g u_{mf} d_p}{\mu} \tag{2.12}$$

$$Ar = \frac{d_p^3 \rho_g (\rho_p - \rho_g) g}{\mu^2} \tag{2.13}$$

By growing the particles the minimum fluidization velocity increases and the ratio of gas velocity to the minimum fluidization velocity, u/u_{mf} decreases. The moment that u/u_{mf} is not sufficient to maintain fluidization ($u/u_{mf} < 1.2$ this ratio is dependent on the reactor and particles properties), the bottom part of the bed is separated from the rest of the reactor (Figure 2.3-b), and the particles are not mixed with the top part anymore. The inflow of gas to the top part is higher due to the production of 2 moles of hydrogen for each mole of consumed methane in the segregated section. Therefore, the ratio u/u_{mf} can be high enough for the fluidization of the particles in the upper sections of the bed. Due to further growth of the particles, the segregated zone propagates along the reactor and eventually, the entire bed becomes segregated as shown in Figure 2.3-c.

This is a phenomenological 1D model representing the evolving reactor and therefore, radial difference, wall effect, channelization, and bubble formation are neglected. Before the particles in the first section start segregating, all the particles are fluidized and well-mixed in the reactor. Therefore, the particles grow at the same rate at this stage. Segregation only occurs if the carbon yield is high enough (mostly in cases with lower temperatures or if hydrogen is added to the feed). Due to segregation, particles are not mixed any more. The growth rate is higher at the bottom of the reactor but there the deactivation starts earlier.

2.4 Results and discussion

2.4.1 The effect of operating conditions

Many experiments were conducted by systematically altering the settings of operating temperature, gas concentrations, catalyst particle size and WHGV. All results were confirmed with at least one duplicate experiment. In these experiments depending on the settings lifetime varied from 5 min to longer than 12 h where the obtained carbon yield ranged between 0 g_C/g_{cat} to more than 70 g_C/g_{cat} (at 550 °C and 70 vol.%CH_4-5 vol.%H_2).

The max. conversion of the reactor was limited to about 20% because of the very high SV. It was observed that although at lower SV fluidization occurs with fresh catalyst particles

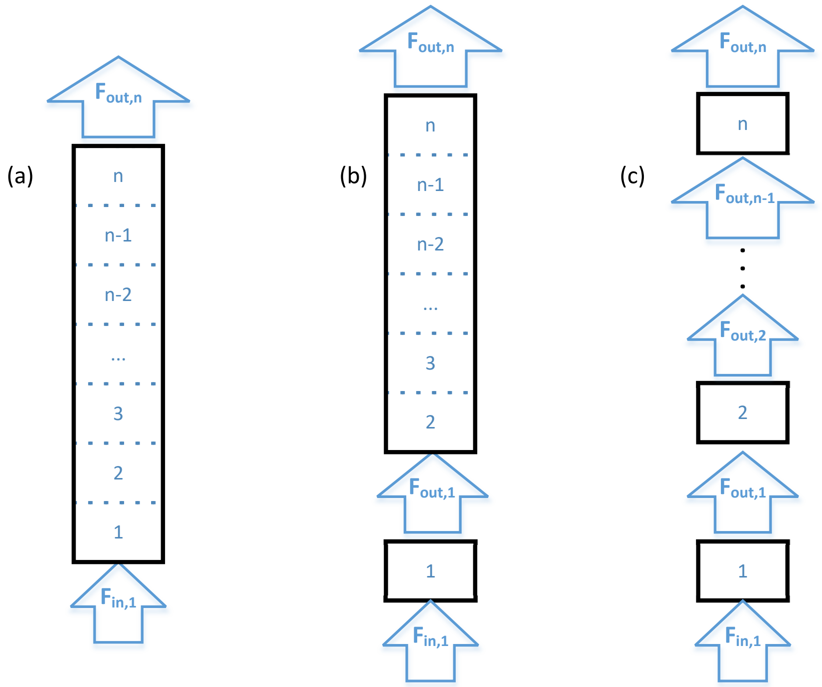

Fig. 2.3 The schematic of (a) the initial plug flow reactor model, (b) the reactor model when only the bottom section is segregated, (c) the reactor model when it is completely segregated.

($u_{mf} \approx 0.1\,\mathrm{m/s}$), the heavier and larger particles including the produced carbon (u_{mf} depends on the CY and it can exceed $2\,\mathrm{m/s}$ for the largest particles) cannot be fluidized and therefore leads to breaking the reactor. Therefore, the gas flow rate (and as a result, SV) is chosen to be high enough to mobilize the grown catalyst particles even after hours of carbon accumulation on them.

Operating temperature

Since the diameter of the reactor is relatively small and the consumed heat by the reaction is small compared to the heat supplied by the oven, temperature drop along the reactor was limited to a maximum of 17 °C (at maximum reaction rate at 600 °C and with a feed of 100 %CH_4). Figure 2.4 shows that the maximum reaction rate increases as the temperature is increased as expected. On the other hand, as can be seen in Figure 2.5-bottom, a high temperature has a negative effect on the lifetime of the catalyst. These findings are in agreement with literature findings [6, 11]. The carbon yield is a parameter that integrates both the effects of the maximum reaction rate and the catalyst's lifetime. Therefore, as shown in Figure 2.5-top from 550 °C to 650 °C a shorter lifetime can overcome the higher reaction rate and carbon yield is significantly lower. However, at lower temperatures the carbon yield is more affected by lower maximum reaction rate and there is an optimum temperature for carbon yield between 500 −550 °C, balancing initial reaction rate and lifetime of the catalyst.

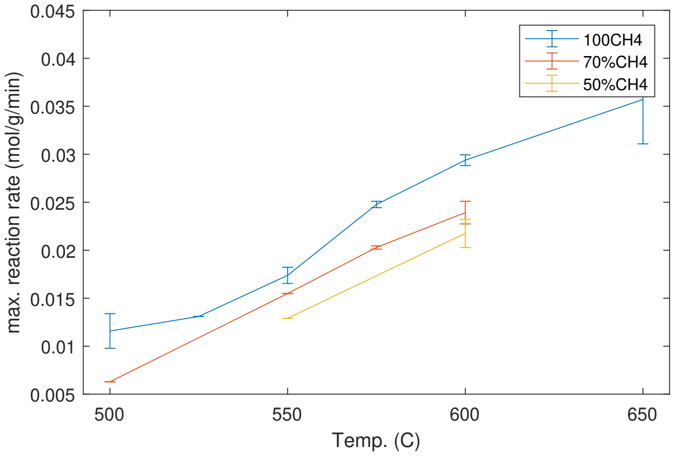

Fig. 2.4 The effect of temperature on the maximum reaction rate of the reaction.

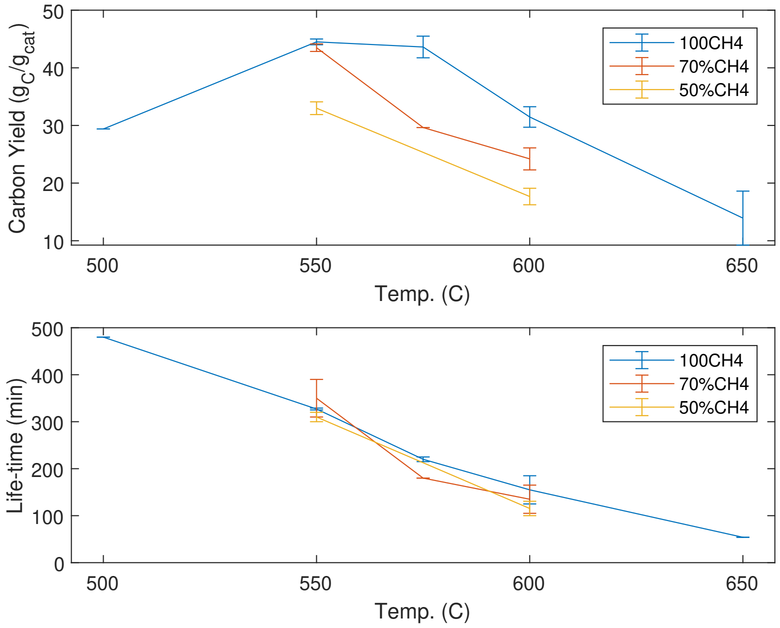

Fig. 2.5 The effect of temperature on the carbon yield (top) and lifetime (bottom).

Concentration of methane

Figure 2.6 shows that the maximum reaction rate is directly dependent on the volumetric concentration of methane as the only reactant of the reaction. What stands out in this figure is that at 550 °C and lower, the maximum reaction rate slightly declines with an increase in methane concentration to 90 vol.%. A possible explanation for this might be that methane adsorption is the dominating step at this temperature and saturation of the active sites allows less neighboring active sites to facilitate the detachment of hydrogen molecules.

One unanticipated finding was that the lifetime of the catalyst is shorter when the concentration of methane (and therefore the reaction rate) is lower, Figure 2.7, while some other researchers observed the opposite behavior [21, 28]. This effect is stronger at lower concentrations or at higher temperatures. We believe that the key difference is the scale of the reactor. Small reactors can be considered as a differential reactor and all the catalyst particles are in an environment with the same concentrations as the feed, while in the larger reactors such as in this work, except for the small portion next to the gas inlet, catalyst particles are in contact with a gas mixture containing the produced hydrogen. Another difference is that the methane concentration range in this study is much higher than most of the literature studies where only mild conditions were tested (max. methane concentration of 7.5% and 42.9% was tested by Latorre et al. [28] and Henao et al. [21] respectively). High concentrations lead to higher reaction rate and larger temperature drop along the reactor which is in favor of a longer lifetime. At higher methane concentrations, larger amounts of hydrogen are also produced and are present in the reactor. As mentioned in section 2.4.1, the addition of hydrogen changes the chemical potential and enhances the reverse reaction and converts the accumulated carbon on the surface of active sites back to methane. This phenomenon prevents encapsulation of the active sites and renews them, which significantly boosts the catalyst's lifetime. Figure 2.7 also reveals that carbon yield is decreased as the methane concentration is lowered by dilution with nitrogen. This was confirmed by using argon instead of nitrogen which led to almost the same effect. Analyzing the gas outlet with a mass spectrometer and also the solid products with XPS tests confirmed that neither nitrogen nor argon are involved in any reaction and are indeed inert.

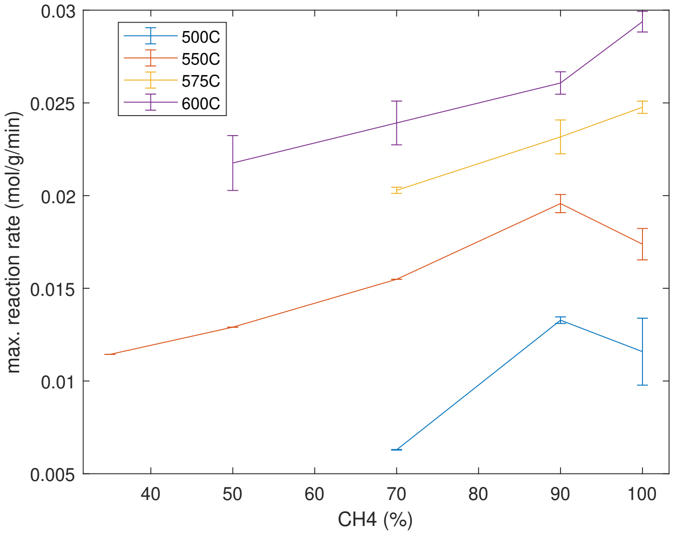

Fig. 2.6 The effect of concentration of methane (diluted by nitrogen or argon) on the maximum reaction rate of the reaction.

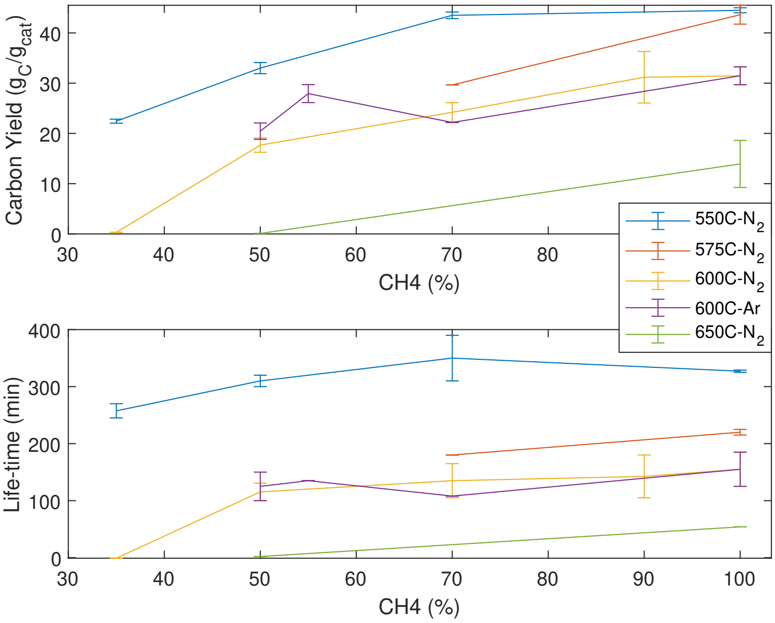

Fig. 2.7 The effect of concentration of methane (diluted by nitrogen or argon) on the carbon yield (top) and lifetime (bottom).

Concentration of hydrogen

Adding a small fraction of hydrogen to the feed decreases the maximum reaction rate by promoting the reverse reaction by Le Chatelier's principle, Figure 2.8. This leads to the higher refresh rate of the surface of active sites and, as a result a higher lifetime of the catalyst. Figure 2.9 shows that the carbon yield is improved by introducing small amounts of hydrogen to the reactor. This behavior was also observed by other researchers such as Latorre et al. [28].

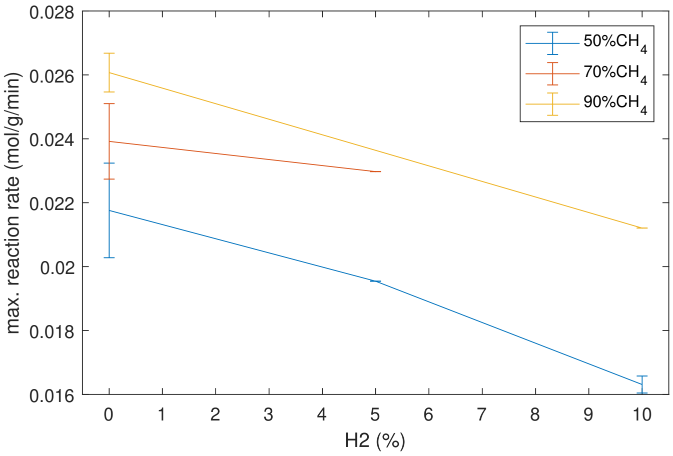

Fig. 2.8 The effect of concentration of hydrogen on the maximum reaction rate of the reaction at 600 °C.

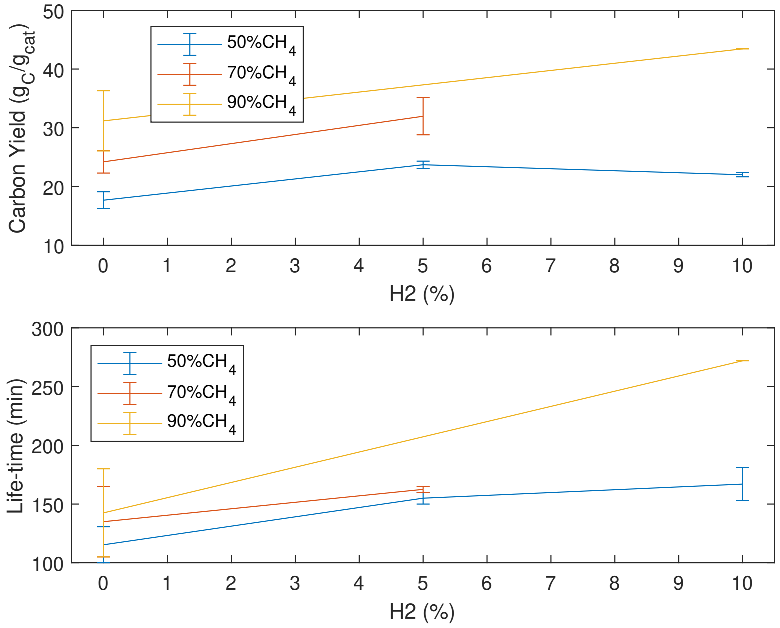

Fig. 2.9 The effect of concentration of hydrogen on the carbon yield (top) and lifetime (bottom) at 600 °C.

Particle size

Three different catalyst particle sizes were tested to investigate the importance of mass transfer limitation in the TCD process. It can be seen from Figure 2.10 that the effect of changing the particle size from the average diameter of 350 μm to 800 μm on the maximum reaction rate is very small. This confirms previous findings in the literature [11, 25, 27]. However, over time, the catalyst particle becomes larger and the effect of mass transfer limitation becomes more important by decreasing both diffusion length scale and pore volume due to carbon formation (See Table 2.1). These findings are also confirmed by Weisz-Prater criterion; see the appendix A. Figure 2.11 shows that the carbon yield is directly affected by the initial size of the catalyst particle. Because mass transfer limitation keeps the concentrations of methane and hydrogen inside the particles compared with smaller particles lower and higher, respectively. Therefore, the lifetime of the catalyst is boosted and as a result, carbon yield is also increased.

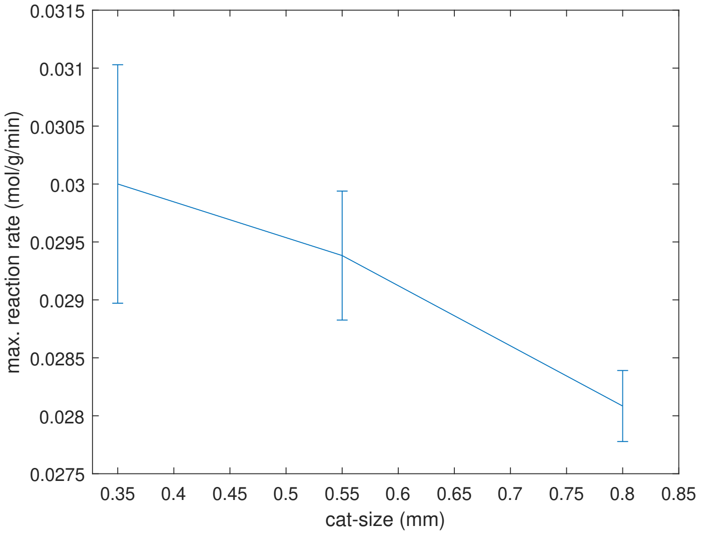

Fig. 2.10 The effect of size of the catalyst particle on the maximum reaction rate of the reaction in 100 vol.%CH_4 and 600 °C.

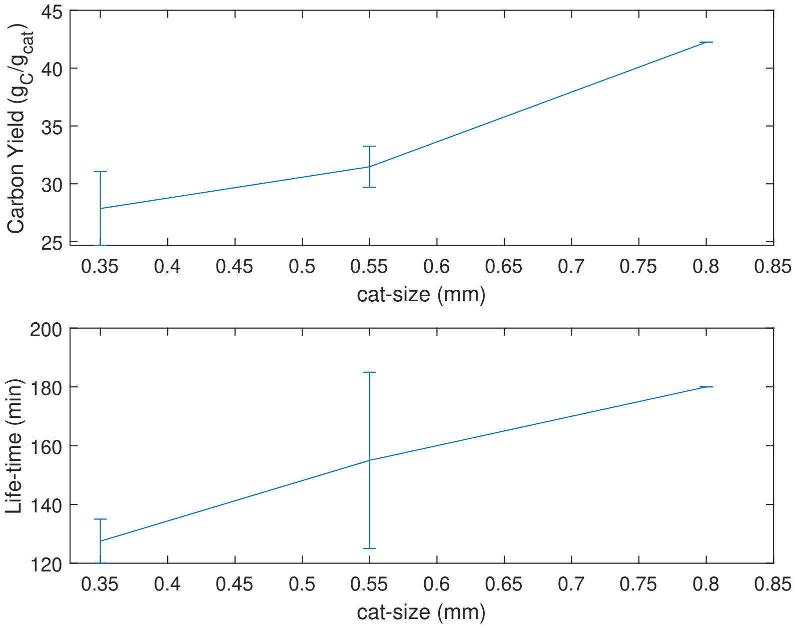

Fig. 2.11 The effect of size of the catalyst particle on the carbon yield (top) and lifetime (bottom) in 100 vol.%CH_4 and 600 °C.

Space velocity (SV)

SV was changed in the experiments while maintaining the volumetric flow rate at $4.5\,\mathrm{L_n/min}$ by changing the amount of the catalyst in the reactor. Lowering the volumetric flow rate would change the fluidization regime and can lead to breaking the quartz reactor due to defluidization of the grown catalyst particles and increasing it would turn the reactor at the beginning of the reaction into a pneumatic riser. Figure 2.12 shows that the reaction rate does not linearly increase with SV because the local reaction rate decreases along the height of the reactor. The reaction rate increases due to larger amounts of methane and smaller amounts of hydrogen available per unit of catalyst. This also explains the catalyst's shorter lifetime and lower carbon yield at higher SV, Figure 2.13.

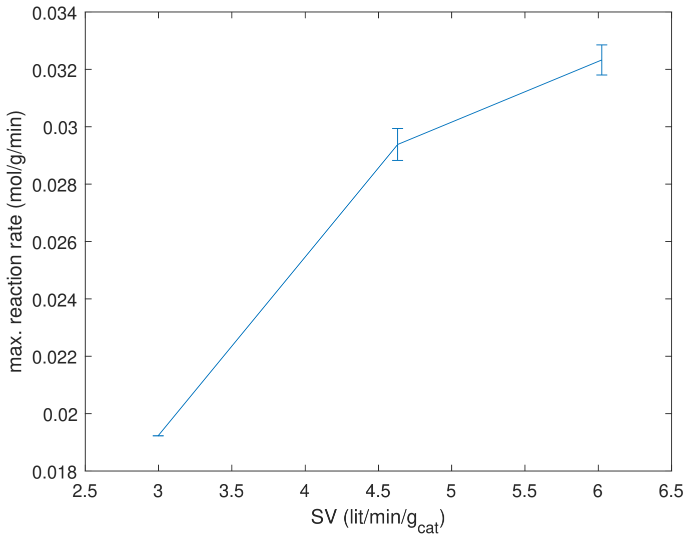

Fig. 2.12 The effect of SV on the maximum reaction rate of the reaction.

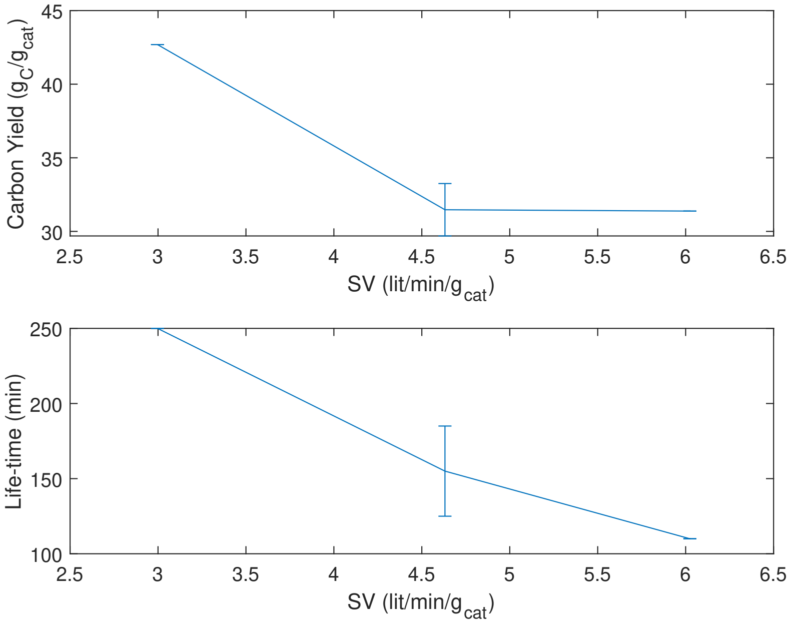

Fig. 2.13 The effect of SV on the carbon yield (top) and lifetime (bottom).

2.4.2 Characterization of the products

BET measurement results are presented in Table 2.1 and reveal a sharp decrease in the specific surface area and pore volume compared with the initial catalyst, suggesting the pores are filled up with carbon. The material density of the produced carbon, including the catalyst, is much lower than the fresh catalyst. As a result, since carbon is less dense than the catalyst material containing nickel, the bulk density is also reduced by about 32%. XPS analyses of the deactivated catalyst showed that all the nickel was in the metallic form and covered by carbon graphene layers. It suggests that deactivation is happening due to encapsulation of the active sites, which makes them inaccessible for the methane molecules. It was found that even in the case of less pure gases (99.5 %) no byproducts (either solid or gas) were formed.

The fraction of carbon that is produced in the form of desired graphene layer structures can be determined by evaluating the Derivative ThermoGravimetric (DTG) curve of oxidation temperature. The DTG is defined as the derivative of a TGA curve of the corresponding oxidation temperature. The highest temperature limit for oxidation of amorphous carbon reported in the literature is 410 °C [55]. However, Zhang et al. [56] and Hu et al. [57] reported 365 °C and 350 °C respectively for the oxidation of amorphous carbon and the carbon that is oxidized in temperatures above these limits is generally accepted to be nano-structured carbon. Figure 2.14 illustrates the TGA and DTG curve of the carbon produced from a feed of 100 %CH_4 at 550 °C. Even with considering 410 °C as the limit temperature of oxidation of amorphous carbon, the lowest purity of the different tested samples was about 96 % nano-structured carbon.

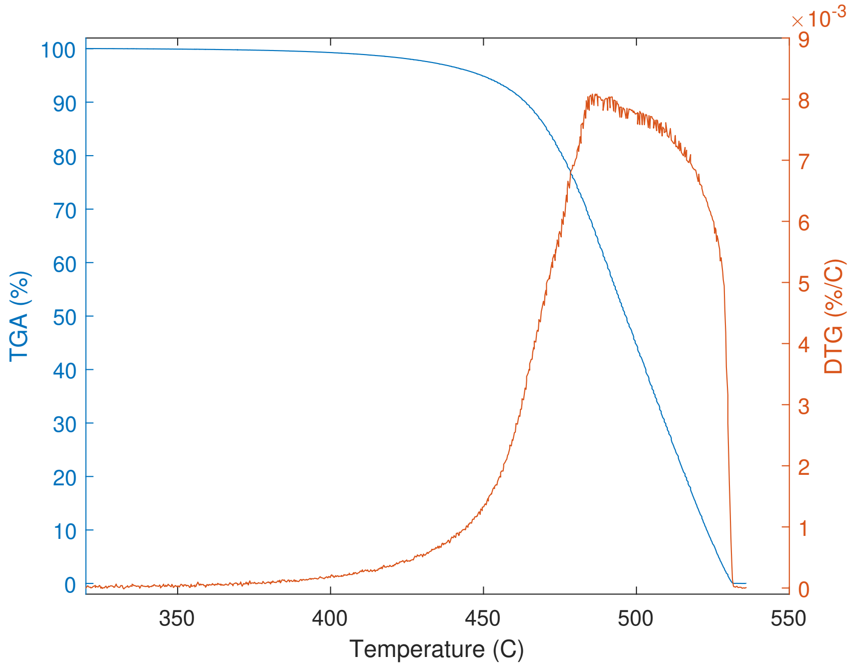

Fig. 2.14 Thermogravimetric and derivative thermogravimetric of the product obtained in a feed of 100 %CH_4 at 550 °C.

Figure 2.15 shows a TEM image of a cluster of produced carbon nanofibers, CNFs, in 100 %CH_4 at 550 °C. The diameters are in the range of $15-80$ nm. CNFs produced at the different operating conditions were in the form of stacked cones; see Figure 2.16. Stacked cones are also called a fishbone structure and were obtained also in the literature on the nickel catalyst supported by silica [20, 58].

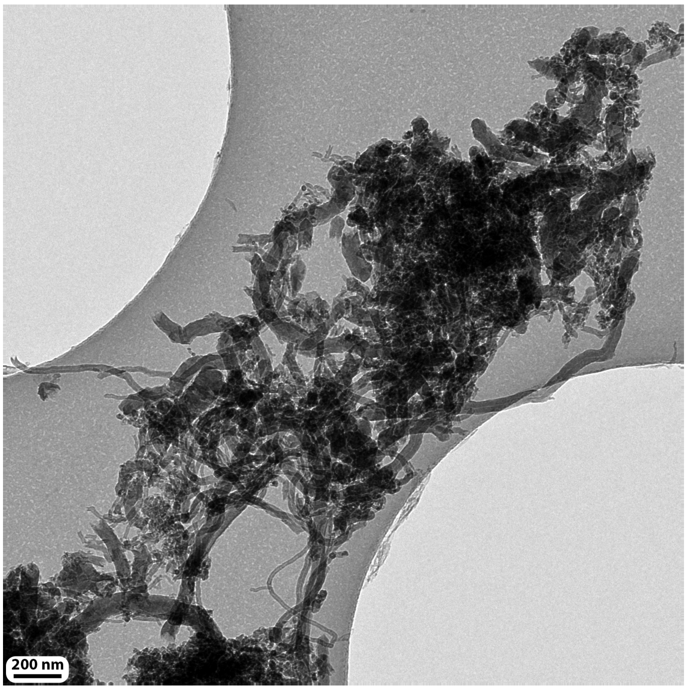

Fig. 2.15 TEM image of a cluster of produced CNFs in 100 %CH_4 at 550 °C.

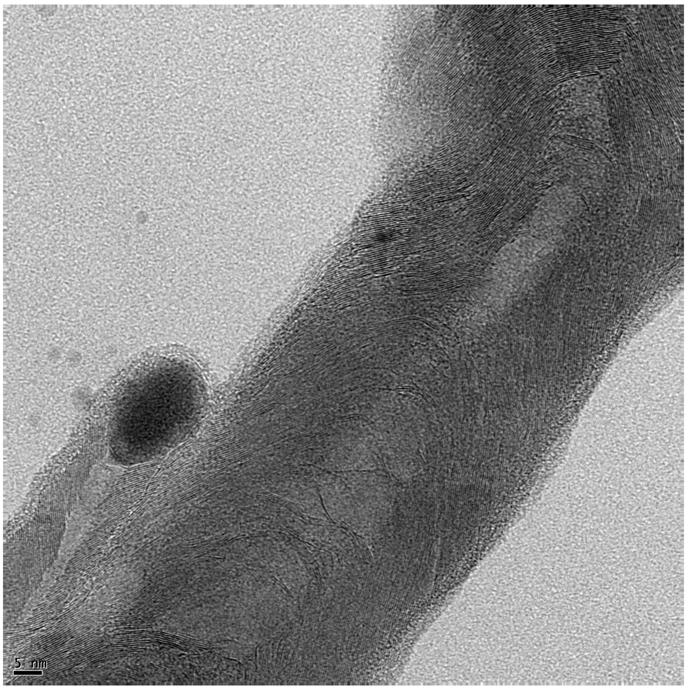

Fig. 2.16 TEM image of Two of the produced CNFs in 100 %CH_4 at 500 °C including an active site covered by carbon.

2.4.3 Kinetic Model

Initial reaction rate

The lifetime of the catalyst for some of the conditions at 650 °C is so short that the maximum reaction rate could not be measured reliably. At 500 °C, the reaction was limited by thermodynamic equilibrium in some of the operating conditions. Therefore, only the experimental data obtained at 550 °C, 575 °C and 600 °C were used to find the exact kinetic parameters by the model described in Section 2.3.1. Table 2.2 presents the kinetic parameters of the TCD reaction rate, equation 2.3. The average and maximum relative error of equation 2.3, using parameters from Table 2.2, do not exceed 11% and 22%, respectively.

Table 2.2 Kinetic coefficients of Equation 2.3.

Coefficient	Parameter	Value	Unit
k	A	5.940×10^4	$\mathrm{mol_{CH_4}/atm_{CH_4}/g_{cat}/min}$
	E	88	kJ/mol
K_{H_2}	A_{H_2}	1.871×10^{-8}	$\mathrm{atm}^{-3/2}$
	ΔH_{H_2}	144	kJ/mol
K_{CH_4}	A_{CH_4}	6.979×10^{-5}	atm^{-1}
	ΔH_{CH_4}	56	kJ/mol

Deactivation factor

The deactivation factor was fitted to the experimental data at 550 °C, 575 °C and 600 °C and Table 2.3 shows the obtained values. The total carbon yield obtained from each experiment and the model were compared. The average and maximum relative differences were 13.0% and 28.7% at the highest. Figures 2.17-2.18 illustrate three examples of the catalyst's performance over time in the experiments and predicted by the model at different operating conditions. Segregation of the reactor as it is described in section 2.3.2 is clearly visible by drops of the deactivation factor.

Table 2.3 Parameters of Equation 2.4

Coefficient	Parameter	Value	Unit
k_d	A_d	18.39	s^{-1}
	E_d	147	kJ/mol
$k_{d,C}$	$A_{d,C}$	309.87	-
	$\Delta H_{d,C}$	26	kJ/mol
k_{d,CH_4}	A_{d,CH_4}	-449.02	atm^{-1}
	$\Delta H_{d,CH_4}$	5.376	kJ/mol
k_{d,H_2}	A_{d,H_2}	-0.349	$atm^{-0.83}$
	$\Delta H_{d,H_2}$	80.19	kJ/mol

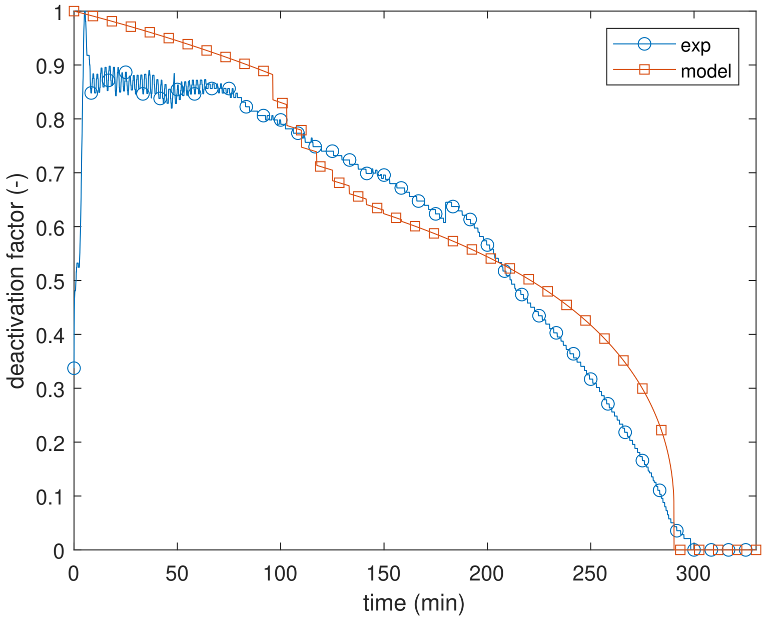

Fig. 2.17 Comparison of the deactivation factor of experiments and the model in a feed of 50 %CH_4 at 550 °C.

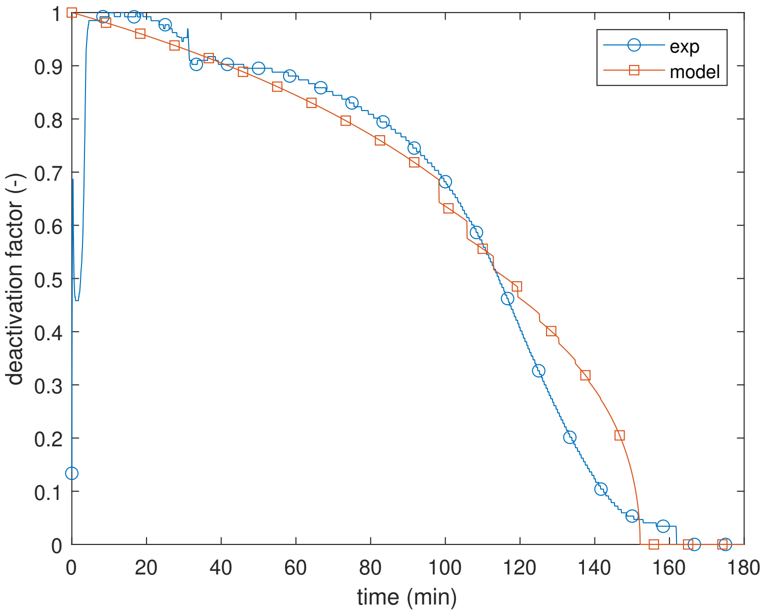

Fig. 2.18 Comparison of the deactivation factor of experiments and the model in a feed of 50 %CH_4 and 10 %H_2 at 600 °C.

2.5 Conclusions and outlook

In this study, the thermocatalytic decomposition of methane in a fluidized bed reactor was studied and the corresponding reaction kinetics were established. A commercial nickel on silica catalyst was used in this study and carbon yields of up to and in excess of 70 g_C/g_{cat} were obtained. The carbon produced was mainly in the form of carbon nanofibers. Its purity was characterized by TEM, TGA and XPS tests. The produced carbon had at least 96% purity of fish bone structures.

The effect of operating conditions has been investigated and it was found that at lower temperature, a larger amount of carbon was produced despite that the maximum reaction rate was lower. This was due to the delayed deactivation of the catalyst at lower temperature. Lowering the concentration of methane lowered the maximum reaction rate, lifetime and carbon yield. Our study has also revealed that although the presence of hydrogen decreases the maximum reaction rate, a higher carbon yield is achieved due to the longer lifetime of the catalyst.

A kinetic model describing the maximum reaction rate and the deactivation factor was developed. This model describes the reaction rate of TCD as a function of time in the temperature range of 550 − 600 °C with reasonable accuracy and averaged error in the initial kinetic rate of 10% and deactivation factors up to 17 %. This model, together with the corresponding commercially available catalyst, can be used for further study of TCD and reproduction of data.

A very high SV was chosen in this study to facilitate the mobility of catalysts that have grown due to large depositions of carbon, and to prevent breaking the reactor's wall. As a result, the conversion of the gas was limited. On an industrial scale, this can be overcome with a proper continuous reactor design and partial recycling of the gas stream.

گر یک نفست ز زندگانی گذرد
مگذار که جز به شادمانی گذرد
هشدار که سرمایهٔ سودای جهان
عمرست چنان کش گذرانی گذرد

خیام

If from life’s domain a breath takes flight,
Let it be in joy, a radiant light.
Beware, the world’s desire in time you find,
It’s yours to spend, as you’ve designed.

Khayyam

3

Numerical modeling of intra-particle phenomena and the catalyst particle growth - A MGM model[1]

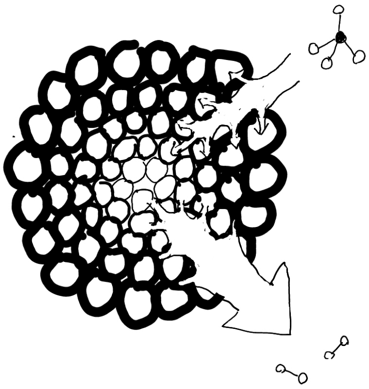

---

[1] This chapter is based on *Hadian, M., Buist, K. A., Bos, A. N. R., Kuipers, J. A. M. (2021). Single catalyst particle growth modeling in the thermocatalytic decomposition of methane. Chemical Engineering Journal, 421, 129759 [11].*

Abstract

ThermoCatalytic Decomposition of methane (TCD) is studied as a method to convert natural gas into hydrogen and functional carbon. In these processes the carbon typically formed on top of a catalyst phase leading to particle growth. Therefore, developing a particle growth model is necessary to understand the limitations of thermocatalytic decomposition of methane and to assess optimal parameters and process conditions. This chapter presents a particle growth model to describe the growth of functional carbon on the catalyst particle. This coupled model requires kinetic equations and information on deactivation rates which have been studied in literature. The morphology of the particle changes due to carbon formation, which leads to eventual deactivation. Therefore, these kinetic expressions are coupled to a particle growth model based on the analogy with the growth of particles in polyolefin production. To combine the effects of particle growth, kinetics, and internal heat and mass transfer, the Multi-Grain Model (MGM) was used. Results confirm that with the currently available catalysts the carbon yield is not affected by heat and mass transfer limitations; however, with the availability of more active catalysts these limitations will become important. Temperature, however, has a significant role in that it regulates the kinetic rate and thus growth rate, which in turn influences the catalyst deactivation. The optimum temperature for the production of nano-carbon, within a reasonable process time, therefore sensitively depends on the choice of catalyst.

3.1 Introduction

Hydrogen can be produced through different processes from different feedstocks, such as steam methane reforming, water splitting, and thermocatalytic decomposition of methane. Steam methane reforming coupled with CO_2 capture and storage (CCS) technologies are the most known and investigated methods in the field of low carbon footprint hydrogen production. However, the separation of produced CO_2 and handling and storage leads to costs for gas separation and storage management. Water splitting is an energy and capital-intensive process and increases the final price of hydrogen. By contrast, methane decomposition to functional carbon materials and hydrogen has advantages to the alternative processes, such as the elimination of additional purification/separation units and production of valuable carbon nanomaterials (tubes or fibers) instead of CO_2. The potential applications of carbon nanomaterials in semiconductors, additives to building materials, energy storage, and catalytic materials due to their unique physicochemical properties such as high conductivity, high tenacity and mechanical strength, high specific surface area and semiconductor properties make TCD more economically and environmentally appealing [12–14, 17, 25, 59]. This chapter presents a more extensive review of the existing kinetic models for TCD compared to the preceding chapter. It is important to note that this chapter precedes chapter 2 and consequently, the kinetic models presented herein have been sourced from the literature.

Methane, in the absence of oxidizing agents or a catalyst (including inert heterogeneities), decomposes naturally to hydrogen and amorphous carbon at high temperatures, >1300°C (reaction 5.18) [6]. The addition of a catalyst facilitates the decomposition of methane in two ways. First, the activation energy and therefore the required temperature for conversion decreases (between 500°C to 950°C dependent on the active material of the catalyst); Second, solid carbon can be produced in specific nano-structured shapes, depending on the support and active materials of catalyst and operating conditions. Nickel, iron, copper, and carbon are the most common materials used as the active sites of the catalysts. Many studies have been performed on the catalyst preparation, different support and active materials, thermodynamics and kinetics of the thermocatalytic decomposition of methane [10, 14, 16, 17, 60]. In general, nickel has the highest activity and rate of methane decomposition. Compared to the others, Nickel is active in a lower temperature range and is more likely to deactivate. However, the addition of a second (or even a third) metal such as iron or copper, to the nickel, has shown improved stability at higher temperatures and less deactivation [46–49].

$$CH_4(g) \longrightarrow C(s) + H_2(g) \qquad \Delta H_{(298K)} = +74.52\, kJ/mol \tag{3.1}$$

Despite the high potential of TCD for producing carbon nanomaterials and CO_2-free hydrogen, it is greatly restricted for industrial applications due to inadequate productivity, uncertainties of process performance and operational challenges coming from carbon formation [14]. Therefore, in addition to studies on catalysts, the TCD reactor and process have to be developed, designed and controlled thoroughly to become feasible at an industrial scale. For a rational reactor and process design, modeling and experimental studies can provide the required understanding and basic data for this. This understanding facilitates the identification of optimal process conditions for maximum carbon nanomaterial production. Modeling of the catalyst performance as a function of equivalent process time is critical for understanding and predicting the product and catalyst evolution in the reactor. This performance can be expressed with the ratio of the mass of produced carbon to the mass of fresh catalyst used, called carbon yield (Equation 3.2) and the change in catalyst particle size and density.

$$carbon\ yield = \frac{mass\ of\ produced\ carbon\ (g)}{mass\ of\ original\ catalyst\ (g)} \tag{3.2}$$

In the literature, including the work of Ashik some studies have been reported on modeling at the molecular scale [14, 61, 62], which helps scientists in catalyst evaluation and to develop a microscopic level of understanding of the complete chemical transformation. Although these models are helpful in understanding reaction mechanisms, a model that properly describes the behavior of a catalyst at the macro level has not been reported to the best of our knowledge. In particular, the formation of a functional carbon layer onto the catalyst phase leads to particle growth [14]. The particle size and thus, growth is a crucial parameter in designing a reactor. In the present chapter, for the first time, the multi-grain model (MGM) based on the analogy with the growth of polyolefin particles is developed to describe the macroscopic behavior of growing particles in the TCD of methane. The model couples different phenomena involved inside the catalyst particle (which is called macroparticle in this study) such as heat and mass transfer and chemical reaction. A short review of kinetic studies in the literature is provided in section 3.2. In section 5.2, the model description is presented. The model validation and its reactor predictions assessed in sections 3.4 and 5.3, respectively.

3.2 Short review of kinetics in literature

In TCD, the activity of the catalyst and kinetic rate of reaction decreases over time due to deactivation. The actual rate of reaction at time $t > 0$ is described using two parameters: the initial reaction rate and a time-dependent deactivation factor.

3.2.1 Initial reaction rate

The initial reaction rate and the reaction mechanism have been studied extensively [14]. Douven et al. and Yadav et al. proposed reaction rate equations for carbon nanotubes (CNT) production by TCD of the methane which is only dependent on methane concentration [13, 63], (see Equation 3.3 below). Yadav found out that multi-walled CNT is produced with a different kinetic rate than single-walled CNT, both only depend on the concentration of methane [24], (see Equation 3.4). Ashik et al. 2017 proposed Equation 3.5 for the initial reaction rate which also does not depend on the hydrogen concentration [64].

$$r_0[kmol_{CH_4}/kg_{cat}/s] = \frac{K_1 P_{CH_4}[atm]}{\left(1 + \frac{K_1 P_{CH_4}[atm]}{K_2}\right)^2} \tag{3.3}$$

$$r_0[kmol_{CH_4}/kg_{cat}/s] = \frac{K_1 P_{CH_4}[atm]}{\left(1 + \frac{K_1 P_{CH_4}[atm]}{K_2}\right)} \tag{3.4}$$

$$r_0[mmol_{CH_4}/g_{cat}/min] = k_p P_{CH_4}^{1.4}[atm] \tag{3.5}$$

The majority of studies have revealed that the hydrogen concentration has a negative effect on the initial reaction rate due to thermodynamic factors equilibrium and occurrence of the reverse reaction [6, 25, 27, 65–67]. The kinetic models presented in equations 3-5 must, therefore be regarded as a simplified form of the actual kinetics. The equations (6-8) that involve the effect of the hydrogen concentration have a very similar form, but differ mostly in the expression in the denominator. Amin et al. [6] and Snoeck et al. [66] derived Equation 3.6 while Borghei et al. [27] suggested different powers for H_2 and CH_4, Equation 3.7, which may be due to the use of a different catalyst and the specific operating conditions used in their studies [6, 27, 66]. Saraswat et al [25] have reported a more extended form of the reaction rate, equation 3.8, which includes effects of hydrogen and methane partial pressures in Langmuir-Hinshelwood type of expressions [25].

$$r_0[mmol_{CH_4}/g_{cat}/min] = \frac{k(P_{CH_4}[atm] - {P_{H2}}^2[atm]/K_p)}{\left(1 + K_{H_2}{P_{H_2}}^{1.5}[atm] + K_{CH_4}P_{CH_4}[atm]\right)^2} \tag{3.6}$$

$$r_0[mol_{CH_4}/g_{cat}/hr] = \frac{k(P_{CH_4}[atm] - {P_{H2}}^2[atm]/K_p)}{\left(1 + K_{H_2}{P_{H_2}}^{0.5}[atm] + K^*_{H_2}P^{1.5}_{H_2}[atm]\right)^2} \tag{3.7}$$

$$r_0[mol_{CH_4}/g_{cat}/s] = \frac{k_1 P_{CH_4}[atm] - k_2 {P_{H_2}}^2[atm]}{\left(1 + k_3 P_{CH_4}[atm] + k_4 {P_{H_2}}^{0.5}[atm] + k_5 P_{H_2}[atm] + k_6 {P_{H_2}}^{1.5}[atm]\right)^2} \tag{3.8}$$

According to the literature [6, 25, 67] The most likely mechanism of the reaction is based on molecular adsorption of methane as the first step, followed by a series of dehydrogenation reactions that take place one by one until it ends with separate adsorbed carbon and hydrogen atoms. Detachment of the first H from CH_4 is known to be the slowest and the rate-determining step. Every two adsorbed hydrogen atoms form a single H_2 molecule, which is released from the catalytic surface. The carbon atom, however, can diffuse into the nickel catalyst and either forms nanomaterials or encapsulates the active site.

3.2.2 Deactivation factor

The ratio of the reaction rate at time t to the initial reaction rate (Equation 3.9) is called the deactivation factor. The deactivation factor expresses the stability of the catalyst over time, which is a crucial factor in order to obtain a high carbon yield.

$$a = \frac{r(t)}{r_0} \tag{3.9}$$

Several different empirical or semi-empirical equations for the deactivation factor have been defined. Borghei [27] proposed Equation 3.10 for the deactivation factor, where b, c and d are constants and k_d is defined by an Arrhenius type of temperature dependency. Douven [13] reported that deactivation is reversible and probably due to the formation of amorphous carbon and encapsulation of active sites. Douven used a sigmoid Equation (3.11) as the deactivation factor, where parameter b is assumed to have only temperature dependency however, parameters t_0 and c decrease slightly as the methane partial pressure increases.

$$a = \frac{1}{\left(1 + (d-1)k_d P_{CH_4}^{c}[atm] P_{H_2}^{b}[atm] t[min]\right)^{1/(d-1)}} \tag{3.10}$$

$$a = d - b\tanh\left(\frac{t[s]-t_0}{c}\right) \tag{3.11}$$

Equation 3.12 is proposed by Amin et al. [6] and is based on the proposed mechanism in 3.2.1, the mass balance of species on the surface of the catalyst and the assumption that all the reaction steps except one are in equilibrium. So, the concentrations of intermediate species are negligible. All parameters (K_d, $K_{d,C}$, k_{d,CH_4} and k_{d,H_2}) are temperature dependent following the Arrhenius equation and are determined by fitting the expression to experimental data.

$$a = \left(\frac{1}{1 - 0.5k_d\left(k_{d,C} + k_{d,CH_4}P_{CH_4} + k_{d,H_2}P_{H_2}^{0.83}\right)t}\right)^{-0.8} \tag{3.12}$$

3.3 Model description

For our model of the TCD reactor and the particle growth over time, the following physical phenomena have to be taken into account:

1. The transport of species into and out of the particle, being the diffusion of methane into the catalyst pores and diffusion of hydrogen out of the catalyst pores.

2. The heat transfer into the macroparticle to provide the heat for the strongly endothermic reaction. This includes the transfer from the bulk gas to the external surface of the macroparticle, conduction within the macro macroparticle as well as conduction within the grains.

3. The decomposition of methane on the active sites of the macroparticles into hydrogen and solid carbon.

4. The accumulation of solid carbon onto the catalyst, with consequential catalyst growth and deactivation of the catalyst.

These phenomena are very similar to the olefin polymerization, which also experiences particle growth of the macroparticle due to solid product formation. For the solids formation and particle growth different modeling approaches have been developed [68, 69]. For our TCD process, the most appropriate model, capable of modeling particle growth and convenient for further development to include fragmentation [70], is the Multi-grain model (MGM).

MGM is based on two assumptions. Firstly, the macroparticle is spherical with only profiles in the radial direction. So, it is a 1D model in the radial direction. Secondly, the macroparticle is composed of layers of identical non-porous grains (microparticles) with active sites on their surface[69–73]. The growth and evolution of the macroparticle are due to the accumulation of produced carbon on the surface of grains. Figure 3.1 shows the schematic of both the concepts of macroparticle and internal grain layers before and after the reaction takes place. Figure 3.1 (a) shows the schematic of a fresh porous macroparticle consisting of layers of non-porous grains illustrated as black spheres. Figure 3.1 (b) shows a circular sector of the same macroparticle after entering the reactor. The gray shell around each grain is the produced carbon on the grain.

3.3.1 Mass transfer

Methane and hydrogen diffusion through the macroparticle's pores and through the accumulated carbon layer surrounding the catalyst fragments is modelled at two different scales. At the scale of the macroparticle the process is modelled by the diffusion-reaction equation in spherical coordinates:

$$\frac{\partial M(r,t)}{\partial t} = \frac{1}{r^2}\frac{\partial}{\partial r}\left(D_e r^2 \frac{\partial M(r,t)}{\partial r}\right) - R(r,t) \tag{3.13}$$

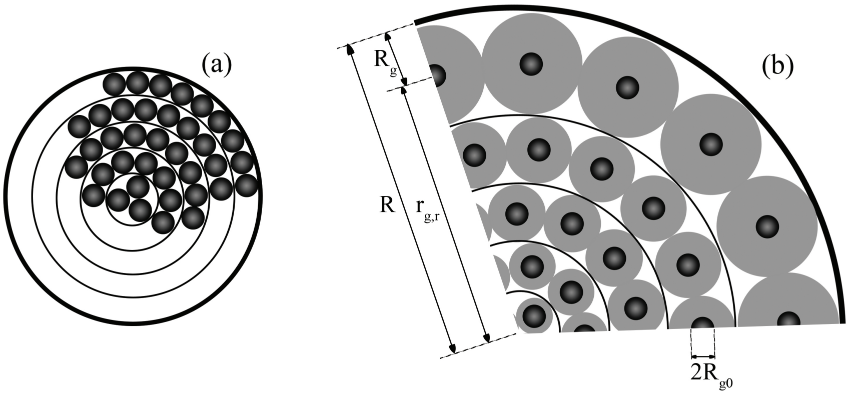

Fig. 3.1 Schematic of macroparticle and layers of grains in MGM model. (a) The fresh catalyst is composed of layers of grains. (b) A circular sector of the macroparticle with produced carbon on the surface of grains. The grain cores are illustrated as black circles and the gray shell around them is the layer of produced carbon.

Where M is the molar concentration of a component, r is the radial position in macroparticle and D_e is the effective diffusivity of the considered component. $R(r,t)$ is the average rate of reaction at a given radial position:

$$R(r,t) = \frac{(1-\varepsilon)\sum_{g=1}^{N_{g,r}}\left(4\pi R_{g0}^2 .r(t)\right)}{\frac{4}{3}\pi\left(r^3-(r-dr)^3\right)} \tag{3.14}$$

Where ε is the porosity of the catalyst, $N_{g,r}$ is the number of grains at radial position r and R_{g0} is the radius of the core of the grains. Equation 3.13 can be solved with the following boundary and initial conditions:

$$\frac{\partial M(0,t)}{\partial r} = 0 \tag{3.15}$$

$$D_e\frac{\partial M(R,t)}{\partial r} = k_m(M-M_b) \tag{3.16}$$

$$M(r,0) = M_0 \tag{3.17}$$

k_m is the external mass transfer coefficient of the macroparticle, M_b is the external concentration and M_0 is the initial concentration in the particle.

The concentration at the grain scale is also modelled by the diffusion equation in spherical coordinates, Equation 3.18. Considering the assumption that the core of the grains is non-porous, so there is no hydrogen or methane inside the core of the grains. Therefore, the boundary conditions, Equations 3.19 and 3.20 are defined at the surface of the core and outer surface of the grain particle.

$$\frac{\partial M(r_g,t)}{\partial t} = \frac{1}{r_g^2}\frac{\partial}{\partial r_g}\left(D_p r_g^2 \frac{\partial M(r_g,t)}{\partial r_g}\right) \tag{3.18}$$

$$D_p \frac{\partial M(R_{g0},t)}{\partial r_g} = r(t).CF \tag{3.19}$$

$$M(R_g,t) = M(r_{g,r},t) \tag{3.20}$$

Where r_g is the radial position in the grain, D_p is the diffusivity in the product layer around the grains, R_g is the radius of whole grain and $r_{g,r}$ is the position of grain in the macroparticle (Figure 3.1) and CF is the unit conversion factor. The initial condition is the same for the macroparticle (Equation 3.17). Equations 3.13-3.17 are solved only once during each time step for the macro macroparticle, while equation 3.18 and its initial and boundary conditions are solved for all the internal grain layers at each time step.

3.3.2 Heat transfer

The heat transfer mechanism at both scales is based on conduction. The temperature profile in the macro-particle is calculated by Equation 3.21:

$$\frac{\partial T(r,t)}{\partial t} = \frac{1}{r^2}\frac{\partial}{\partial r}\left(\frac{k_h}{\rho C_P} r^2 \frac{\partial T(r,t)}{\partial r}\right) - \frac{\Delta H}{\rho C_P} R(r,t) \tag{3.21}$$

Where k_h, ρ and C_P are the heat conductivity, the density and the specific heat capacity of the macroparticle, respectively, ΔH is the heat of reaction and $R(r,t)$ is obtained from Equation 3.14. Equation 3.21 can be solved with the following initial and boundary conditions (Equations 3.22 to 3.24):

$$\frac{\partial T(0,t)}{\partial r} = 0 \tag{3.22}$$

$$k_h \frac{\partial T(R,t)}{\partial r} = h(T - T_b) \tag{3.23}$$

$$T(r,0) = T_0 \tag{3.24}$$

h is the external convective heat transfer coefficient outside the macroparticle which can be estimated from the Gunn correlation, T_0 and T_b are respectively the initial temperature and the temperature outside the macroparticle.

The radial temperature profile in the grains can be obtained from the heat conductivity equation in spherical coordinates for the whole domain of the core of the grain and the layer of the carbon product. However, the heat conductivity, density and specific heat capacity (k_g, ρ_{gr} and C_{P_g}) have different values in the core of the grains and in the product layer.

$$\frac{\partial T(r_g,t)}{\partial t} = \frac{1}{r_g^2}\frac{\partial}{\partial r_g}\left(\frac{k_g}{\rho_{gr}C_{P_g}} r_g^2 \frac{\partial T(r_g,t)}{\partial r_g}\right) \tag{3.25}$$

$$k_g \frac{\partial T(R_{g0},t)}{\partial r_g} = r(t).CF.\Delta H \tag{3.26}$$

$$T(R_g,t) = T(r_{g,r},t) \tag{3.27}$$

One can notice the analogy between mass and heat transfer at both scales of the macroparticle and the grains.

3.3.3 Reaction kinetics

In this study, Equation 3.6 and 3.12 and corresponding parameter values are provided in Table 3.1 and are used in the model as the initial reaction rate and deactivation factor of reaction [6]. Carbon formation increases the radius of the grains and, consequently the size of the macroparticles. The growth rate of the radius of the grains is calculated by Equation 3.28 and the growth rate of the macroparticle equals the summation of the growth rate of all grain layers, Equation 3.29.

$$\frac{\partial R_g}{\partial t} = MW_{CH_4} \frac{R_{g0}^2\, r(t)}{\rho_{carbon} R_g^2} \tag{3.28}$$

$$\frac{\partial R}{\partial t} = 2\left[\sum_{1}^{N_g} \frac{\partial R_g}{\partial t}\right] \tag{3.29}$$

Table 3.1 Kinetic parameters of equation 3.6 and 3.12, taken from [6].

Constant	Parameter	Value
k	A	$4.64 \times 10^{7}\ \mathrm{mmol_{CH_4}/g_{Ni}/min/atm}$
	E	$88\ \mathrm{kJ\,mol^{-1}}$
K_{H_2}	A_{H_2}	$2 \times 10^{-8}\ \mathrm{atm^{-3/2}}$
	ΔH_{H_2}	$144\ \mathrm{kJ\,mol^{-1}}$
K_{CH_4}	A_{CH_4}	$3.75 \times 10^{-5}\ \mathrm{atm^{-1}}$
	ΔH_{CH_4}	$56\ \mathrm{kJ\,mol^{-1}}$
K_P	A_P	$4.38 \times 10^{-5}\ \mathrm{atm}$
	ΔH_P	$-88.21\ \mathrm{kJ\,mol^{-1}}$
CF		$2.49 \times 10^{-8}\ \mathrm{mol\,min\,g_{Ni}/(mmol\,s\,m^{2})}$
k_d	A_d	4904
	E_d	$147\ \mathrm{kJ\,mol^{-1}}$
$k_{d,C}$	$A_{d,C}$	313
	$\Delta H_{d,C}$	$26\ \mathrm{kJ\,mol^{-1}}$
k_{d,CH_4}	A_{d,CH_4}	$-4082\ \mathrm{atm^{-1}}$
	$\Delta H_{d,CH_4}$	$3.56\ \mathrm{J\,mol^{-1}}$
k_{d,H_2}	A_{d,H_2}	$-0.34\ \mathrm{atm^{-0.83}}$
	$\Delta H_{d,H_2}$	$81\ \mathrm{kJ\,mol^{-1}}$

3.4 Verification of the model

The performance and the results of the model are validated by comparing its results with analytical solutions and results obtained from an independent PDE solver. Two limiting cases are used to verify the implementation of the model. In the simplified **case 1**, it is assumed that there is only one layer of micro grains, the mass transfer limitation is low, and the reaction is first order without deactivation. In this case, the mass of carbon produced is calculated by Equation 3.30:

$$carbon\ produced\ (kg) = (4\pi R_{g0}^{2}.N.t.k.M_{CH_4}.MM_{CH_4}) \tag{3.30}$$

Where R_{g0} is the radius of the core of micro grains, N is the number of micro grains in the only available layer in the macroparticle, t is the time passed since the start of the reaction, k is the kinetic coefficient of the first-order reaction per surface area of grain core (mol/m^2) and MM_{CH_4} is the molar mass of methane. Figure 3.2 illustrates the high accuracy of MGM in case 1, by showing that the MGM results matches the Equation 3.30.

In **case 2**, again, it is assumed that the reaction is first order in methane and independent of the hydrogen concentration without any deactivation ($r = k.P_{CH_4}$). The second assumption is that the reaction takes place uniformly in the macroparticle. Finally, it is assumed that the physical properties of the macroparticle do not change with time as the reaction proceeds. In these conditions, the methane concentration profile inside the particle can be calculated at any time by solving Equation 3.31 and its associated initial and boundary conditions.

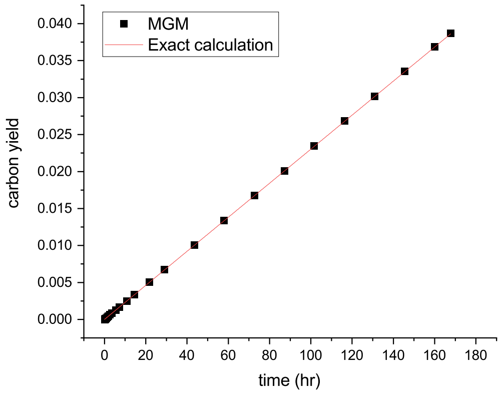

Fig. 3.2 Verification of the model by comparing the results of simplified case 1 with exact solutions. The curves of MGM results and exact data calculated by Equation 3.30 are matched with very high accuracy.

$$\frac{\partial M(r,t)}{\partial t} = \frac{1}{r^2}\frac{\partial}{\partial r}\left(D_e r^2 \frac{\partial M(r,t)}{\partial r}\right) - k.M(r,t) \tag{3.31}$$

$$M(r,t=0) = M_0$$

$$\frac{\partial M(r=0,t)}{\partial r} = 0$$

$$M(r=R,t) = M_b$$

The set of equations can be rewritten in dimensionless from via the definition of the following dimensionless quantities:

$$\widehat{M} = \frac{M}{M_b} \tag{3.32}$$

$$\widehat{r} = \frac{r}{R} \tag{3.33}$$

$$\widehat{t} = \frac{D}{R^2}t \tag{3.34}$$

$$M_T = R\sqrt{\frac{k}{D_e}} \tag{3.35}$$

M_T is a Thiele modulus and represents the reaction rate to diffusion rate ratio. By using these dimensionless quantities in Equations 3.31, they change to:

$$\frac{\partial \widehat{M}(\widehat{r},\widehat{t})}{\partial \widehat{t}} = \frac{1}{\widehat{r}^2}\frac{\partial}{\partial \widehat{r}}\left(\widehat{r}^2\frac{\partial \widehat{M}(r,t)}{\partial \widehat{r}}\right) - M_T^2.\widehat{M}(\widehat{r},\widehat{t}) \tag{3.36}$$

$$\widehat{M}(\widehat{r},\widehat{t}=0) = \widehat{M}_0$$

$$\frac{\partial \widehat{M}(\widehat{r}=0,\widehat{t})}{\partial \widehat{r}} = 0$$

$$\widehat{M}(\widehat{r}=1,\widehat{t}) = 1$$

Equation 3.36 has been solved with an independent PDE-solver (Matlab pdepe solver). Figure 3.3 compares the results of MGM with the Matlab solver. As is clearly illustrated, the results of the MGM are in almost perfect agreement with the Matlab solver over time, from the start of the reaction till the steady state condition has been reached (which is about one minute in this case). This confirms that the model works correctly and there are no errors in the calculation methods.

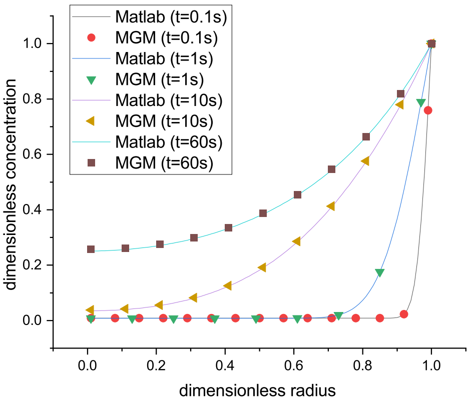

Fig. 3.3 Verification of the model by comparing the results of simplified case 2 (M_T=3.25) with Matlab PDE solver at different times. Solid lines Matlab PDE solver results and symbols are MGM output.

3.5 Results and discussion

The results of MGM simulations are evaluated using a sensitivity analysis and assessing the importance of different parameters and operating conditions in TCD. The temperature range used in our models is limited to the operating conditions that are used to derive the kinetic coefficients of equations 3.6 and 3.12 (temperature: 500-650 °C and maximum hydrogen fraction: 10%) to ensure of the validity of results [6]. Table 3.2 provides the most important parameters used in the model for the following cases, unless otherwise stated or the importance of the parameter is evaluated.

Table 3.2 Operating conditions used in the simulations.

Parameter	**Value**
initial macro particle radius	500um
number of microparticle layers	25
reactor pressure	1 atm
reactor temperature	650 °C
reactor mole fraction of CH4	1
reactor mole fraction of H2	0
initial Temperature of particle	350 °C
methane effective diffusivity in the porous particle	$1.36 \times 10^{-6}\ \mathrm{m^2/s}$
hydrogen effective diffusivity in the porous particle	$5.40 \times 10^{-6}\ \mathrm{m^2/s}$
external mass transfer coefficient	$2.26 \times 10^{-2}\ \mathrm{m^3_{gas}/m^2_{interface}/s}$
heat conductivity	30 W/m/K
external heat transfer coefficient	$622\ \mathrm{W/m^2_{interface}/K}$

3.5.1 Mass and heat transfer limitations

To assess the impact of internal mass transfer limitations, the diffusivity was altered to one thousand times higher and lower values than the (base case) values stated in Table 3.2. The results are summarized in Figure 3.4 and reveal that lowering the internal mass transfer rate does not affect the carbon yield. Hence, for the conditions of Table 3.2 the effect of diffusion limitation is negligible. On the other hand, if the mass transfer limitation increases to one thousand times higher, the carbon yield decreases by about 35%.

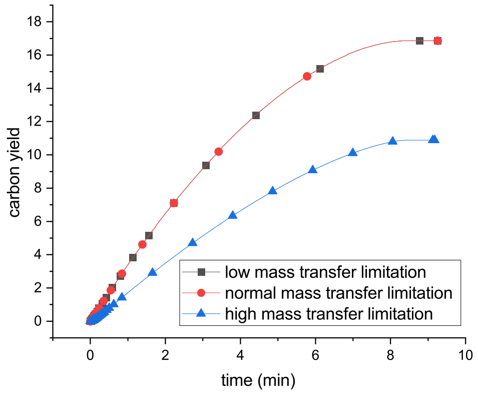

Fig. 3.4 Internal mass transfer effect. The results of the cases with one thousand times higher and lower mass transfer limitations are compared with normal mass transfer limitation

The importance of internal diffusional resistance is also confirmed by the WeiszPrater criterion (Equation 3.37) that estimates the importance of the diffusion on the reaction rates in heterogeneous catalytic reactions [74]. In the normal case, $C_{WP} = 9.02 \times 10^{-4} << 1$, which means that internal mass transfer does not influence the production rate of carbon. However, in the case with one thousand times lower effective diffusion coefficient, $C_{WP} = 0.902$, which implies that for such low diffusion coefficients, internal mass transfer limitation is not negligible anymore compared to the reaction rate.

$$C_{WP} = \frac{r_0 \rho R^2}{D_e M_b} \tag{3.37}$$

The same procedure was applied to assess the role of the internal heat transfer limitation, by changing the thermal conductivity of the solid material composing the macroparticle. The results are presented in Figure 3.5. Since the carbon yield is not affected by lowering the heat transfer limitation, for the conditions of Table 3.2 the heat transport resistance is negligible compared to other factors. However, the carbon yield is decreased dramatically in the case with 1000 times higher heat transfer limitation. In this case, the temperature in the macroparticle increases relatively slowly, and as a result, the reaction rate and, therefore the slope of the curve increases gradually.

In addition, external heat and mass transfer limitations can prevail in the thin film around the macroparticle. However, it was observed that even with the highest external heat and mass transfer limitation, meaning a macroparticle in a stagnant gas phase ($Nu = 2$ and $Sh = 2$) and with larger particle sizes (1000 μm), the production rate of carbon is not reduced.

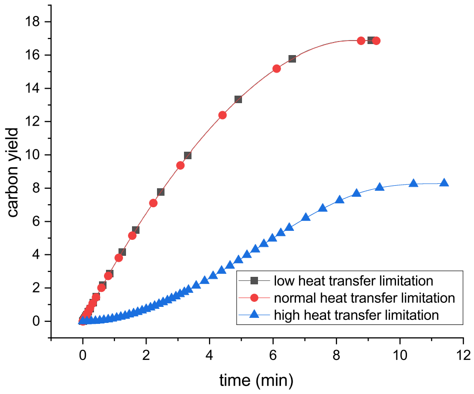

Fig. 3.5 Internal heat transfer effect. The results of the cases with one thousand times higher and lower heat transfer limitations are illustrated alongside normal mass transfer limitation

These observations regarding mass transfer importance and their effect on the TCD process are in agreement with literature findings derived from both experiments and the Weisz-Prater criterion [25, 27].

3.5.2 Reaction kinetic effect

Figure 3.6 illustrates in logarithmic scale how much the carbon yield changes if the initial reaction rate changes by a factor of 1000. Reduction of the reaction rate leads to a decrease by a factor of 1000 in carbon yield. This finding is another confirmation of the fact that the reaction is the rate-determining step compared to the mass and heat transfer limitations (Section 3.5.1). On the other hand, if the reaction is one thousand times faster, the carbon yield increases around 450 times. This means that in this case, mass and heat transfer limitations become also important, which again is in agreement with Section 3.5.1.

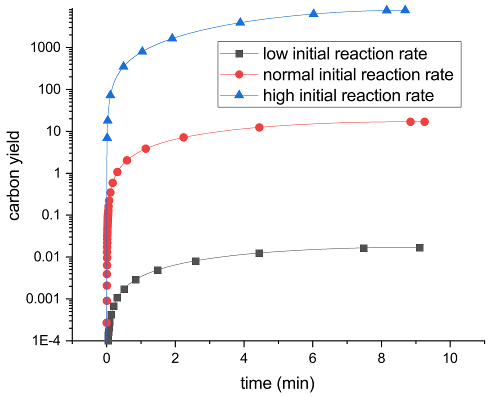

Fig. 3.6 The effect of initial reaction rate when it changes one thousand times. In the case with one thousand times faster kinetics, the carbon yield is increased about 450 times, while the change for the case with one thousand times slower kinetics difference is about one thousand times.

3.5.3 Bulk gas concentration effect

As can be seen in Figure 3.7 adding inert gas (which means lowering the methane fraction) decreases the carbon yield. On the other hand, for a given fraction of methane, increasing the fraction of hydrogen leads to a lower initial reaction rate and higher durability of the catalyst against deactivation. These effects are presented in Figure 3.8. These two effects together lead to higher carbon yield, however, in comparison a pure methane feed yields a higher amount of carbon in a shorter amount of time.

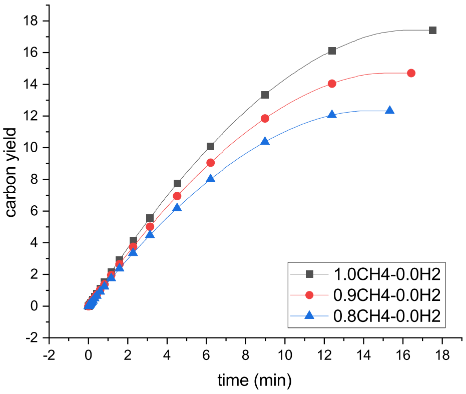

Fig. 3.7 the effect of adding inert gas to the reactor on carbon yield. Lowering the concentration of CH_4 decreases the reaction rate and, consequently the carbon yield.

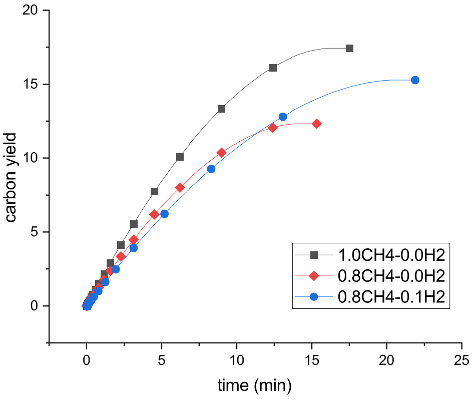

Fig. 3.8 The effect of adding hydrogen to the reactor on carbon yield and comparison of the result with pure CH_4 methane as the feed. The rest of gas fraction until 1 is inert gas. Adding H_2 lowers both the reaction and deactivation rates.

3.5.4 Temperature effect

Temperature has two opposing effects in the TCD process. On the one hand, higher temperature leads to a higher initial reaction rate and therefore a higher carbon production rate. On the other hand, increasing the temperature results in faster catalyst deactivation and lowers the final carbon yield. These two phenomena are illustrated in Figure 3.9. At high temperatures, deactivation proceeds more suddenly instead of gradual deactivation at lower temperatures. Thus, curves of 600 °C and 650 °C have a very short flat part, rather than a longer flat tail.

Increasing the temperature between 500 °C to 650 °C leads to a lower carbon yield due to the increased deactivation rate. However, it should be noted that this slightly lower amount of carbon is produced in a significantly shorter period of time. Therefore, in the examined conditions and with the used kinetic model, the optimum operating conditions will depend on economic considerations. It should be noted that using a different catalyst (and as a result, different kinetic models) may change this optimum condition.

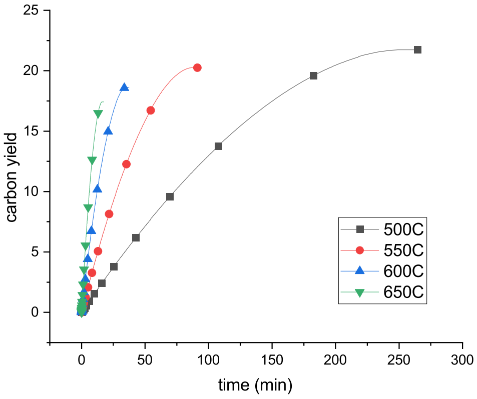

Fig. 3.9 The effect of operating temperature on the carbon yield. Higher temperature leads to higher initial reaction rate (initial slope of the curves) and faster deactivation (endpoint of curves).

3.5.5 Effect of number of micro grain layers

The number of micro grain layers in the macroparticle is a model parameter that is not straightforward to measure or estimate, as previous parameters were. As Figure 3.10 shows, this number significantly impacts the carbon yield. The effect of the number of grain layers is not linear and becomes stronger with an increase in the number of layers. Although physically, the number of micro grain layers can be translated to the specific surface area of the macroparticle, the internal structure of an actual catalyst particle is more complex than the structure defined by many layers of identical spheres. Therefore, the number of grain layers will be used as the tuning parameter of the model against validated data.

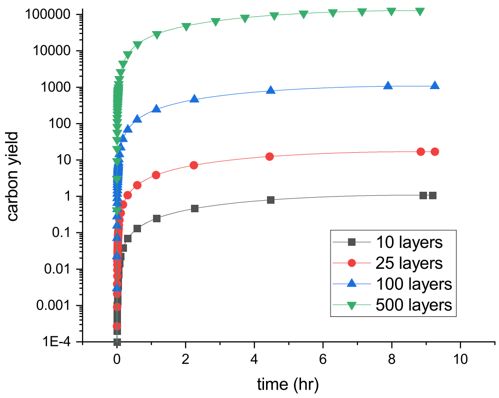

Fig. 3.10 The effect of the number of grain layers. There is a positive relation (non-linear) between the number of micro grain layers in the model and the predicted carbon yield.

3.6 Conclusions

A Multi-Grain Model has been developed to model the heat and mass transfer inside macroparticles coupled with the decomposition reaction of methane. The reaction rate model and deactivation factor from Amin [6] are used, however, the model is suitable for the use of other kinetic models which can be easily accommodated.

The effect of operating conditions and model parameters has been investigated by sensitivity analyses and it was found that the heat and mass transfer rates do not limit the carbon production rate and consequently, the reaction is the rate-limiting step of the process. This fact is in agreement with experimental findings respected in the literature. However, if a catalyst is made with one thousand times higher ratio of kinetics rate to the mass and heat transfer rates (either by increasing the reaction rate or decreasing the mass and heat transfer rates), the heat and mass transfer limitations will affect the final carbon yield.

It was found that, the presence of hydrogen causes a decrease in the reaction rate, however a higher carbon yield is achieved due to delayed deactivation of the catalyst. Moreover, increasing the operating temperature leads to a faster initial reaction rate and faster catalyst deactivation and hence an optimal, process-dependent, temperature exists.

ما زنده به آنیم که آرام نگیریم
موجیم که آسودگی ما عدم ماست

صائب تبریزی

Living not to settle, we declare,
As waves, mere stillness we cannot bear.

Saeb Tabrizi

4

Coupling of MGM with CFD-DEM[1]

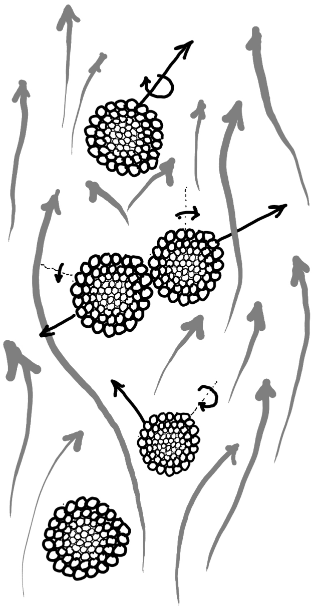

---

[1] This chapter is based on *M. Hadian, M. J. A. de Munck, K.A. Buist, A.N.R. Bos, J.A.M. Kuipers, (2023), Modeling of a catalytic fluidized bed reactor via coupled CFD-DEM with MGM: from intra-particle scale to reactor scale. Submitted to Chemical Engineering Science*

Abstract

The Computational Fluid Dynamics - Discrete Element Method (CFD-DEM) method is extended by coupling with the multi-grain model (MGM) to include intra-particle phenomena such as heat and mass transfer, reaction, and solid deposition next to the inter-particle and fluid-particle interactions in the reactor. This comprehensive model treats each particle individually and accounts for changes in particle properties due to temporal and spatial variations of the process conditions. It also captures the impact of the change in the particles' properties on the fluidized bed reactor characteristics, such as the hydrodynamic regime. The results of the model revealed that the fluidization characteristics and solids mixing are altered by particle growth. Particle growth also led to the formation of a particle size gradient along the height of the reactor. The coupling allows for monitoring of both external and internal mass transfer limitations. For the adopted reaction kinetics, growth rate and properties, the external mass transfer limitations remained negligible, however the internal mass transfer limitation plays a significant role in the process performance.

4.1 Introduction

Many chemical processes such as polymerization, oxidative coupling of methane, and ThermoCatalytic Decomposition of methane (TCD), utilize catalytic fluidized bed reactors. In a catalytic fluidized bed, the scale of the effective phenomena can vary from the mass and heat transfer within the micro-scale of a porous particle to the interaction of particles with each other and the fluid phase and the scale of the reactor when it comes to solids circulation patterns. Modeling these multi-phase phenomena is crucial in developing and optimizing the process. Numerical simulations with multi-scale models enable engineers to investigate multiphase flows in industrial chemical processes.

Computational Fluid Dynamics – Discrete Element Method (CFD-DEM) is known as a multi-scale Eulerian-Lagrangian technique to simulate processes involving fluid and solid particles [75–78]. CFD-DEM is a powerful method to model systems that include multi-scale solid-fluid interactions such as encountered in fluidized beds, spouted beds and pneumatic conveyors. Although CFD-DEM covers a wide range of the mentioned scales and can include heat and mass transfer between the continuous and discrete phases, it mostly assumes uniform (lumped) conditions inside the particles ($Bi \leq 0.1$) for both heat and mass and it lacks the intra-particle phenomena [76, 79–81]. In some processes, such as polymerization or TCD, catalyst particles can grow in size and therefore, the Biot number changes over time and from particle to particle and may exceed this limit.

Several publications have explored the use of CFD-DEM models in conjunction with intra-particle models to investigate biomass pyrolysis in FBR. Wang et al. have extended the CFD-DEM model by incorporating a 1D thermally thick model to capture internal heat transfer and heat of reaction [82]. Oyedeji et al. have employed a CFD-DEM model coupled with a 2D model to simulate cylindrical biomass particles [83, 84]. In another study, the impact of biomass shape was investigated using a 3D glued-spheres particle model [85]. While these models offer valuable insights for fundamental research, they can be computationally expensive. Furthermore, none of these models account for the influence of intra-particle reactions on FBR hydrodynamics.

In an earlier contribution, the authors developed the Multi-Grain Model (MGM) that models the particle growth by combining the surface reaction and deactivation kinetics, as well as intra-particle heat and mass transfer of reactants and products [11]. MGM provides insight into the importance of effective phenomena in an isolated particle and the change of particle parameters such as size and density [11, 69, 70]. However, it does not include the consequence of this evolution on the reactor characteristics, such as the hydrodynamics of the bed.

The particle properties and the overall reactor conditions as well as local conditions, can significantly affect each other [86]. Therefore, coupling CFD-DEM with MGM combines the potential of both approaches and allows us to capture the effects of dynamic catalyst characteristics on the reactor conditions and vice versa. One example is the influence of the increased particle size and mass on the fluidized bed hydrodynamics. Besides, studying the temperature and concentration profiles and their importance in the reactor is possible. As a result, the combined CFD-DEM-MGM methodology produces a more comprehensive representation of reality and is expected to produce more accurate results. This model enables engineers to predict the reactor performance over time and optimize the design and conditions of the reactor for industrial processes such as TCD and polyolefins production.

The outline of this chapter is as follows: in section 5.2 the coupled CFD-DEM-MGM model and the implementation of the coupling are described. In section 4.3 the implementation of the method is verified using analytical solutions. The results and discussion are presented in section 5.3. Finally, in section 5.4, the conclusions are presented.

4.2 Model description

CFD-DEM-MGM consists of three sub-models that are coupled with each other. CFD is responsible for modeling the continuous (gas) phase, including the momentum, energy and mass of species balances. DEM models the interaction of the particles with the gas phase, heat and mass transfer and drag and the interactions of the particles with each other and the reactor walls, collisions. MGM handles the heat and mass balance at the smallest scale: the reaction and mass deposition inside each of the particles individually.

4.2.1 Gas phase modeling

The gas phase is described by the volume-averaged Navier-Stokes equation (4.1) and the continuity equation (4.2):

$$\frac{\partial(\varepsilon_f \rho_f \mathbf{u}_f)}{\partial t} + \nabla \cdot (\varepsilon_f \rho_f \mathbf{u}_f \mathbf{u}_f) = -\varepsilon_f \nabla P_f - \nabla \cdot (\varepsilon_f \tau_f) + \varepsilon_f \rho_f \mathbf{g} - \mathbf{S}_p \tag{4.1}$$

$$\frac{\partial(\varepsilon_f \rho_f)}{\partial t} + \nabla \cdot (\varepsilon_f \rho_f \mathbf{u}_f) = \sum_{i=1}^{n_c} S_{m,i} \tag{4.2}$$

In all equations, the subscript f indicates the fluid phase and p is the particulate phase. ε is the gas volume fraction in the cell, ρ the density, $\mathbf{u_f}$ the fluid velocity and P_f the pressure. τ_f is the gas phase viscous stress tensor, provided by equation 5.4, which is assumed to follow the general Newtonian form:

$$\tau_f = -\mu_f \left[(\nabla \mathbf{u}_f) + (\nabla \mathbf{u}_f)^T - \frac{2}{3} (\nabla \cdot \mathbf{u}_f) \mathbf{I} \right] \tag{4.3}$$

where μ_f is the shear viscosity, and $\mathbf{I}$ the unity tensor. $S_{m,i}$ is the mass source of component i in the cell and is detailed in section 4.2.2. The fluid is assumed to be gas, thus the fluid density, ρ_f is dependent on the gas composition and is calculated according to the ideal gas law, equations 4.4 and 4.5 respectively.

$$MW_{mix} = \sum_{i=1}^{n_c} y_i MW_i \tag{4.4}$$

$$\rho_f = \frac{P MW_{mix}}{R T_f} \tag{4.5}$$

where M_i is the mass concentration of the component i , y_i the mole fraction of component i, MW_i and MW_{mix} are the molar mass of component i and the mixture.

$\mathbf{S}_p$ in equation 4.1 is the source term accounting for coupling of momentum exchange between the fluid and the particles given by equation (4.6):

$$\mathbf{S_p} = \frac{1}{V_{cell}} \sum_{a=0}^{N_p} \frac{V_{p,a}\beta_a}{1-\varepsilon_f}(\mathbf{u}_f - \mathbf{v}_{p,a})D(\mathbf{r}-\mathbf{r}_{p,a}) \tag{4.6}$$

where V_{cell} and $V_{p,a}$ represent the local cell volume and the volume of particle a. Due to the growing nature of particles, the poly-disperse drag correlations proposed by Sarkar and Beetstra [87, 88], equations 4.7 and 4.8 are used to calculate the interface momentum exchange coefficient, β. The distribution function, D, ensures that the drag force acts as a point force at the particle's center of mass [89]. The mapping of local properties from the Eulerian grid to Lagrangian particle positions and vice versa is performed by using a volume-weighing techniques developed by Hoomans et al. [90].

$$\beta_a = \left[\frac{d_{p,a}}{\langle d\rangle} + 0.064\left(\frac{d_{p,a}}{\langle d\rangle}\right)^3\right]\beta_{mono}(\varepsilon_f, \langle \mathrm{Re}\rangle) \tag{4.7}$$

$$\begin{aligned}\beta_{mono}(\varepsilon_f, \langle \mathrm{Re}\rangle) = {}& 180\frac{\mu_g(1-\varepsilon_f)^2}{\langle d\rangle^2 \varepsilon_f} + 18\frac{\mu_g \varepsilon_f^3(1-\varepsilon_f)(1+1.5\sqrt{(1-\varepsilon_f)})}{d_p^2} \\ & + 0.31\frac{\mu_g(1-\varepsilon_f)\langle \mathrm{Re}\rangle}{\langle d\rangle^2 \varepsilon_f}\left[\frac{\varepsilon_f^{-1} + 3\varepsilon_f(1-\varepsilon_f) + 8.4\langle \mathrm{Re}\rangle^{-0.343}}{1+10^{3(1-\varepsilon_f)}\mathrm{Re}^{-2.5+2\varepsilon_f}}\right]\end{aligned} \tag{4.8}$$

Where $\langle Re\rangle$ is the average Reynolds number in the cell, equation 4.9, calculated by the Sauter mean diameter, equation 4.10.

$$\langle Re\rangle = \frac{\varepsilon_f \rho_f(|\mathbf{u}_f - \mathbf{v}_{p,a}|)\langle d\rangle}{\mu_f} \tag{4.9}$$

$$\langle d\rangle = \frac{\sum_{a=1}^{N_{cell}} d_{p,a}^3}{\sum_{a=1}^{N_{cell}} d_{p,a}^2} \tag{4.10}$$

with N_{cell} indicating the total number of particles in the computational cell and $\mathbf{v}_{p,a}$ is the velocity particle a.

The gas phase thermal energy balance is given by equation 4.11:

$$Cp_f\left[\frac{\partial(\varepsilon_f \rho_f T_f)}{\partial t} + \nabla\cdot(\varepsilon_f \rho_f \mathbf{u}_f T_f)\right] = \nabla\cdot(\varepsilon_f K_f^{\mathrm{eff}}\nabla T) + Q_p \tag{4.11}$$

T is temperature, and Q_p represents the energy source term originating from the energy transport between the fluid and the particulates detailed in section 4.2.2. K_f^{eff} is the effective thermal conductivity of the fluid, which is calculated from the thermal conductivity of the fluid, K_f, and the fluid volume fraction, ε_f, via equation (4.12):

$$K_f^{\text{eff}} = \frac{1-\sqrt{1-\varepsilon_f}}{\varepsilon_f} K_f \tag{4.12}$$

The component mass balance is described by equation 4.13 considering convection, diffusion and a source term due to mass exchange with the catalyst particles:

$$\frac{\partial(\varepsilon_f M_{f,i})}{\partial t} + \nabla\cdot(\varepsilon_f M_{f,i}\mathbf{u_f}) = \nabla\cdot(\varepsilon_f D_{f,i}^{\text{eff}}\nabla M_{f,i}) + S_{m,i} \tag{4.13}$$

where $M_{f,i}$ is the mass concentration of components in the fluid, and the effective diffusivity of component i in the fluid, $D_{f,i}^{\text{eff}}$, is calculated similarly as K_f^{eff}, using equation 4.14. $S_{m,i}$ is the gas-particle mass source term transfer of component i and is defined in section 4.2.2

$$D_{f,i}^{\text{eff}} = \frac{1-\sqrt{1-\varepsilon_f}}{\varepsilon_f} \mathscr{D}_{fi} \tag{4.14}$$

4.2.2 Discrete phase modeling

DEM

The trajectory of individual particles in DEM are tracked by Newton's second law of motion, equation 4.15. Forces acting on the particle are on the right-hand side. These forces include the pressure gradient force, drag force, gravitational force and collisional forces, respectively. The particle-particle and particle-wall collisions are described by the soft-sphere model developed by Cundall and Strack [91]. In this approach, the contact forces are calculated using a linear spring and dashpot model [89, 92, 93].

$$m_{p,a}\frac{d\mathbf{v}_{p,a}}{dt} = m_{p,a}\frac{d^2\mathbf{r}_{p,a}}{dt^2} = -V_{p,a}\nabla P_f + \frac{V_{p,a}\beta_{p,a}}{1-\varepsilon_f}(\mathbf{u}_f - \mathbf{v}_{p,a}) + m_{p,a}\mathbf{g} + \sum \mathbf{F}_{contact,p,a} \tag{4.15}$$

in which $\mathbf{r}_{p,a}$ and $m_{p,a}$ are the position and the mass of the particle a.

The rotational motion of the particle is computed using equation (4.16).

$$I_{p,a}\frac{dw_{p,a}}{dt} = \mathbf{T}_{p,a} = \sum_{\text{b}\in\text{contact list}} (r_{p,a}\mathbf{n}_{ab} \times \mathbf{F}_{ab,t}) \tag{4.16}$$

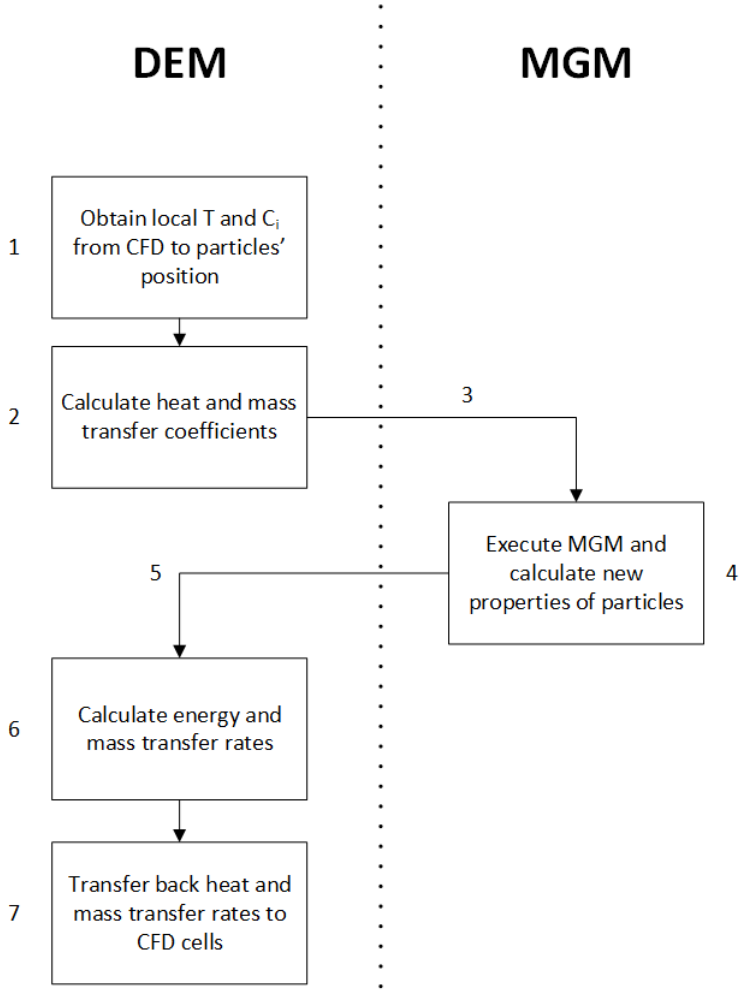
DEM
MGM
Obtain local T and C_i from CFD to particles' position
Calculate heat and mass transfer coefficients
Execute MGM and calculate new properties of particles
Calculate energy and mass transfer rates
Transfer back heat and mass transfer rates to CFD cells
1
2
3
4
5
6
7

Fig. 4.1 Schematic diagram of heat and mass transfer coupling steps between fluid and particles.

where $I_{p,a}$ is the moment of inertia, $w_{p,a}$ is the rotational velocity and $\mathbf{T}_{p,a}$ is the torque.

The mass and heat transfer between the fluid and particles is performed in 7 steps, as shown in Figure 4.1. In each time step, the local fluid temperature and concentration at the particle position are obtained. The local gas-particle heat and mass transfer coefficients are calculated. These transfer coefficients are used in the multi-grain model. As described in section 4.2.2, the particle surface temperature and concentrations are subsequently calculated. DEM obtains the particle temperature and concentration surface values from MGM and calculates the heat and mass transfer rates between particles and the fluid. In the last step, these transfer rates are coupled back to the Eulerian grid cells and is used as source terms in the gas thermal energy and mass balances, shown in equations 4.11 and 4.13 respectively.

The energy source term, Q_p in equation 4.11 is calculated from:

$$Q_p = \frac{1}{V_{cell}} \sum_{a=0}^{N_p} h_{p,a} A_{p,a} (T_{p,a} - T_f) D(\mathbf{r} - \mathbf{r_{p,a}}) \tag{4.17}$$

where $A_{p,a}$ is the heat exchanging surface area of particle a, and h_a the heat transfer coefficient calculated using the Nusselt number, Nu, from the Gunn correlation, equation 4.18:

$$\begin{aligned} Nu = \frac{h_a d_{p,a}}{k_f} &= (7 - 10\varepsilon_f + 5\varepsilon_f^2)(1 + 0.7 Re^{0.2} Pr^{0.33}) \\ &\quad + (1.33 - 2.4\varepsilon_f + 1.2\varepsilon_f^2) Re^{0.7} Pr^{0.33} \end{aligned} \tag{4.18}$$

Re and Pr are Reynolds and Prandtl number respectively:

$$Re = \frac{\varepsilon_f \rho_f (|\mathbf{u}_f - \mathbf{v}_p|) d_{p,a}}{\mu_f} \tag{4.19}$$

$$Pr = \frac{\mu_f C p_f}{K_f} \tag{4.20}$$

The mass source term of component i in equation 4.13 and in the continuity equation (4.2), $S_{m,i}$, is calculated from equation (4.21).

$$S_{m,i} = \frac{1}{V_{cell}} \sum_{a=0}^{N_p} k_{m,a,i} A_{p,a} (M_{p,a} - M_i) D(\mathbf{r} - \mathbf{r_{p,a}}) \tag{4.21}$$

where the mass transfer coefficient of component i between particle a and the fluid, $k_{m,a,i}$, is determined by the Sherwood number. The Sherwood number is computed using the Gunn correlation for mass transfer, equation 4.22. Sc is the Schmidt number, calculated from equation 4.23.

$$\begin{aligned} Sh_i = \frac{k_{m,a,i} d_{p,a}}{\mathscr{D}_{f,i}} &= (7 - 10\varepsilon_f + 5\varepsilon_f^2)(1 + 0.7 Re^{0.2} Sc^{0.33}) \\ &\quad + (1.33 - 2.4\varepsilon_f + 1.2\varepsilon_f^2) Re^{0.7} Sc^{0.33} \end{aligned} \tag{4.22}$$

$$Sc = \frac{\mu_f}{\rho_f D_{f,i}^{\mathrm{eff}}} \tag{4.23}$$

MGM

Each individual particle is modeled as a porous medium by MGM. In this model, the catalyst support is assumed to consist of several layers of solid spheres, called grains, with uniform coverage of active material on their surfaces, Figure 4.2. Heat and mass transfer is considered in the radial direction at two different scales and the reaction occurs at the surface of the grains.

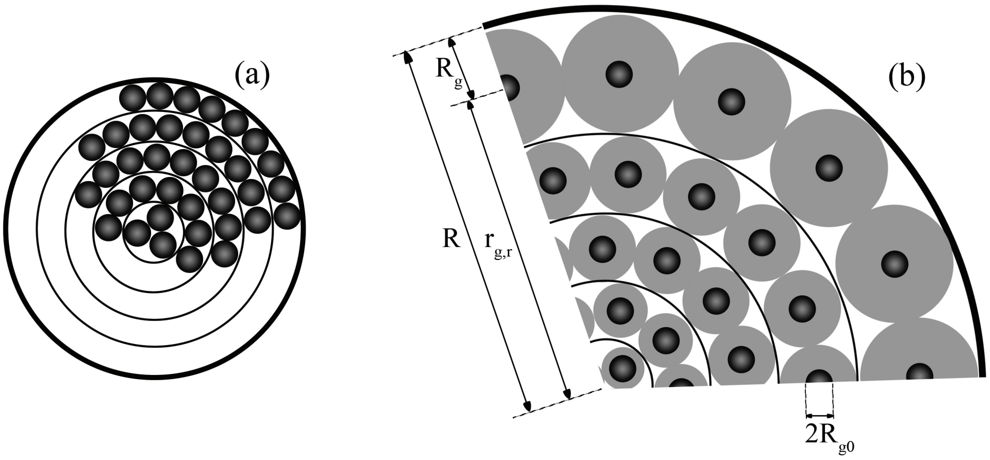

Fig. 4.2 Schematic of MGM model and layers of grains. (a) The particle before solid formation and growth. (b) A circular sector of the particle with the accumulated solid product on the surface of grains [11].

At the macro particle scale the component concentrations and temperature are governed by via equations 4.24 and 4.25:

$$\frac{\partial M_{p,a,i}(r,t)}{\partial t} = \frac{1}{r^2}\frac{\partial}{\partial r}\left(D^{\mathrm{eff}}_{p,a,i} r^2 \frac{\partial M_{p,a,i}(r,t)}{\partial r}\right) - R(r,t) \tag{4.24}$$

$$\frac{\partial T_{p,a}(r,t)}{\partial t} = \frac{1}{r^2}\frac{\partial}{\partial r}\left(\frac{k^{\mathrm{eff}}_{p,a}}{\rho_p Cp_p} r^2 \frac{\partial T_{p,a}(r,t)}{\partial r}\right) - \frac{\Delta H}{\rho_p Cp_p} R(r,t) \tag{4.25}$$

Where r is the radial position in particle and $D^{\mathrm{eff}}_{p,a,i}$ the effective diffusivity of component i, $k^{\mathrm{eff}}_{p,a}$, ρ_p and Cp_p the heat conductivity, the density and the specific heat capacity of the particle respectively, and $R(r,t)$ the volumetric average rate of reaction at a given radial position.

The concentration and temperature at the grain scale are also modeled by equations 4.26 and 4.27. The reaction occurs at the surface of the core of these grains and, therefore appears in the boundary conditions, equation 4.28. The solid product of the reaction accumulates on the grains' surface, causing an increase in radius leading to the alteration of the internal diffusion limitation.

$$\frac{\partial M(r_g,t)}{\partial t} = \frac{1}{r_g^2}\frac{\partial}{\partial r_g}\left(D_{prod} r_g^2 \frac{\partial M(r_g,t)}{\partial r_g}\right) \tag{4.26}$$

$$\frac{\partial T(r_g,t)}{\partial t} = \frac{1}{r_g^2}\frac{\partial}{\partial r_g}\left(\frac{k_g}{\rho_{gr} C_{P_g}} r_g^2 \frac{\partial T(r_g,t)}{\partial r_g}\right) \tag{4.27}$$

$$D_{prod}\frac{\partial M(R_{g0},t)}{\partial r_g} = r(t).CF \tag{4.28}$$

Where r_g is the radial position in the grain, D_{prod} is the diffusivity in the product layer around the grains, R_g is the radius of the whole grain and $r_{g,p}$ is the position of the grain in the particle (Figure 4.2) and CF is the unit conversion factor. For further details on MGM and its implementation and verification, see chapter 3.

Intra-particle mass and heat balance are coupled with the fluid as explained in section 4.2.2 by continuous flux boundary conditions on the surface of the particle, equations 4.29 and 4.30:

$$@r = R_p \quad -D_{p,a,i}^{\text{eff}}\frac{\partial M_{p,a,i}}{\partial r} = k_{m,a,i}\left(M_{p,a,i} - M_{f,i}\right) \tag{4.29}$$

$$@r = R_p \quad -k_{p,a}^{\text{eff}}\frac{\partial T_p}{\partial r} = h_a\left(T_p - T_f\right) \tag{4.30}$$

4.3 Verification and validation of the model

The implementation of the model is verified by comparing the results with analytical solutions in specific cases. Two-way heat and mass transfer between fluid and particles, the effect of removed mass from fluid to the particle on the fluid velocity, and the total mass balance of the reactor are evaluated and verified in the sections 4.3.1 to 4.3.4.

4.3.1 Temperature coupling

The heat transfer coefficient for each individual particle is calculated from equation 4.18. Assuming a lumped particle temperature ($Bi_p << 1$), the gas-particle heat transfer and the subsequent particle temperature change are calculated by the equations 4.31 and 4.32 respectively.

$$q_p = h(4\pi r_p^2)(T_p - T_f) \tag{4.31}$$

$$\frac{dT_p}{dt_{DEM}} = -\frac{q_p}{V_p \rho_p C p_p}] \tag{4.32}$$

In order to verify the implementation of the heat transfer, two tests were performed. In the first test a single particle ($T_{p,0} = 350\,^{\circ}\mathrm{C}$) is placed in a fluid with constant temperature ($T_f = 400\,^{\circ}\mathrm{C}$), Figure 4.3-left. The heat transfer coefficient is constant and calculated according to terminal particle velocity. The particle temperature over time can then be calculated by equation 4.33, obtained from the analytical solution.

$$T_{p,t} = T_f - (T_f - T_{p,0}) exp\left(\frac{-h(4\pi r_p^2)t}{V_p \rho_p C p_p}\right) \tag{4.33}$$

Figure 4.4 compares the simulation results with the analytical solution. A perfect match of the temperature of the DEM object verifies the CFD to DEM heat transfer implementation.

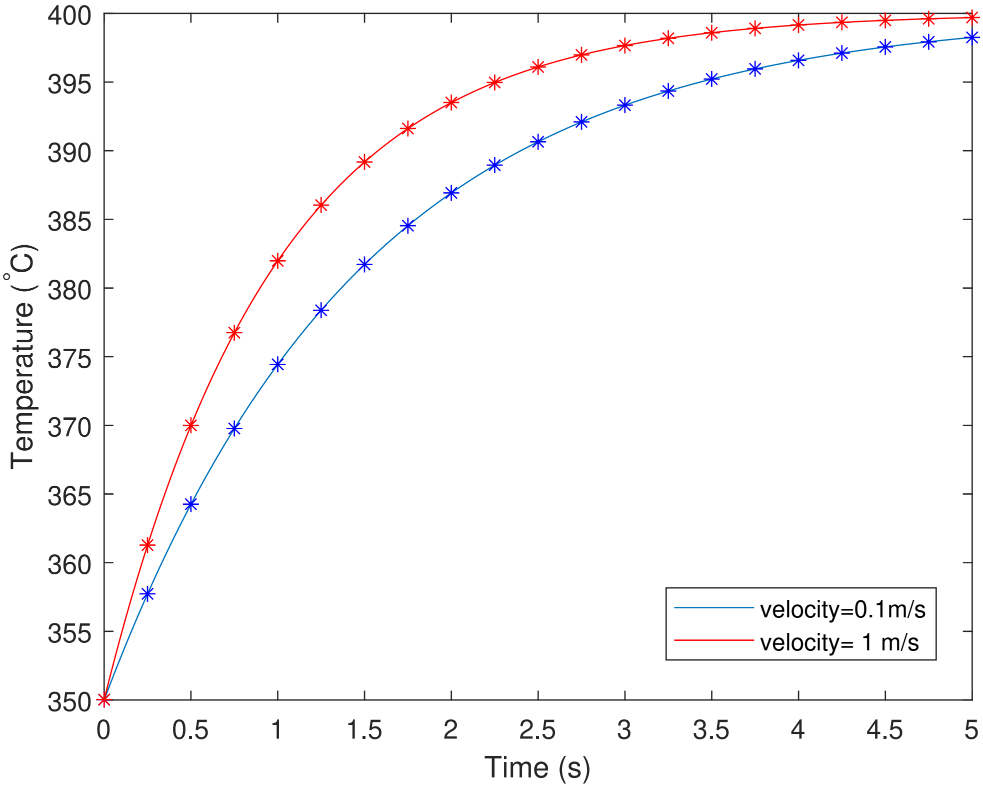

Fig. 4.4 Verification of the fluid to particle heat transfer with varying the falling particle velocity. Lines: analytical solutions. Symbols: simulation results.

In the second test case, the two-way gas-particle heat transfer is verified using a packed bed of (30 × 30 × 150) particles with initial temperature of 300 °C, Figure 4.3-right. The

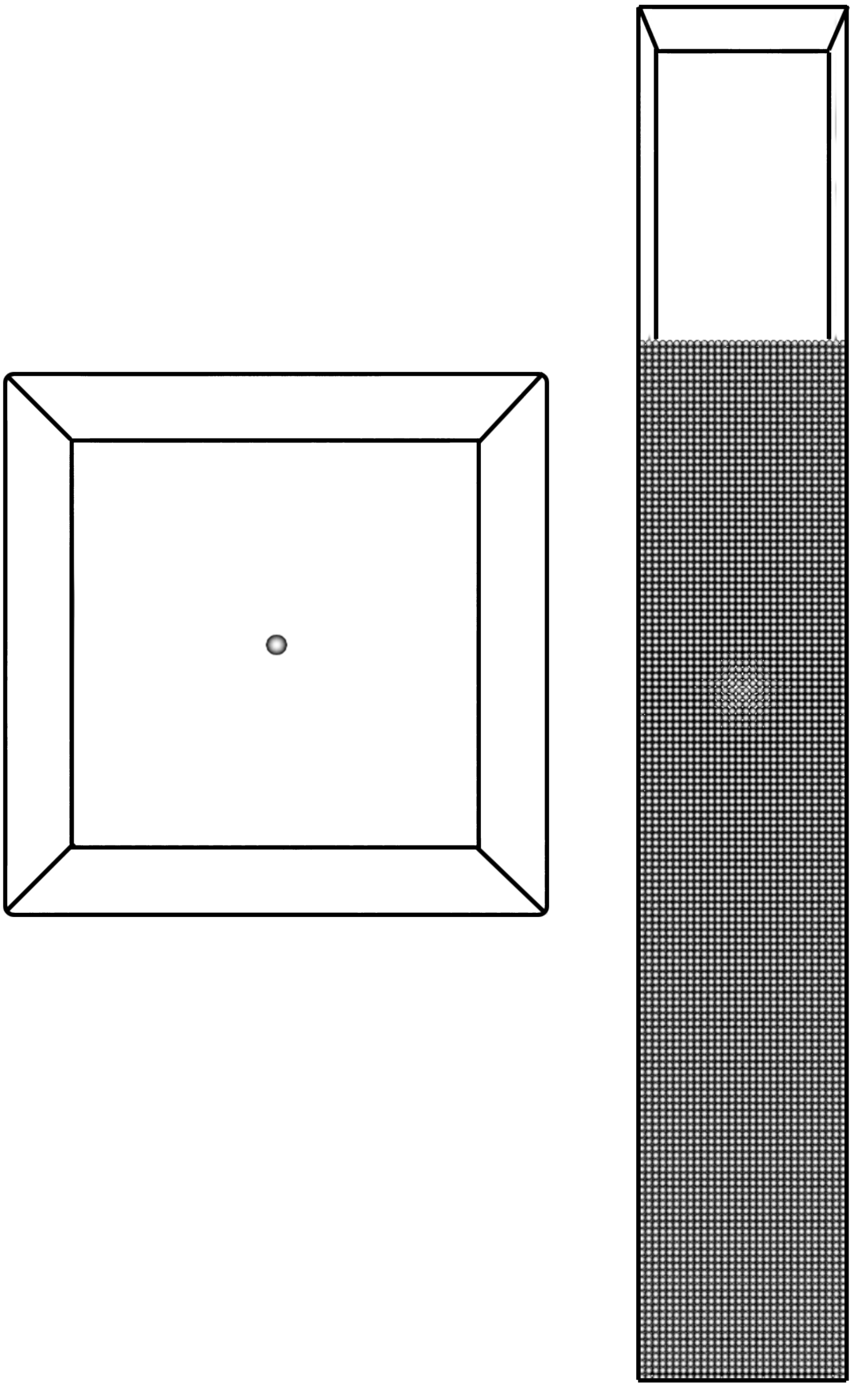

Fig. 4.3 The test case of verification of one-way heat and mass transfer (left) and two-way heat and mass transfer (right)

initial gas phase temperature is also equal to 300 °C. At time $t = 0\,\mathrm{s}$, a fluid flow with a temperature (400 °C) enters from the bottom of the bed. By applying a very high fluid Peclet number, the test case can be considered as a 1D convection problem. Equations 4.34 and 4.35 show the fluid and particle phase energy balances, respectively, at an axial position z in the bed.

$$\varepsilon_f \rho_f Cp_f \frac{\partial T_{f,z}}{\partial t} = \varepsilon_f \rho_f Cp_f u_{f,z} \frac{\partial T_{f,z}}{\partial t} - hA_p(T_{f,z} - T_{p,z}) \tag{4.34}$$

$$(1-\varepsilon_f)\rho_p Cp_p \frac{\partial T_{p,z}}{\partial t} = hA_p(T_{f,z} - T_{p,z}) \tag{4.35}$$

The details of the analytical solution for the temperature of the fluid over time can be found in the references [94–97]. Figure 4.5 illustrates the dimensionless temperature (equation 4.36) along the height of the bed at different times. From this figure, it is evident that there is a good agreement between the analytical solution and the simulation results, which emphasizes that the two-way gas-particle heat transfer coupling is correctly implemented.

$$\theta = \frac{T_f - T_0}{T_{in} - T_0} \tag{4.36}$$

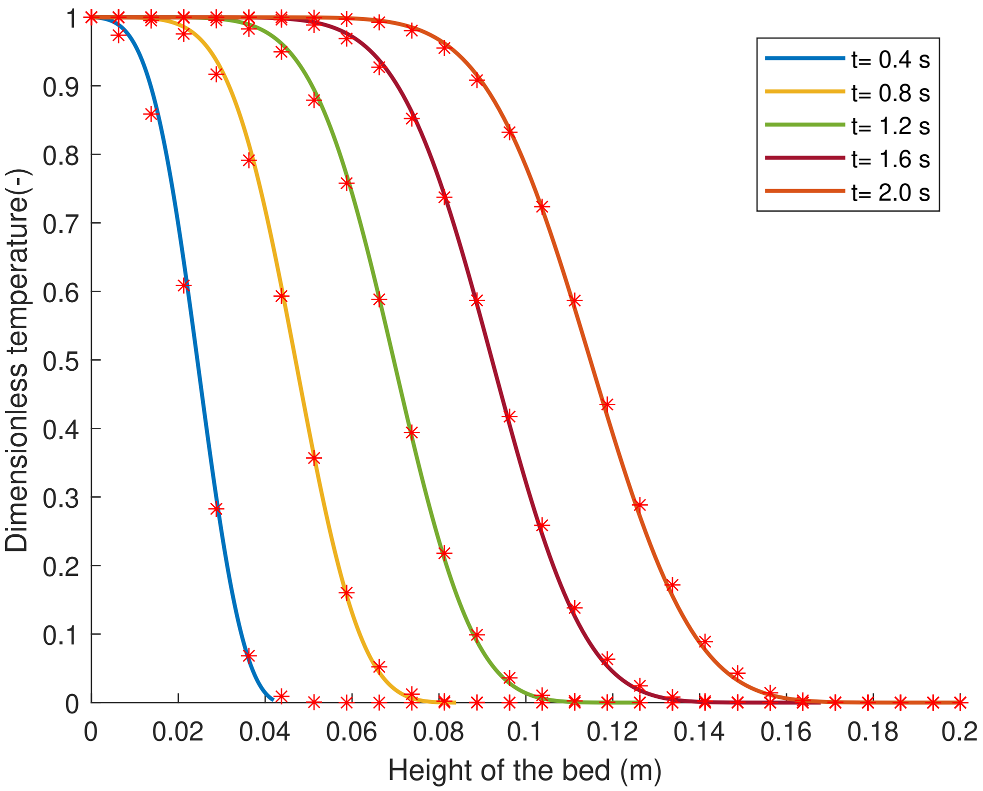

Fig. 4.5 Verification of the two-way heat transfer between CFD and DEM. Lines: analytical solutions. Symbols: simulation results.

4.3.2 Components coupling

The mass transfer is verified using a third test case. A single catalyst particle is surrounded by fluid with a terminal velocity, Figure 4.3-left. A first-order reaction occurs inside the particle and internal and external mass transfer limitations are negligible. A solid product forms and remains on the particle. The weight gain of the particle can be calculated from equation 4.37.

$$m_{MGM}(t) = 4\pi r_g^2 \cdot N_g \cdot k_{reaction} \cdot M_{bulk} \cdot MW_{prod} \cdot t \tag{4.37}$$

where r_g is the grain radius, N_g is the number of grains in the MGM model, $k_{reaction}$ is the surface reaction rate, M_{bulk} is the concentration of the reactant in the bulk of the gas, MW_{prod} is the molar weight of the formed solid, and t is time. Figure 4.6 compares the simulation results with the analytical solution and verifies the mass balance and solid formation implementation.

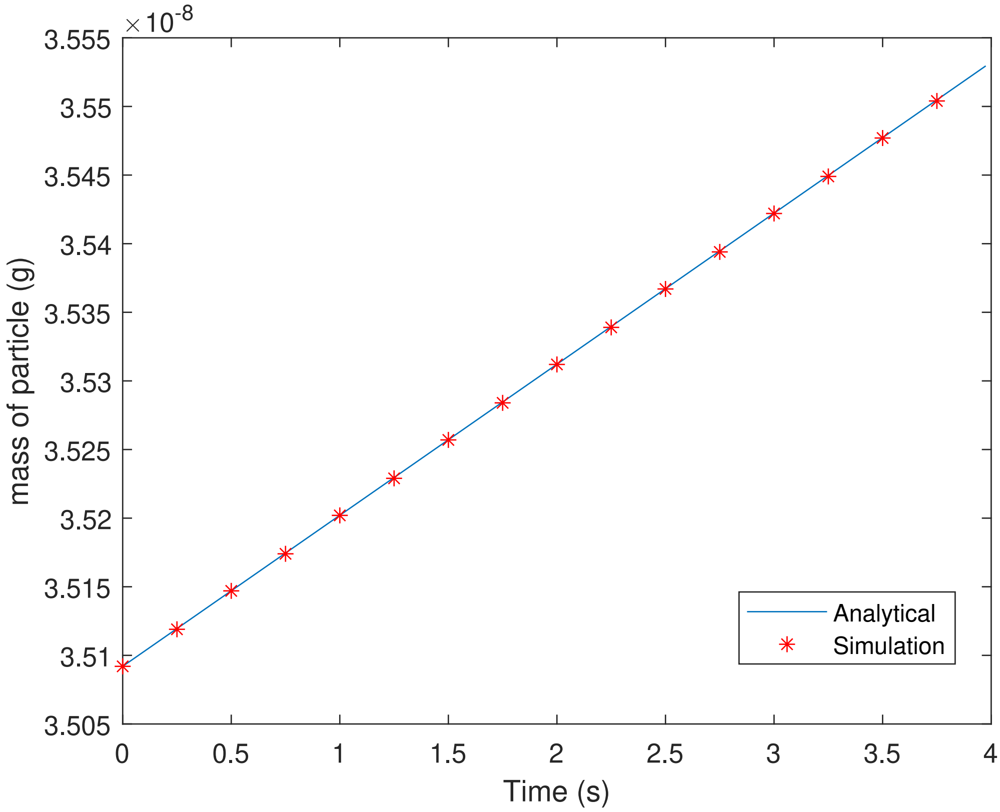

Fig. 4.6 Comparison of mass of the particle over time calculated from analytical solution and simulation.

In order to verify the two-way fluid-particle mass transfer, a packed bed of 31250 ($25 \times 25 \times 50$) particles was considered, Figure 4.3-right. Three components with different mass transfer coefficients and conditions are considered:

- Component-1: no mass transfer between the phases is considered.
- Component-2 has a mass transfer coefficient of $0.005\ \mathrm{m/s}$ and component 2 reacts with a high reaction rate inside the particle.
- Component-3 has a mass transfer coefficient of $0.01\ \mathrm{m/s}$ and has a constant concentration inside the particle ($0.1\ \mathrm{kg/m^3}$) which is higher than the fluid inlet.

The fluid density and particles' size are constant and the flow velocity is unaffected by the added or removed mass (i.e., the fluid is incompressible). In this case, the component concentration along the bed is governed by equation 4.38:

$$M_{f,i}(z) = M_{p,i} + (M_{f,i,in} - M_{p,i}).exp\left(\frac{-k_{m,a,i}a_d z}{u_f}\right) \tag{4.38}$$

$M_{f,i,in}$ represents the inlet condition. a_d is the exchanging surface area per unit length of the bed, and z is the position along the height of the packed bed. Figure 4.7 shows that the analytical and simulation results are in good agreement, and therefore, the implementation is verified.

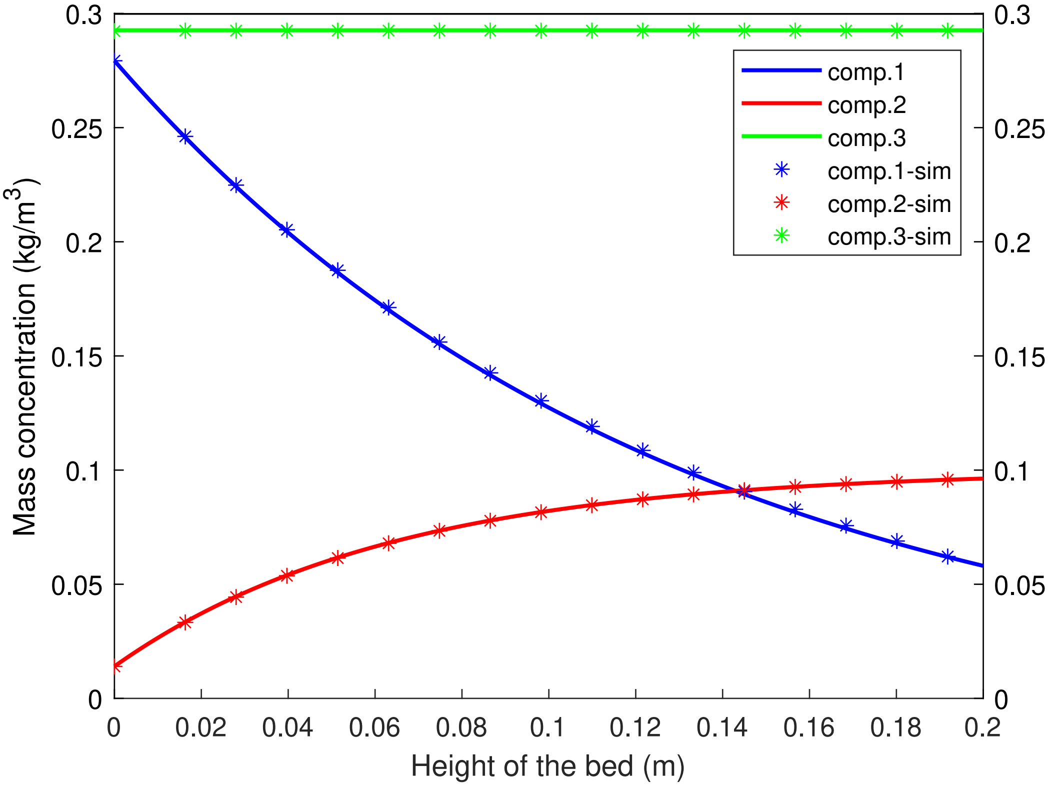

Fig. 4.7 Comparison of the components' concentrations along the bed's height, obtained from analytical solution and simulation.

4.3.3 Added/removed mass to/from the gas phase

The removed (or added) mass from/to the fluid phase will affect the fluid phase. A packed bed of 31250 ($25 \times 25 \times 50$) particles is assumed in a fluid with a constant density to verify this effect. Each particle adds a constant source term of $\Psi = 3 \times 10^{-8}\ kg/s$ to the fluid. As a consequence, the fluid velocity along the bed can be calculated with equation 4.39:

$$u_f(z) = u_f(0) + \frac{\Psi n_p}{\rho_f \varepsilon_f A_c} z \tag{4.39}$$

where n_p is the number of particles in the unit height of the packed bed, and A_c is the cross-sectional area of the bed. Figure 4.8 compares the analytical solution and simulation results and verifies the correct implementation of the model. The deviation at the inlet and outlet is due to the change in porosity because of the begin and end position of the packing.

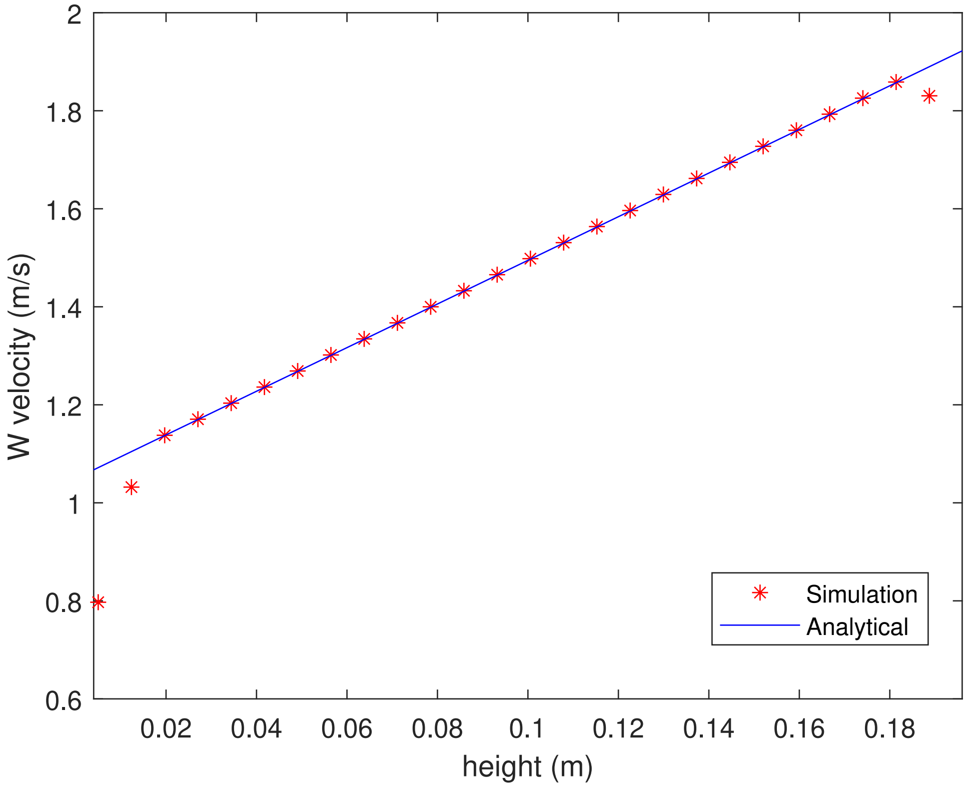

Fig. 4.8 Comparison of the fluid's vertical velocity along the bed's height, obtained from analytical solution and simulation.

4.3.4 Integral mass balance of the reactor

In order to verify the conservation of mass along the reactor, a column with dimensions of $0.1\ m \times 0.1\ m \times 0.5\ m$ was considered with 800 fixed particles at the height of 0.1 m. A constant feed of 70 vol.% inert and 15 vol.% of each reactant and product is introduced. The flux of each component entering and leaving the column is calculated. In the case of a product and reactant containing similar molar weights, the ratio of the gain in the mass of the product to the loss of the mass of the reactant should match the reaction stoichiometry. This factor was evaluated with different reaction stoichiometric ratios and the error was always below 0.03%.

4.4 Results and discussion

4.4.1 Case description

In order to demonstrate the capability of the newly developed CFD-DEM-MGM model, a fluidized bed reactor of catalyst particles is modeled. An arbitrary equilibrium reaction is chosen to occur inside the catalyst particles, represented by expression 5.18 and rate equation 4.41. Table 4.1 shows the most important simulation settings. The particle size increases over time, resulting in altered bed hydrodynamics. Secondly, the balance between the mass transfer limitations and evolving catalytic reaction is gradually changing. Figure 4.9 shows snapshots of the catalyst particles in the center of the reactor (0.02 m depth) colored according to the radius after 3.5 s (left) and 8 s (right). In the next sections, the evolution of these parameters is evaluated in more detail.

$$2\,\mathrm{A(g)} \rightleftharpoons 2\,\mathrm{B(g)} + \mathrm{C(s)} \qquad \Delta H_{(298K)} = +74.5\,kJ/mol \tag{4.40}$$

$$-r_A = k\left({P_{CH_4}}^2 - \frac{{P_{H2}}^2}{K_p}\right) \tag{4.41}$$

Table 4.1 Simulation settings and properties.

Name	Value	Unit
Reactor dimensions	$0.1 \times 0.1 \times 1$	m
Field grid size	$20 \times 20 \times 160$	-
Inlet gas velocity	3.5	m/s
Inlet gas temperature	850	K
Inlet gas composition	$80 - 15 - 5$	vol.%$(A - B - \text{inert})$
Initial reactor temperature	800	K
Initial reactor composition	$5 - 10 - 85$	vol.%$(A - B - \text{inert})$
Number of particles	25000	-
Particles initial diameter	4	mm
Number of grain layers in particles	20	-
Particle density	1309	kg/m^3
Geldart classification type	D	-

4.4.2 Particle size growth

As the reaction evolves over time inside the catalyst particles with accompanying solid product formation, the catalyst particle size increases over time. As a result the bed height increases. Figure 4.10-left shows particles grow as the reaction occurs. During the initial phase, there is no product layer around the grains and therefore, no mass and heat transfer resistance prevails in the grains; therefore, the radius increases at a higher rate compared to a later stage in this process.

Although the particles at the bottom of the reactor are experiencing a higher reaction rate due to the higher reactant concentration and lower product concentration, Figure 4.10-right shows that initially, particles grow at a uniform rate due to the intense bed mixing under the influence of vigorous fluidization and therefore the particle size distribution is very narrow. However, as it is mentioned in section 5.3.3 mixing of particles is reduced over time and, therefore a wider particle size distribution is obtained in the later stages. As it is visible in the snapshots of Figure 4.9, there is a gradient of size along the height of the reactor.

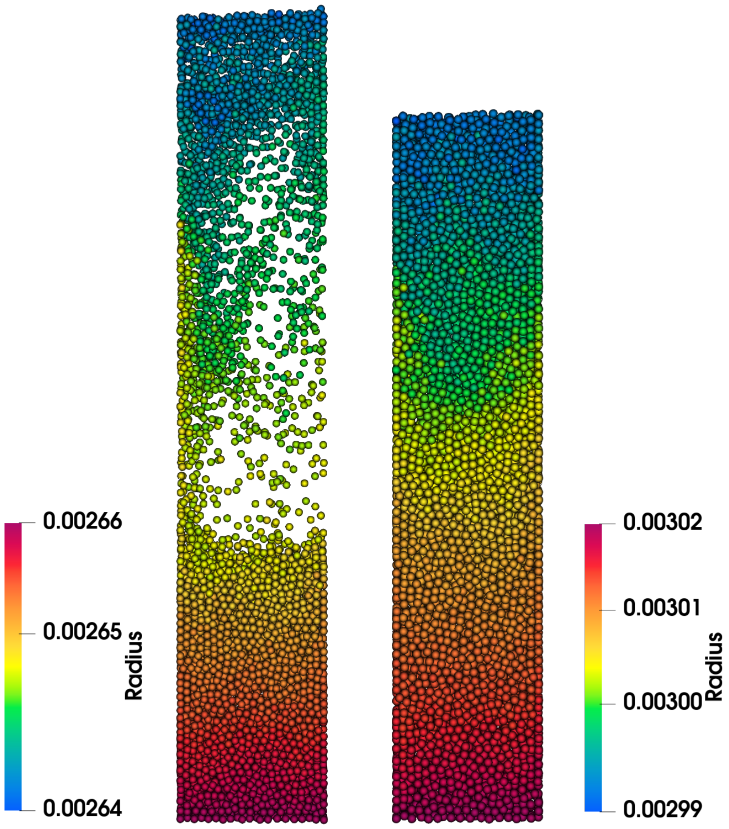
0.00266
0.00265
Radius
0.00264
0.00302
0.00301
0.00300
Radius
0.00299

Fig. 4.9 Illustration of the particles in the center of the reactor (0.02 m depth) colored according to the radius after 3.5 s (left) and 8 s (right).

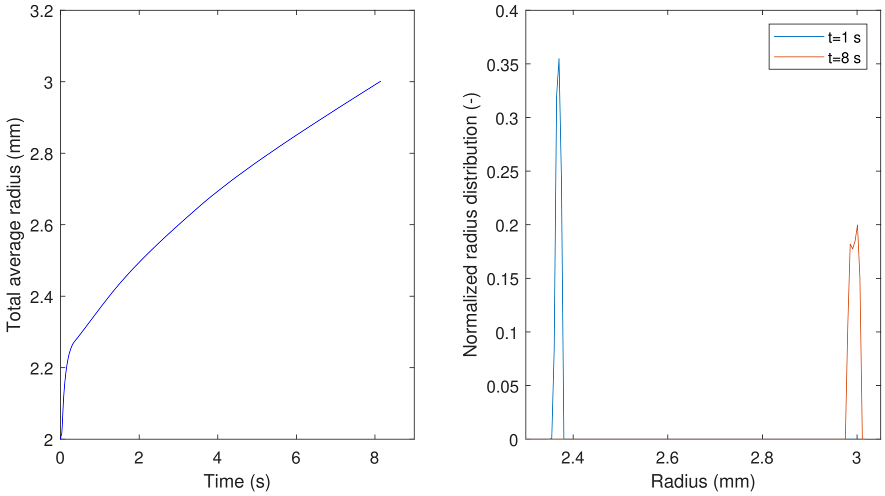

Fig. 4.10 Left: the average size of all particles in the reactor over time. Right: normalized particle size distribution after 3.5 and 8 seconds of the start of the reaction.

4.4.3 Fluidization regime

Since the larger particles are heavier and require a higher gas velocity in order to remain fluidized, the excess velocity decreases with the associated impact on fluidization characteristics over time. Figure 4.11 shows the porosity at the central plane of the bed at different times. It is obvious that in early times bubbles and slugs are formed, however after 6.5 s, the bed is completely defluidized, whereas the height of the bed has expanded considerably.

Figure 4.12 shows the average ratio of the drag force imposed on the particles to the minimum required drag force for the fluidization of the bed (which is the buoyant weight of the particles). Initially, particles descend and accumulate at the bottom of the reactor, causing a reduction in bed porosity. This reduction in porosity induces a high gas velocity, resulting in significant drag force on the particles. Consequently, the particles are propelled upward within the bed, leading to the formation of slugs. The expansion of the bed height caused by slug formation subsequently diminishes the bed porosity, thereby reducing the drag force exerted on the particles. As a consequence, the particles descend once again toward the bottom of the bed, initiating a recurring cycle of particle movement. The reduction in the fluctuations shows that the intensity of bubble formation is reduced until, eventually the bed is defluidized. Furthermore, the frequency of the fluctuations is also reduced, confirming the hydrodynamic regime change.

Figure 4.13 depicts the solids' motion at three different times. Initially, particles experience significant vertical movements. Over time, the solid mobility is reduced. Eventually, the bed is defluidized, and the only movement is due to particle growth and the consequence of bed height expansion.

Figure 4.14-left demonstrates the initial formation of bubbles at the bottom of the reactor, which rapidly transition into slugs as they ascend. Nevertheless, as the slugs reach higher heights within the reactor, the particles above them descend and disrupt them, causing them to break into smaller bubbles once again (Figure 4.11).

In the later stages of the process, the minimum gas velocity required for fluidization increases. Consequently, the excess gas velocity decreases, forming smaller bubbles (Figure 4.14-right), compared to the initial stages. This change in bubble size distribution is attributed to the elevated minimum fluidization velocity, which affects the overall fluidization behavior and the resulting bubble dynamics.

4.4.4 Diffusion limitation

If the reaction rate is assumed to be pseudo-first-order as equation 4.42, then the impact and importance of the fluidization regime and particle size on the performance of the process can

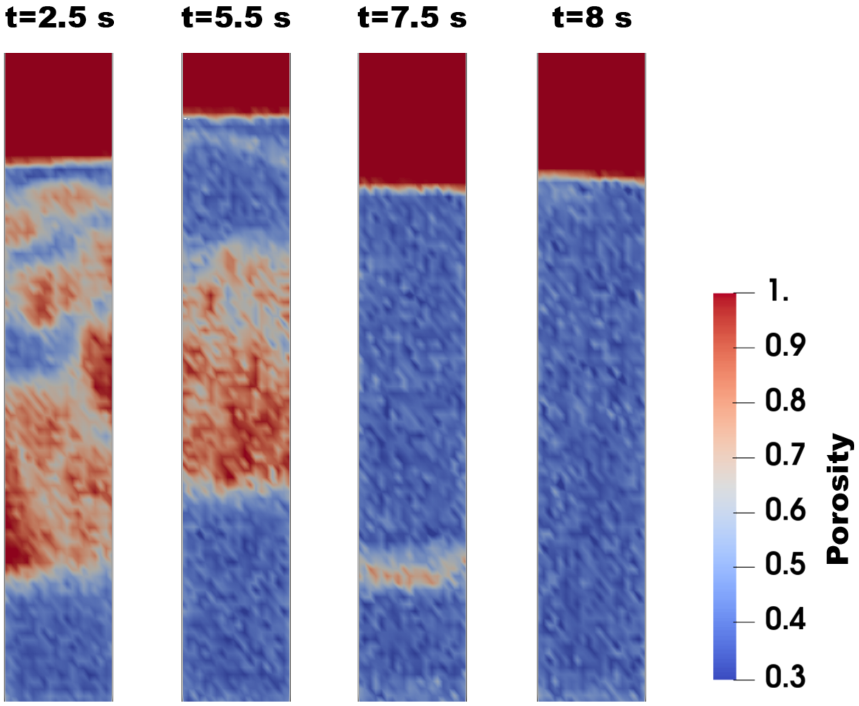

Fig. 4.11 Snapshots of the porosity at the central sheet of the bed over time.

be evaluated by the second Damköhler number (Da_{II}). This number represents the ratio of the chemical reaction rate, to the external mass transfer rate, as given by 4.43 [97]. Where k_m is the mass transfer coefficient calculated from equation 4.22, while the indices s and $bulk$ refer to surface and local concentrations and temperature.

$$-r'_A[\frac{mol}{m^3\,.\,s}] = \hat{k}_1\,[\frac{1}{s}]C_A[\frac{mol}{m^3}] \tag{4.42}$$

$$Da_{II} = \frac{R_p\,\hat{k}_1\,C_{A,s}}{3\,k_m\,C_{A,bulk}} \tag{4.43}$$

To linearize the actual reaction kinetics (as shown in Equation (4.41)) to first order, a unit conversion is necessary, which is described by Equation (4.44). Consequently, the rate constant of the pseudo-first-order reaction rate is determined by Equation (4.45).

$$-r_A[\frac{mol_A}{g_{freshcat}s}] \times 10^3[\frac{g_{freshcat}}{kg_{freshcat}}] \times \frac{m_0}{V_p}[\frac{kg_{freshcat}}{m^3}] = -r'_A[\frac{mol_A}{m^3\,s}] \tag{4.44}$$

$$\hat{k}_1 = \frac{-r_A \times \frac{m_0}{V_p} \times 10^3}{C_A} \tag{4.45}$$

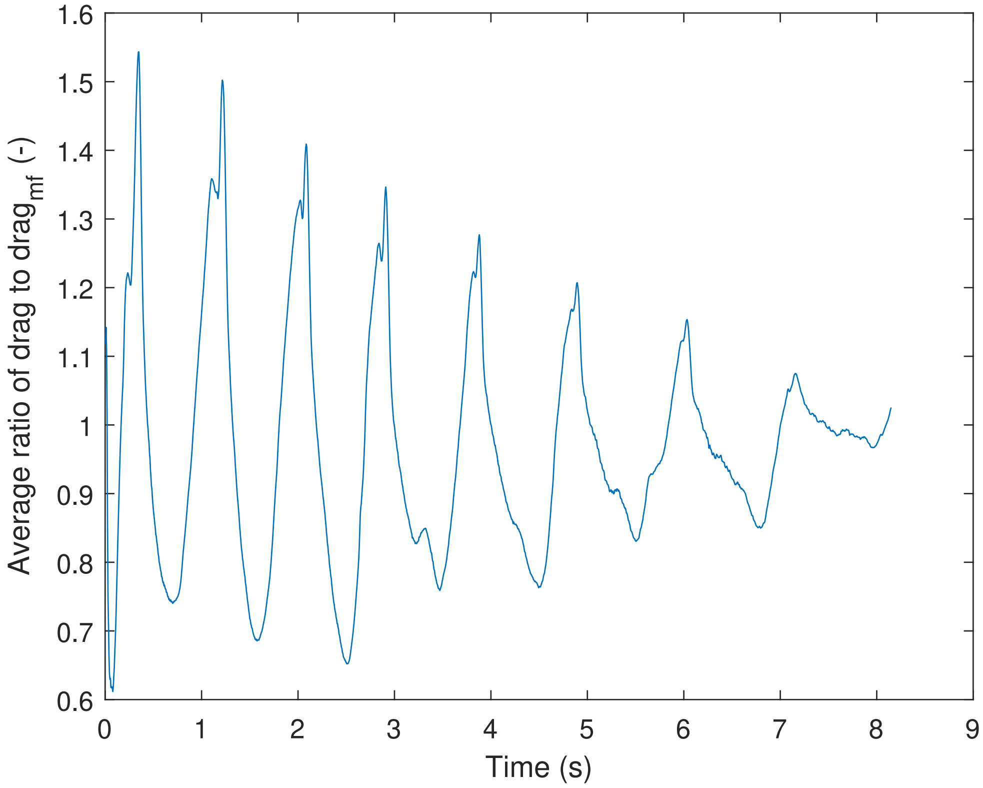

Fig. 4.12 Average ratio of the drag force on the particles to the minimum required drag force for fluidization of particles.

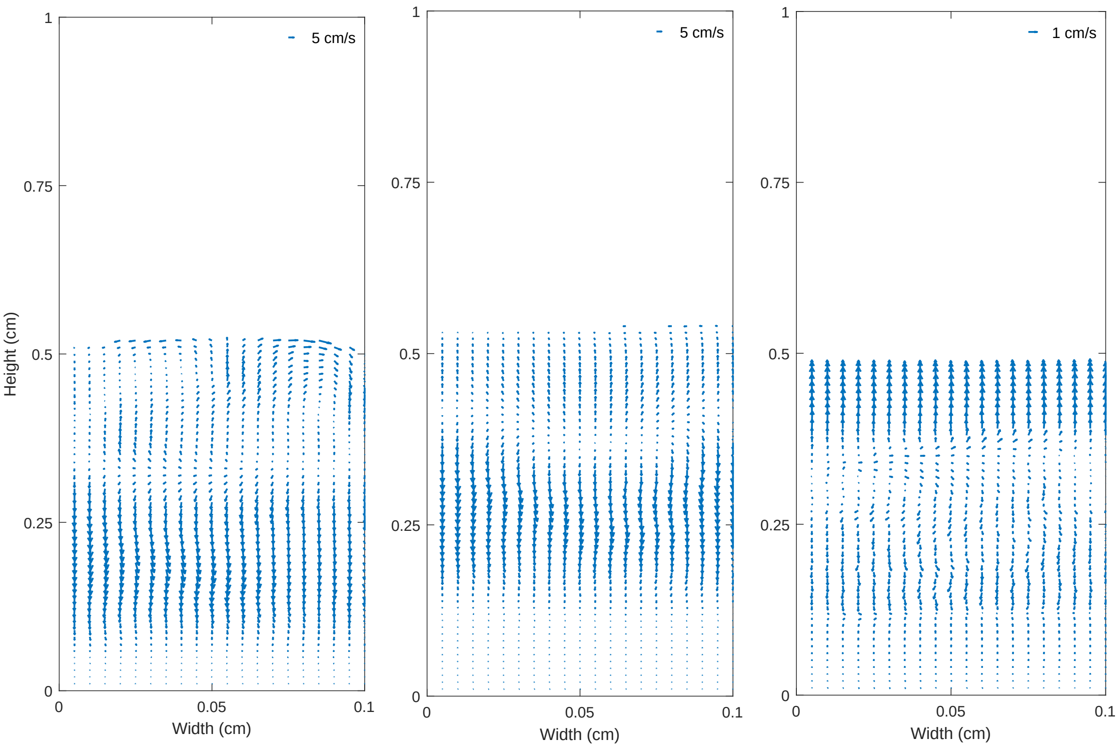

Fig. 4.13 Instantaneous solids velocity at different times (left: 2.5 s, middle: 5.5 s, right: 8 s). Please note the scale differences. Over time the solid mobility and mixing are reduced.

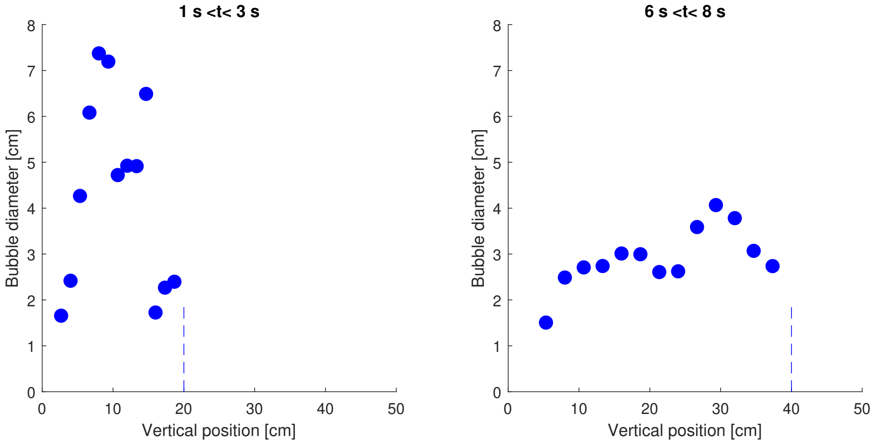

Fig. 4.14 Average bubble size along the bed height between 1 s< t <3 s (left) and 6 s< t <8 s (right). Dash lines show the cut-off height for bubble detection, and represent the approximate bed height.

Figure 4.15 illustrates the gradual decrease of Da_{II} over time, attributed to the reduction in $\hat{k}_1$ resulting from the declining density of active sites per unit volume of the particle, which is inversely proportional to the third power of R_p. The magnitude of Da_{II} suggests that the influence of external mass transfer limitations on the reaction rate and reactor performance can be considered negligible throughout the entire process duration. By comparing Figures 4.12 and 4.15, it is evident that the Da_{II} closely follows the hydrodynamic behavior and exhibits the same oscillation frequency due to the dependency of the mass transfer coefficient on the relative velocity between the particles and the gas phase.

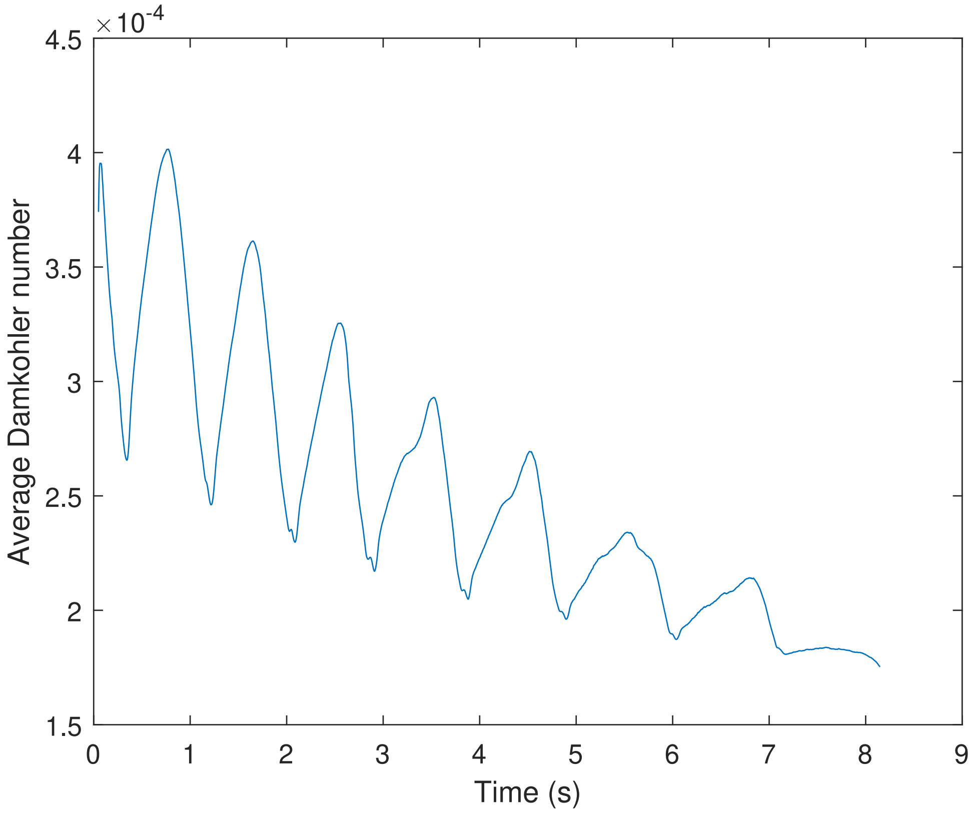

Fig. 4.15 The average Da_{II} of the particles gradually decreases over time due to particle growth and a lower density of active sites in larger particles. The fluctuations follow the hydrodynamics of the bed..

On the other hand, the increase of particle size and the formation of solid products can alter the diffusional limitations of the process. This effect can be assessed by analyzing the Thiele modulus (ϕ^2), which represents the ratio of the chemical reaction rate to the pore diffusion rate. For the assumed pseudo-first-order reaction rate (equation (4.42)), the calculation of ϕ^2 is performed using Equation (4.46) [97, 98].

$$\phi^2 = R_p^2 \frac{\hat{k}_1}{D^{\mathrm{eff}}(4.46)}$$

Figure 4.16 demonstrates the decreasing trend of ϕ^2 over time, primarily due to the diminishing value of $\hat{k}_1$, which exhibits an inverse relationship with the third power of R_p. Despite the external mass transfer limitation, ϕ^2 emphasizes that the diffusional effect cannot be disregarded and its significance may vary throughout the course of the process.

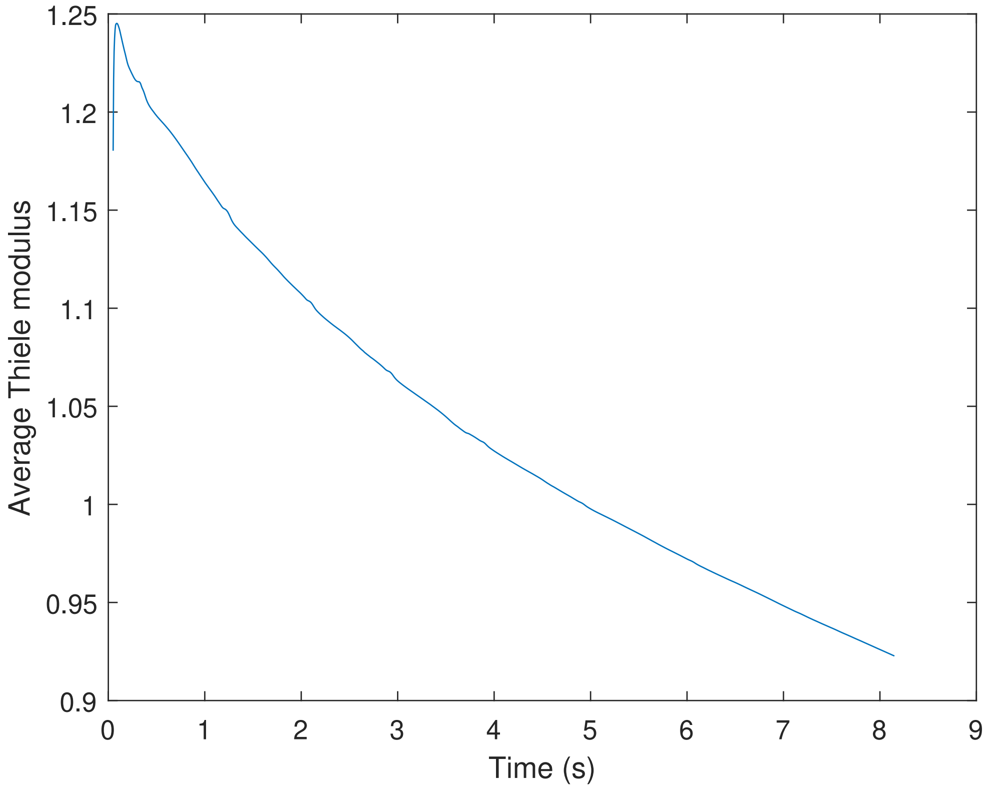

Fig. 4.16 The average ϕ^2 of the particles decreases over time. The graph highlights that pore diffusion limitations are comparatively as significant as the reaction kinetics for the given pseudo-first-order reaction rate.

4.5 Conclusions

A CFD-DEM-MGM model for growing catalyst particles inside a reactor has been developed to study particle growth's impact on the bed hydrodynamics and heat and mass transfer rates. The CFD-DEM-MGM was verified in different aspects such as two-way heat and mass transfer by comparing results with trusted analytical solutions. In order to assess the capabilities of the model and evaluate its effectiveness in replicating the dynamic behavior of the reactor system, a simulation was conducted on a fluidized bed reactor consisting of catalyst particles exhibiting an arbitrary reaction.

Initially, the particle size increased uniformly inside the reactor due to good solid mixing. However, the increase of the particle size led to changing fluidizing behavior and a reduced solids mixing rate. Eventually, complete defluidization of the fluidized bed reactor was observed. As a result, a particle size gradient was noted along the height of the reactor.

For the chosen arbitrary reaction, the external mass transfer limitation remained negligible despite the slightly increased Damköhler number. On the other hand, internal mass transfer is slowly becoming important as the particle size further increases. However, the presented results indicate that the model is capable of coupling the effects of hydrodynamics in a fluidized bed with reacting and growing particles, incorporating the effects of mass and heat transfer.

آری آری زندگی زیباست
زندگی آتشگهی دیرنده پابرجاست
گر بیفروزیش رقص شعله‌اش در هر کران پیداست
ورنه خاموشست و خاموشی گناه ماست

سیاوش کسرائی

Yes, indeed, life’s beauty is clear,
An aged fireplace, it seems,
When you kindle it without fear,
Flames dance, illuminating dreams.
Yet if you don’t ignite the blaze,
It rests in stillness.
And being still, our sin it portrays.

Siavash Kasrai

5

Numerical modeling of TCD in fluidized bed reactors[1]

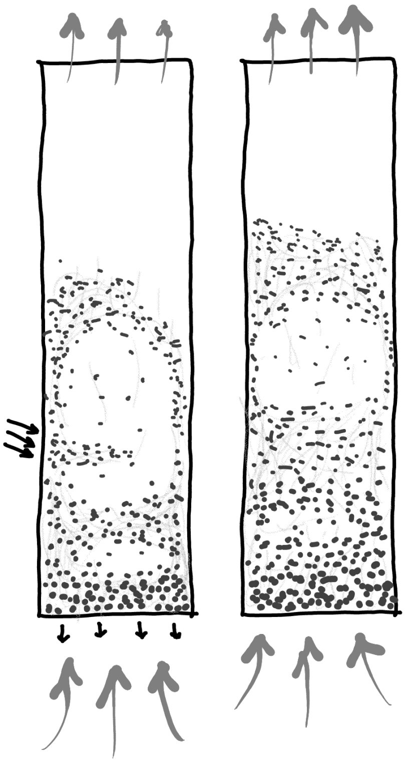

---

[1] This chapter is based on *M. Hadian, J. G. Ramírez, M. J. A. de Munck, K.A. Buist, A.N.R. Bos, J.A.M. Kuipers, (2023), Comparative analysis of a batch and continuous fluidized bed reactors for thermocatalytic decomposition of methane: a CFD-DEM-MGM approach. Submitted to Chemical Engineering Journal*

Abstract

ThermoCatalytic Decomposition of methane (TCD) has shown great potential for the synthesis of valuable carbon nanomaterials as well as hydrogen production. This chapter employs the Computational Fluid Dynamics-Discrete Element Method-Multi Grain Model (CFD-DEM-MGM) to investigate two fluidized bed reactors with the same dimensions for TCD. Case-1 involved a batch of catalyst particles, while Case-2 featured the continuous removal of catalyst particles from the bottom and the introduction of fresh particles from the side. The results revealed that the limited residence time of catalyst particles in the continuous reactor, compared to the batch reactor, leads to lower growth and deactivation. In contrast, the continuous reactor demonstrated higher carbon production and gas conversion rates due to the continuous introduction of fresh catalyst particles. Additionally, the presence of larger catalyst particles in Case-1 resulted in a significant reduction in bubble formation frequency during the later stages of the process. In Case-2, the continuous removal and introduction of particles promoted the break-up of larger bubbles and enhanced horizontal solids mixing. Internal diffusion limitations clearly have an impact on the reactor performance. This study highlights the potential of the CFD-DEM-MGM model for optimizing the design of FBRs and determining the optimal gas-solid contacting operation in TCD processes.

5.1 Introduction

Various methods such as chemical looping reforming, steam methane reforming integrated with Carbon Capture and Sequestration processes (CCS), water splitting, and thermal and thermocatalytic decomposition of methane have been studied to reduce anthropogenic CO_2 emissions [99, 100]. Among these, ThermoCatalytic Decomposition of methane (TCD) is one of the most promising methods due to its potential capability of producing highly valuable carbon nanomaterials in addition to hydrogen [14, 27, 43]. In addition, the feedstock of TCD is abundantly available from both fossil and renewable resources, thus TCD can play a vital role in both transition towards a fossil-free industry and the fossil-free future itself. Another advantage of TCD over conventional hydrogen processes is eliminating the need for complex downstream purification or separation units since no by-products are formed [11].

In TCD, methane is decomposed into solid carbon and gaseous hydrogen with the help of a catalyst at a much lower temperature (500 °C-950 °C) compared to the thermal decomposition temperature exceeding 1300 °C [6]. The structure of the produced carbon material can be in different forms of carbon nano-fibers (CNF), such as fish-bone structures or nano-tubes, depending on operating conditions and the catalyst properties [22, 48, 49]. CNF products are valuable for different industries and are considered as the main product of the process [15]. Among different catalysts, nickel on silica support, $Ni-SiO_2$, has shown a very high methane decomposition activity [10, 12, 16, 29, 60].

Due to carbon accumulation, the catalyst particles in TCD exhibit an increase in size over time. As a consequence, fixed bed reactors encounter significant limitations, such as an elevated risk of clogging, particle breakage, elevated pressure drop, and damage to the reactor's structure. As a result, for large-scale TCD process, Fluidized Bed Reactors (FBR) are preferred over fixed bed reactors [19, 32, 33, 101]. In catalytic fluidized beds, effective phenomena occur on a range of scales, from the micro-scale of porous particles to interactions between particles and the fluid phase. Accurate modeling of these multi-phase phenomena is essential for designing, evaluating, and optimizing the process.

Muradov [42] utilized the Kunii-Levenspiel 1D phenomenological bubbling fluidized bed model to upscale a TCD reactor for producing $50\,\mathrm{ton}_{\mathrm{H}_2}/\mathrm{day}$. Furthermore, a 1D plug flow reactor model was employed to simulate the turbulent flow regime in the reactor [42]. Ammendola et al. [102] used the two-phase phenomenological model and assumed that the produced carbon would be removed from the reactor by attrition and therefore, the catalyst would get reactivated. Although these simple models provide a basic understanding of TCD's potential, they rely on questionable assumptions and fail to incorporate critical phenomena, such as the impact of particle growth on the bed hydrodynamics and the complex interplay between mass and heat transfer and chemical conversion [103].

Multi-scale numerical simulations, such as those performed with the Computational Fluid Dynamics-Discrete Element Method (CFD-DEM), enable engineers to investigate the hydrodynamics of multiphase flows with solid-fluid interactions accompanied by heat and mass transfer in macro-scale industrial chemical processes, such as FBRs [76, 104, 105]. At the micro-scale, the Multi-Grain Model (MGM), predicts particle growth by combining surface reaction and deactivation kinetics with intra-particle heat and mass transfer of reactants and products [11, 69, 70]. Coupled CFD-DEM with MGM combines the potential of both approaches and covers both micro and macro scale phenomena. It allows us to capture the effects of dynamic catalyst characteristics on the reactor conditions and vice versa. CFD-DEM-MGM enables engineers to predict the reactor performance over time and compare different reactor designs.

This work uses the coupled CFD-DEM-MGM model to compare the advantages and drawbacks of two different FBRs. A **batch** FBR is considered in Case-1. Contrary in Case-2, a **continuous** FBR is simulated. In this case, the catalyst particles are removed from the reactor and instead, fresh catalyst particles are injected into the reactor.

The outline of this chapter is as follows: the model and the test cases are described in section 5.2. The results are presented and discussed in section 5.3. Finally, in Section 5.4, the conclusions drawn from this study are presented.

5.2 Model description

The gas phase in the reactor is described by the volume-averaged Navier-Stokes equation (5.1) and the continuity equation (5.2).

$$\frac{\partial(\varepsilon_f\rho_f\mathbf{u}_f)}{\partial t}+\nabla\cdot(\varepsilon_f\rho_f\mathbf{u}_f\mathbf{u}_f)=-\varepsilon_f\nabla P_f-\nabla\cdot(\varepsilon_f\tau_f)+\varepsilon_f\rho_f\mathbf{g}-\mathbf{S}_p \tag{5.1}$$

$$\frac{\partial(\varepsilon_f\rho_f)}{\partial t}+\nabla\cdot(\varepsilon_f\rho_f\mathbf{u}_f)=\sum_{i=1}^{N_{cell}}S_{m,i} \tag{5.2}$$

In all equations presented, the subscript notation f denotes the fluid phase, while p refers to the particulate phase. The parameter ε denotes the gas volume fraction present within a given cell, while ρ represents the density. The velocity vector of the fluid phase is denoted by $\mathbf{u_f}$, with P_f denoting the pressure. $\mathbf{S}_p$ is the momentum source term that accounts for the coupling of momentum exchange between the fluid and particles. This coupling is described by equation (5.3):

$$\mathbf{S_p}=\frac{1}{V_{cell}}\sum_{a=0}^{N_p}\frac{V_{p,a}\beta_a}{1-\varepsilon_f}(\mathbf{u}_f-\mathbf{v}_{p,a})D(\mathbf{r}-\mathbf{r}_{p,a}) \tag{5.3}$$

where V_{cell} and $V_{p,a}$ represent the local cell volume and the volume of particle a. The polydisperse drag coefficient correlations presented by Sarkar and Beetstra [87, 88] are utilized in the calculation of the inter-phase momentum exchange coefficient, β, owing to the growing nature of particles. Notably, the gas phase viscous stress tensor, denoted as τ_f and given by equation 5.4, is assumed to follow the general Newtonian form.

$$\tau_f=-\mu_f\left[(\nabla\mathbf{u}_f)+(\nabla\mathbf{u}_f)^T-\frac{2}{3}(\nabla\cdot\mathbf{u}_f)\mathbf{I}\right] \tag{5.4}$$

where μ_f is the shear viscosity, and $\mathbf{I}$ is unity tensor. $S_{m,i}$ is the mass source term of the component i in the cell. The gas density, ρ_f is calculated according to the ideal gas law.

The gas phase thermal energy balance is given by equation 5.5:

$$Cp_f\left[\frac{\partial(\varepsilon_f\rho_f T_f)}{\partial t}+\nabla\cdot(\varepsilon_f\rho_f\mathbf{u}_f T_f)\right]=\nabla\cdot(\varepsilon_f K_f^{\text{eff}}\nabla T)+Q_p \tag{5.5}$$

T is temperature, and K_f^{eff} is the effective thermal conductivity of the fluid. Q_p represents the energy source term originating from the energy transport between the fluid and the particulates is defined by equation 5.6.

$$Q_p=\frac{1}{V_{cell}}\sum_{a=0}^{N_p}h_{p,a}A_{p,a}(T_{p,a}-T_f)D(\mathbf{r}-\mathbf{r_{p,a}}) \tag{5.6}$$

where $A_{p,a}$ is the heat exchanging surface area of particle a, and h_a heat transfer coefficient is calculated using the Gunn correlation.

The component mass balance is described by equation 5.7 considering convection, diffusion and inter-phase transfer source term:

$$\frac{\partial(\varepsilon_f M_{f,i})}{\partial t}+\nabla\cdot(\varepsilon_f M_{f,i}\mathbf{u_f})=\nabla\cdot(\varepsilon_f D_{f,i}^{\text{eff}}\nabla M_{f,i})+S_{m,i} \tag{5.7}$$

where $M_{f,i}$ is the mass concentration of component 'i' in the fluid, $D_{f,i}^{\text{eff}}$ is the effective diffusivity of component i in the fluid, and $S_{m,i}$ is the gas-particle mass source term transfer of component i and is calculated from equation (5.8).

$$S_{m,i}=\frac{1}{V_{cell}}\sum_{a=0}^{N_p}k_{m,a,i}A_{p,a}(M_{p,a}-M_i)D(\mathbf{r}-\mathbf{r_{p,a}}) \tag{5.8}$$

where the mass transfer coefficient of component i between particle a and fluid, $k_{a,i}$, is determined by the Gunn correlation.

The trajectory of each particle is determined by Newton's second law, equation 5.9. The forces imposed by the pressure gradient of fluid, drag force, gravitational force and collisional forces determine the acceleration of the particle. The particle-particle and particle-wall collisions are described by the soft-sphere model developed by Cundall and Strack [91] using a linear spring and dashpot model [91–93, 106].

$$m_{p,a}\frac{d\mathbf{v}_{p,a}}{dt}=m_{p,a}\frac{d^2\mathbf{r}_{p,a}}{dt^2}=-V_{p,a}\nabla P_f+\frac{V_{p,a}\beta_{p,a}}{1-\varepsilon_f}(\mathbf{u}_f-\mathbf{v}_{p,a})+m_{p,a}\mathbf{g}+\sum\mathbf{F}_{contact,p,a} \tag{5.9}$$

in which $\mathbf{r}_{p,a}$ and $m_{p,a}$ are the position and the mass of the particle a.

The rotational motion of the particle is tracked using equation (5.10).

$$I_{p,a}\frac{dw_{p,a}}{dt} = \mathbf{T}_{p,a} = \sum_{\text{b}\in\text{contact list}} (r_{p,a}\mathbf{n}_{ab} \times \mathbf{F}_{ab,t}) \tag{5.10}$$

where $I_{p,a}$ is the moment of inertia, $w_{p,a}$ is the rotational velocity and $\mathbf{T}_{p,a}$ is the torque.

MGM models each particle as a porous medium, whereby the catalyst support is represented by multiple layers of solid, non-porous grains uniformly covered with active material on their surfaces, as depicted in Figure 5.1. Heat and mass transfer are accounted for in the radial direction at two distinct scales (i.e. catalyst particle and grains), with the reaction taking place on the grain surface [11].

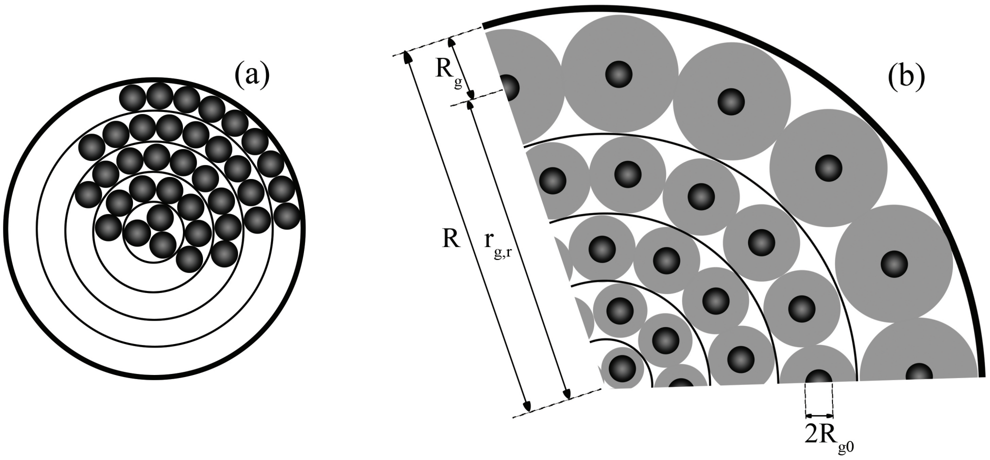

Fig. 5.1 Schematic of MGM model (a) prior to solid formation and growth, and (b) a circular sector of the particle with the accumulated solid product on the grains' surfaces [11].

Species mass balance is solved along the radius of the catalyst particle and each grain via equations 5.11 and 5.12 respectively:

$$\frac{\partial M_{p,a,i}(r,t)}{\partial t} = \frac{1}{r^2}\frac{\partial}{\partial r}\left(D^{\text{eff}}_{p,a,i} r^2 \frac{\partial M_{p,a,i}(r,t)}{\partial r}\right) - R(r,t) \tag{5.11}$$

$$\frac{\partial M(r_g,t)}{\partial t} = \frac{1}{r_g^2}\frac{\partial}{\partial r_g}\left(D_{prod} r_g^2 \frac{\partial M(r_g,t)}{\partial r_g}\right) \tag{5.12}$$

r represents the radial position within the particle, r_g is the radial position within the grain, R_g is the radius of the entire grain. $D^{\text{eff}}_{p,a,i}$ refers to the effective diffusivity of component i in particle a, D_{prod} is the diffusivity in the product layer surrounding the grains for each component, and $R(r,t)$ is the volumetric average reaction rate at a specific radial position within the particle, calculated by averaging the reaction rate in the corresponding grid cell. The actual reaction occurs on the core's surface, which is reflected in the boundary conditions with the unit conversion factor of the kinetic equation (CF), equation 5.13. As a result of the solid product formation on the grain surface, the grain's radius increases, resulting in additional internal diffusion constraints.

$$D_{prod}\frac{\partial M(R_{g0},t)}{\partial r_g} = r(t).CF \tag{5.13}$$

The heat balance is solved for each catalyst particle and each grain layer given by equations 5.14 and 5.15.

$$\frac{\partial T_{p,a}(r,t)}{\partial t} = \frac{1}{r^2}\frac{\partial}{\partial r}\left(\frac{k^{\text{eff}}_{p,a}}{\rho_p C p_p} r^2 \frac{\partial T_{p,a}(r,t)}{\partial r}\right) - \frac{\Delta H}{\rho_p C p_p} R(r,t) \tag{5.14}$$

$$\frac{\partial T(r_g,t)}{\partial t} = \frac{1}{r_g^2}\frac{\partial}{\partial r_g}\left(\frac{k_g}{\rho_{gr} C_{P_g}} r_g^2 \frac{\partial T(r_g,t)}{\partial r_g}\right) \tag{5.15}$$

$k^{\text{eff}}_{p,a}$, ρ_p and Cp_p are the heat conductivity, the density and the specific heat capacity of the particle, respectively. For further details regarding MGM we refer to Hadian et al. [11].

Continuous fluxes are considered as boundary conditions at the particles' surface to couple the intra-particle and fluid heat and mass balances, equations 5.16 and 5.17:

$$@r = R_p \quad -D^{\text{eff}}_{p,a,i}\frac{\partial M_{p,a,i}}{\partial r} = k_{a,i}\left(M_{p,a,i} - M_{f,i}\right) \tag{5.16}$$

$$@r = R_p \quad -k^{\text{eff}}_{p,a}\frac{\partial T_p}{\partial r} = h_a\left(T_p - T_f\right) \tag{5.17}$$

5.2.1 Case description

Two different fluidized bed reactors were compared. In **Case-1**, a batch FBR containing 20,000 particles is simulated. TCD reaction kinetics is given by equations 5.19 and 5.20 with the corresponding parameters in Table 5.1 [29]. Table 5.2 shows the most important settings of the simulation. The particle size increases over time, resulting in changing bed hydrodynamics and reactor performance. In the **Case-2**, a continuous FBR with identical dimensions as Case-1 is simulated. The catalyst particles are removed from the bottom of the reactor at a rate of $8.33\%/s$ (leading to a residence time of almost 12 s), and additionally, fresh catalyst particles are inserted into the reactor from the side of the reactor. The gas flow in the domain was subjected to specific boundary conditions. These conditions included a uniform superficial air velocity of 0.45 m/s at the bottom, no-slip boundary conditions for the side walls, and a fixed pressure boundary condition of 1 atm at the top. Figure 5.2 shows snapshots of the catalyst particles in the reactor colored according to the particle radius after 7.5 s in Case-1 (left) and Case-2 (right). The removal and insertion zones in the continuous test case are depicted in red and green colors, respectively.

$$\mathrm{CH_4(g)} \rightleftharpoons \mathrm{C(s)} + 2\,\mathrm{H_2(g)} \qquad \Delta H_{(298K)} = +74.52\,kJ/mol \tag{5.18}$$

$$r_0 = \frac{k(P_{CH_4} - {P_{H2}}^2/K_p)}{\left(1 + K_{H_2}{P_{H_2}}^{1.5} + K_{CH_4}P_{CH_4}\right)^2} \tag{5.19}$$

$$r(t) = r_0 \times \left(\frac{1}{1 - 0.5k_d\left(k_{d,C} + k_{d,CH_4}P_{CH_4} + k_{d,H_2}P_{H_2}^{0.83}\right)t} \right)^{-0.8} \tag{5.20}$$

Table 5.1 Kinetic coefficients of equations 5.19 (top part) and 5.20 (bottom part) [29].

Coefficient	Parameter	Value	Unit
k	A	5.940×10^4	$\mathrm{mol_{CH_4}/atm_{CH_4}/g_{cat}/min}$
	E	88	kJ/mol
K_{H_2}	A_{H_2}	1.871×10^{-8}	$\mathrm{atm}^{-3/2}$
	ΔH_{H_2}	144	kJ/mol
K_{CH_4}	A_{CH_4}	6.979×10^{-5}	atm^{-1}
	ΔH_{CH_4}	56	kJ/mol
k_d	A_d	18.39	s^{-1}
	E_d	147	kJ/mol
$k_{d,C}$	$A_{d,C}$	309.87	-
	$\Delta H_{d,C}$	26	kJ/mol
k_{d,CH_4}	A_{d,CH_4}	-449.02	atm^{-1}
	$\Delta H_{d,CH_4}$	5.376	kJ/mol
k_{d,H_2}	A_{d,H_2}	-0.349	$\mathrm{atm}^{-0.83}$
	$\Delta H_{d,H_2}$	80.19	kJ/mol

Table 5.2 Simulation settings and properties.

Name	Value	Unit
Reactor dimensions	$2 \times 1 \times 10$	cm
Eulerian grid size	$20 \times 10 \times 80$	-
CFD time step size	10^{-4}	s
DEM time step size	10^{-5}	s
Inlet superficial gas velocity	0.45	m/s
Inlet gas temperature	600	°C
Initial reactor temperature	600	°C
Inlet gas composition	$80-10-10$	vol.%(A – B – inert)
Initial reactor composition	$5-10-85$	vol.%(A – B – inert)
Number of particles	20000	-
Particles initial diameter	500	μm
Number of grain layers in particles	20	-
Particle density	1762	kg/m^3

5.3 Results and discussion

5.3.1 Catalyst deactivation

Catalyst particles deactivate gradually at a rate depending on the reactor's local conditions and residence time. Figure 5.3 illustrates the average deactivation factor of particles within the bed for both scenarios. In the continuous scenario (Case-2), the deactivation factor reaches a plateau due to the constrained residence time of the particles. Conversely, in Case 1 (batch FBR), the deactivation process persists until full deactivation is attained. Figure 5.3 also shows that under steady-state conditions and with the provided solid flow rate, the deactivation factor of the particles removed in Case-2 approximates 0.7.

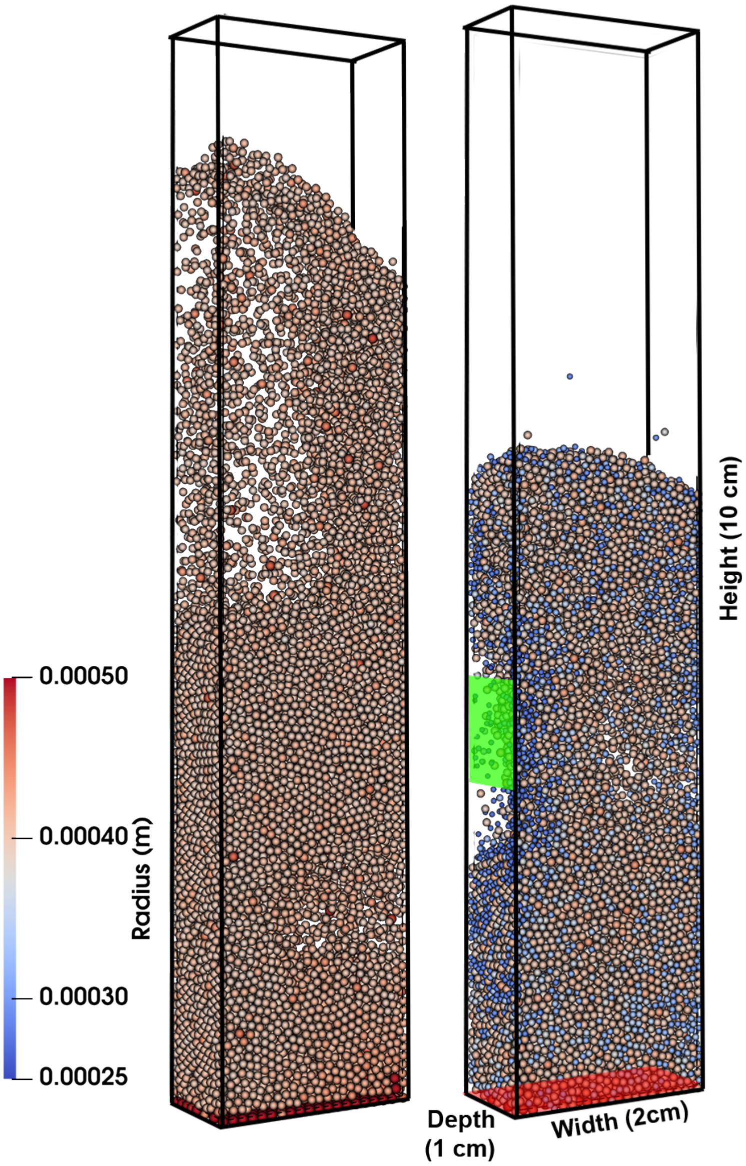
0.00050
0.00040
0.00030
0.00025
Radius (m)
Height (10 cm)
Depth (1 cm)
Width (2cm)

Fig. 5.2 Illustration of the catalyst particles in the reactor colored according to the radius after 7.5 s in Batch FBR Case-1 (left) and Continuous FBR Case-2 (right), including the removal (red) and insertion zones (green).

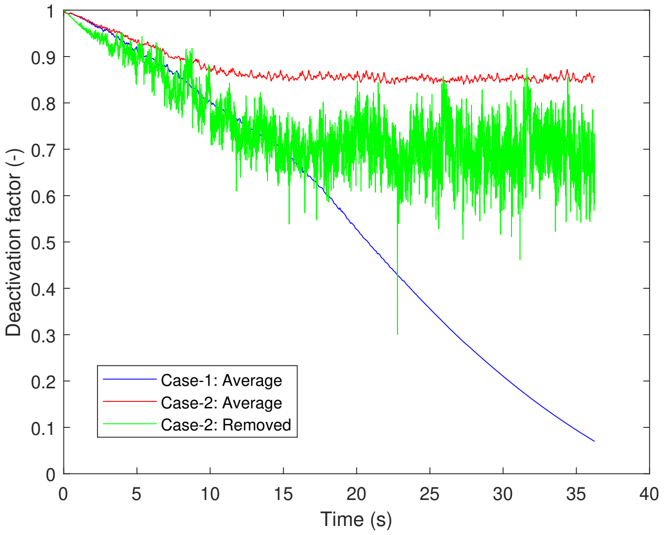

Fig. 5.3 The average deactivation factor of the particles in the bed (Case-1 and Case-2), and the removed particles from the reactor (Case-2).

5.3.2 Particle size growth

Due to the carbon formation, the size of catalyst particles progressively increases during the course of a reaction. Consequently, the bed height expands accordingly. Figure 5.4 compares the average radius of the catalyst particles as a function of time. In Case-2, as the time surpasses the average residence time of the particles, the average radius of the catalyst particles reaches a steady value. Conversely, in Case-1, the particles undergo more extensive growth. Nevertheless, the growth rate diminishes as time evolves.

However, comparing the average radius of the particles is misleading because inserting fresh and small catalyst particles in Case-2 lowers the average radius. Instead, the removed particles from the bed can be compared; see Figure 5.4. Initially, both cases exhibit comparable growth rates. In later stages, due to the experienced higher residence time, Case-1 results in larger particles.

While the particles in Case-1 exhibit a larger size and yield a higher amount of carbon per gram of catalyst utilized, Case-2 demonstrates the capability to generate larger total quantities of carbon. This outcome can be attributed to the enhanced activity of the particles in Case-2. As depicted in Figure 5.5, the cumulative carbon accumulation at the bottom of the reactor in Case-2 surpasses the overall carbon production in Case-1.

In order to maximize the efficiency and cost-effectiveness of the process, an optimal solids flow rate and reactor operation can be determined while taking into account economic parameters. This analysis should consider factors such as capital investment, operating costs

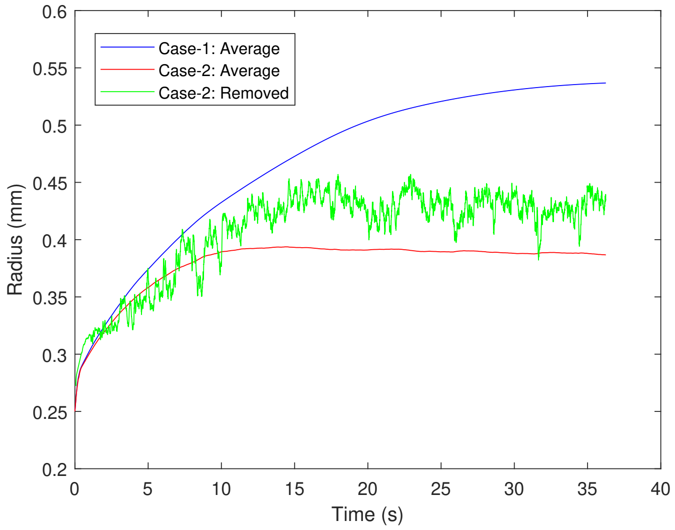

Fig. 5.4 The average radius of the particles in the bed (Case-1 and Case-2), and the removed particles from the reactor (Case-2).

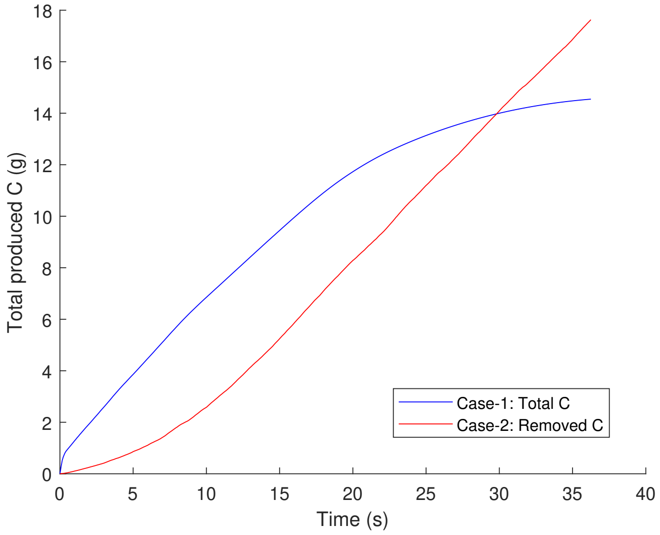

Fig. 5.5 The total mass of produced carbon in Case-1 and mass of carbon removed from the reactor in Case-2 over time.

(including energy consumption, catalyst replacement, and maintenance), product yield and quality, and market demand. By evaluating these economic parameters, it becomes possible to identify the most favorable operating conditions that balance productivity, cost-efficiency, and profitability.

5.3.3 Bed hydrodynamics

The increasing size of catalyst particles leads to an augmented weight, necessitating higher gas velocities to maintain their fluidized state. Consequently, the fluidization intensity and regime experience alterations as time progresses, affecting heat and mass transfer characteristics as well. Figure 5.6 illustrates the pressure drop of the bed in both Case-1 and Case-2. In Case-1, the pressure drop reaches higher values than Case-2 due to the larger mass of solids in the reactor. Notably, at approximately 16 s, the particles begin to collide with the upper boundary of the reactor. Subsequently, at 27 s, the solids completely fill the reactor, resulting in the transformation of the reactor into a constrained Packed Bed Reactor (PBR). In Case-2, the pressure drop does not exceed a maximum value of 355 pa.

The bubble frequency is determined by performing a fast Fourier transform (FFT) on the pressure drop signals. A Lorentz fit is applied to detect the dominant frequencies [106]. From Figure 5.7, it is evident that the frequency of bubble formation in Case-1 has substantially decreased. In contrast, Case-2 demonstrates a relatively consistent bubble formation frequency, maintaining values close to those observed during the initial stages of the process.

Bubble size is a crucial characteristic of a FBR. To obtain the equivalent bubble diameter, a post-processing algorithm is employed. In this algorithm, the bubble regions are identified using a threshold porosity value ($\varepsilon = 0.8$), excluding the freeboard region from the analysis. Additionally, for a void to be classified as a bubble, it must have a minimum size of 2.5 times the grid cell size. The equivalent bubble diameter is derived, assuming the bubble is a sphere.

Figure 5.8 illustrates the initial bubble size distribution in both Case-1 and Case-2, revealing comparable bubble sizes. However, as the bed expands beyond the particle insertion zone, the introduction of new particles in Case-2 leads to the breakup of bubbles into smaller sizes. Above the insertion zone, bubbles are growing at a faster rate (higher slope of the depicted dashed lines), resulting from smaller particle sizes. Conversely, in Case-1, bubbles tend to attain slightly larger sizes, and the bubble growth rate is lower compared to Case-2.

In Figure 5.9, a comparison of Case-1 and Case-2 is presented considering the time-averaged particle velocities. Case-1 exhibits the characteristic particle flow pattern commonly observed in FBRs as particles move upward in the central zone of the bed with bubbles, and descend in the vicinity of the reactor walls. On the other hand, Case-2 demonstrates

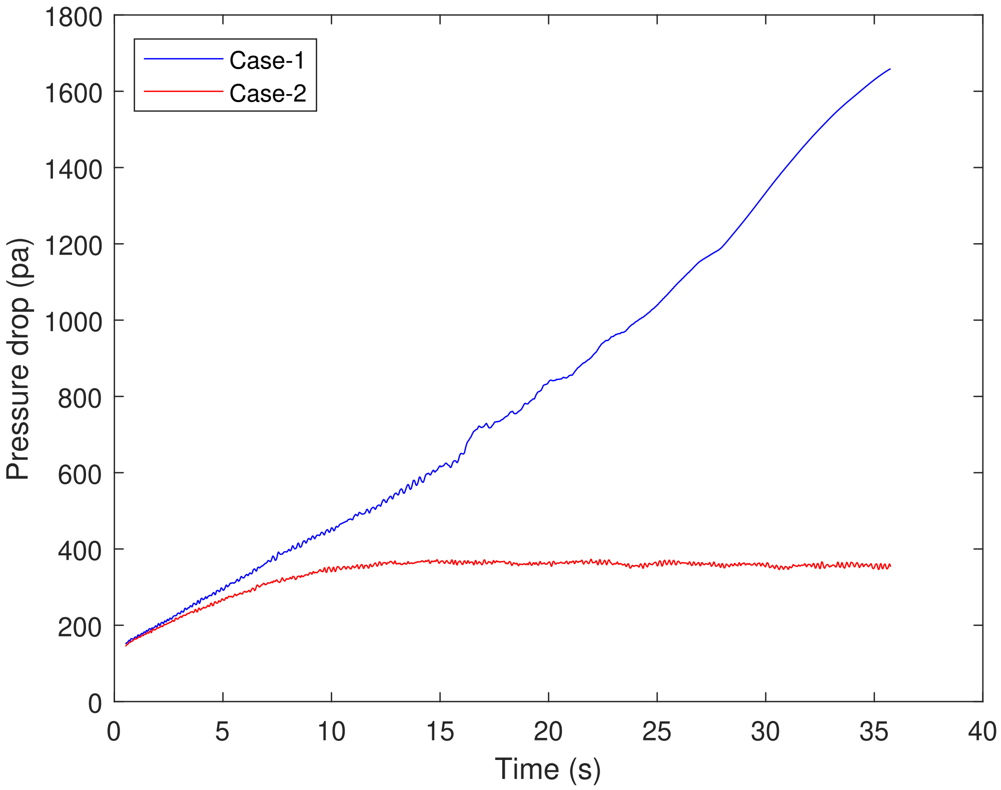

Fig. 5.6 The pressure drop of the bed over time. The notable increase in pressure drop observed in Case-1 is attributed to the larger mass of particles within the bed compared to Case-2.

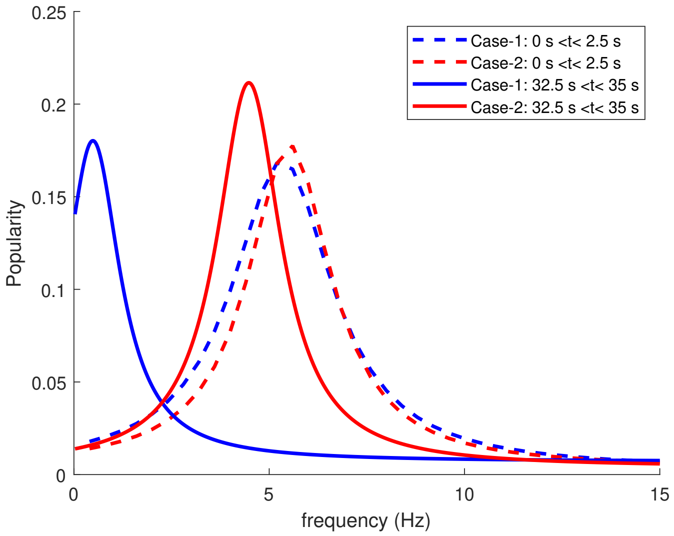

Fig. 5.7 Comparison of the frequency of the bubble formation in Case-1 and Case-2, initially and after 35 s.

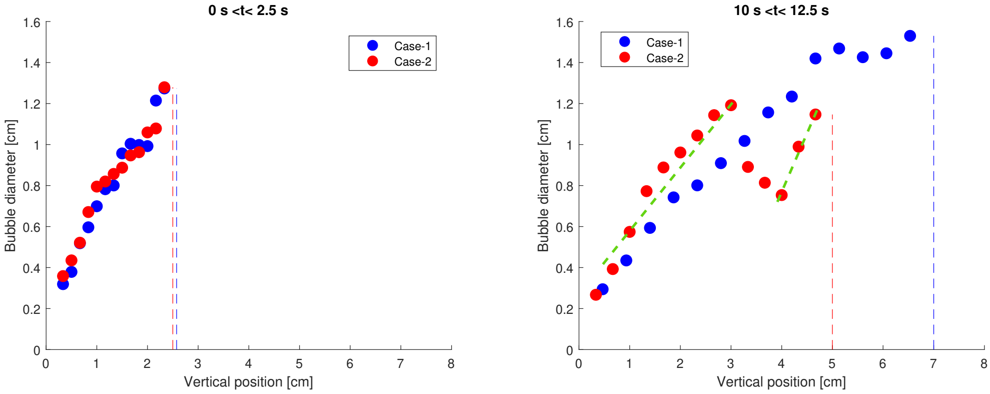

Fig. 5.8 Equivalent bubble diameter as a function of axial position at the onset of the reaction (left) and after 10 s (right) for both cases. The dashed lines indicate the approximate maximum bed height.

shorter and more circulation zones, and higher velocity magnitudes, leading to enhanced solids mixing. It should be noted that the higher bed height in Case-1 is caused by the larger particles (i.e., higher static bed height).

The average instantaneous particle fluxes at the height of 2 cm are shown in Figure 5.10. After 10 s, solids fluxes in both cases show similar magnitudes. In later stages, the solids flux in Case-1 reduces, while in Case-2 it remains high. Within a symmetric fluidized bed, the central region usually experiences an upward motion of solids as the particles are entrained in the wake of ascending bubbles. Conversely, a downward flow of solids is observed in the wall region. However, this pattern is affected due to particle insertion only from one side of the reactor.

5.3.4 Gas conversion

Figure 5.11 depicts a comparison of the gas conversion profiles for both Case-1 and Case-2 (solid lines) against ideal plug flow reactors (PFR) operating under identical conditions. Notably, Case-2 achieves a steady conversion rate, whereas Case-1 experiences a decline owing to catalyst particle deactivation. Consistent with expectations, the gas conversion in a FBR is lower than that of an ideal PFR due to phenomena such as gas bypassing through bubbles and channeling.

It is noteworthy that the qualitative behavior of Case-1 closely resembles the experimental observations of TCD in a FBR as reported by Hadian et al. [29]. Specifically, the conversion commences in a turbulent manner at a maximum conversion, followed by a slight decline leading to a period of stability. Subsequently, the conversion exhibits a gradual decrease with a prolonged tail until complete deactivation occurs.

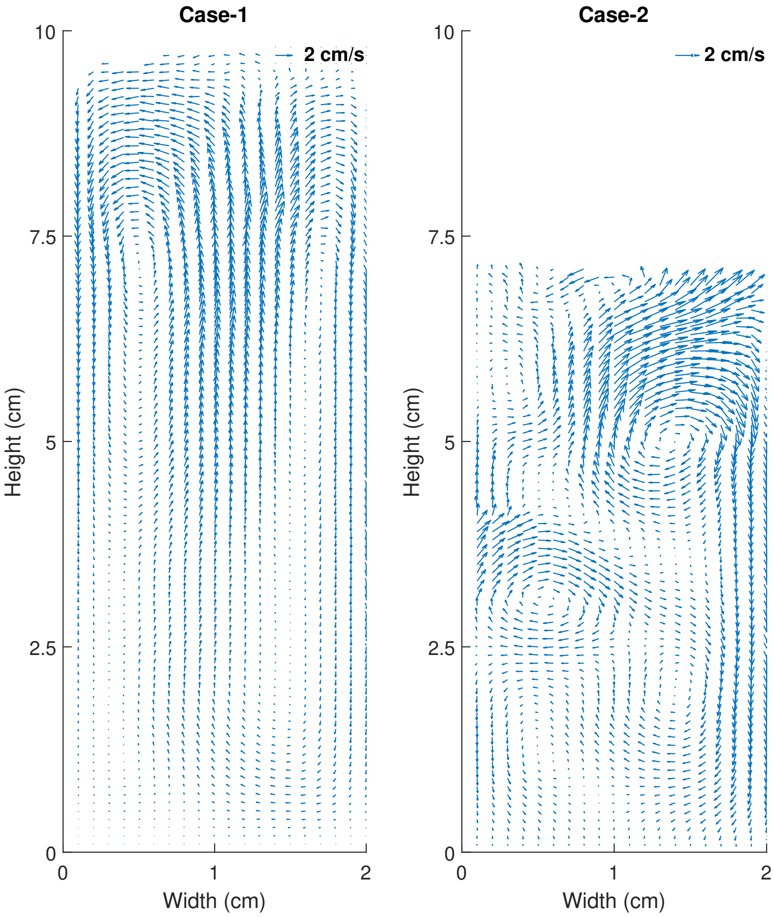

Fig. 5.9 Time-averaged particle velocity between 10 s and 20 s in Case-1 (left) and Case-2 (right). Solid circulation and mixing are improved in Case-2, compared to Case-1.

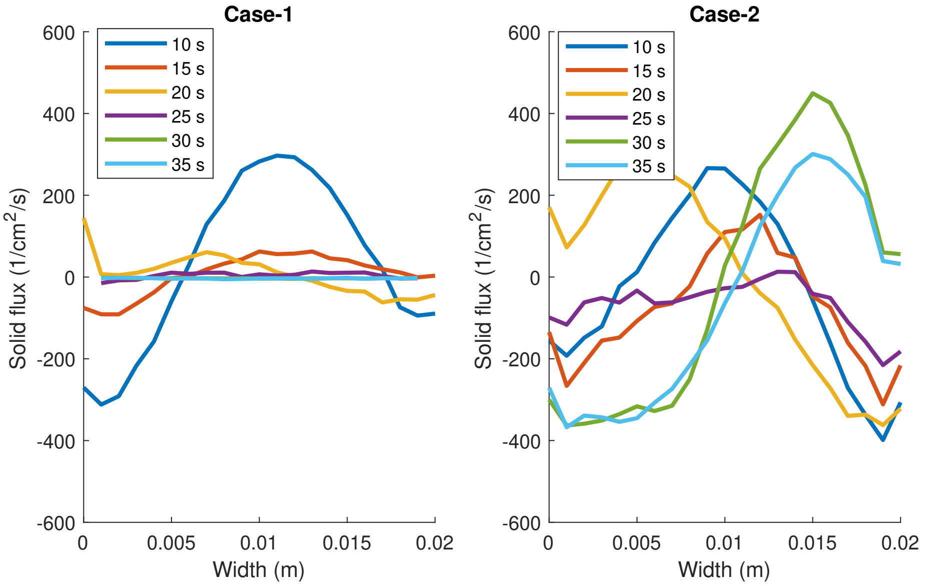

Fig. 5.10 Particle flux profiles at the height of 2 cm over time in Case-1 (left) and Case-2 (right). Solid flux in Case-1 reduces over time. In Case-2, solid fluxes remain high, and the insertion of the particles influences the profile.

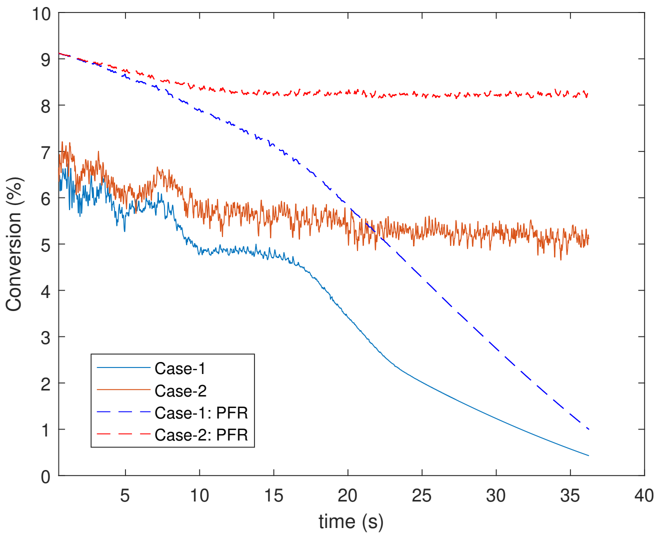

Fig. 5.11 Conversion of the gas phase in both cases compared with the performance of ideal PFRs.

5.3.5 Mass transfer limitations

The evaluation of external mass transfer limitation's impact and significance on the process performance, considering a pseudo-first-order reaction, can be achieved through the utilization of the second Damköhler number (Da_{II}) as depicted in Equation 5.21 [97]. In this equation, k_m represents the mass transfer coefficient, while the indices s and $bulk$ pertain to surface and local concentrations and temperature, respectively.

$$Da_{II} = \frac{R_p \hat{k}_1 C_{A,s}}{3 k_m C_{A,bulk}} \tag{5.21}$$

The linearization of the actual reaction kinetics (expressed by Equations (5.19) and (5.20)) into a pseudo-first-order reaction is accomplished by Equation (5.22). Consequently, the rate constant for the pseudo-first-order reaction is determined using Equation (5.23).

$$-r_A[\frac{mol_A}{g_{fresh\,cat}s}] \times 10^3[\frac{g_{fresh\,cat}}{kg_{fresh\,cat}}] \times \frac{m_0}{V_p}[\frac{kg_{fresh\,cat}}{m^3}] = \hat{k}_1\,[\frac{1}{s}]C_A[\frac{mol}{m^3}] \tag{5.22}$$

$$\hat{k}_1 = \frac{-r_A \times \frac{m_0}{V_p} \times 10^3}{C_A} \tag{5.23}$$

Figure 5.12-right illustrates the gradual decrease in Da_{II} over time, which is attributed to the reduction in $\hat{k}_1$ caused by catalyst deactivation and the declining density of active sites per unit volume of the particle. This reduction is inversely proportional to the third power of R_p. Based on the magnitude of Da_{II}, it can be inferred that the influence of external mass transfer limitations on the reaction rate and reactor performance is negligible for both cases.

Alternatively, the diffusional limitations of the process can be influenced by the growth of particle size and the formation of solid products. The assessment of this effect can be conducted through the examination of the Thiele modulus (ϕ^2). Equation (5.24), based on the assumed pseudo-first-order reaction rate, is employed for the calculation of ϕ^2 [97, 98].

$$\phi^2 = R_p^2 \frac{\hat{k}_1}{D^{\text{eff}}} \tag{5.24}$$

Figure 5.12-left demonstrates the declining trend of ϕ^2 over time, primarily attributable to the diminishing value of $\hat{k}_1$ and catalyst deactivation. The figure underscores the importance of diffusional effects, which cannot be disregarded. Notably, in Case-1, the significance of diffusional effects becomes negligible over time due to catalyst deactivation. This observation contradicts the trends discussed in Section 2.4.1 and may be attributed to the assumption of a constant D^{eff}, and it requires further research.

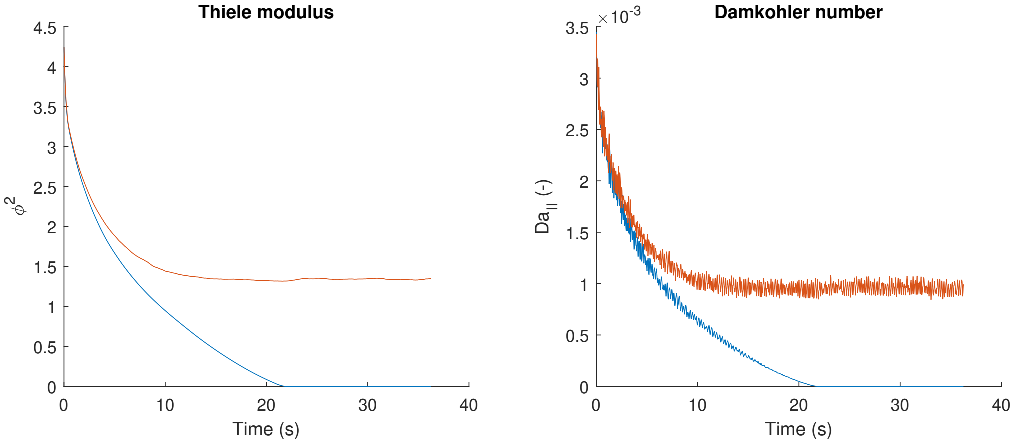

Fig. 5.12 Average Thiele modulus (left) and second Damkohler number (right) of the particles in both cases show that external mass transfer limitation has negligible effect, however, internal diffusion limitation is and remains important.

5.4 Conclusions

The CFD-DEM-MGM model was adapted for the TCD process with the kinetics derived from a former experimental study [29]. This model simulated two cases with a batch and a continuous solids flow. In Case-1, particles experience longer residence time and therefore grow larger and deactivate further than in Case-2. However, the rates of carbon production and gas conversion remain relatively high in Case-2, while in Case-1, a significant decay is observed due to catalyst deactivation.

Larger and heavier catalyst particles led to a transformation in the hydrodynamics of the FBR. Explicitly, the frequency of bubble formation dropped significantly in Case-1 during the later stages of the process. On the other hand, removing the large catalyst particles and introducing fresh catalyst particles led to breaking down the large bubbles and keeping the bubble formation frequency high. Furthermore, an enhanced horizontal solids mixing was observed in Case-2 due to stronger solids circulation.

Considering economic parameters and operational considerations, the design of the fluidized bed reactor and the solids flow rate can be optimized with this CFD-DEM-MGM model in the future.

The evaluation of the second Damkohler number and Thiele modulus shows that the external mass transfer limitations are negligible, the internal diffusion limitation, however, has a significant impact on the overall yield of the process, most importantly in the continuous scenario.

زندگی صحنه‌ی یکتای هنرمندی ماست
هر کسی نغمه‌ی خود خواند و از صحنه رود
صحنه پیوسته بجاست
خرم آن نغمه که مردم بسپارند به یاد

ژاله اصفهانی

Life’s stage, a canvas for our art to play,
Each arrives, sings, then gracefully bows away.
The platform endures, an eternal display,
A song finds immortality, in memories that forever sway.

Zhaleh Esfahani

6

Epilogue

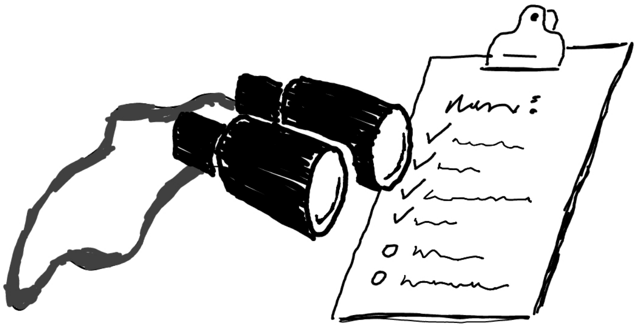

6.1 Conclusions

This thesis showcases ThermoCatalytic Decomposition of methane (TCD) in a fluidized bed reactor (FBR). Aiming to investigate the potential and challenges of TCD. The thesis focuses on evaluating the impact of effective parameters on the overall yield of the reactor.

6.1.1 Experimental study of TCD in an FBR

In **Chapter 2**, a commercial nickel on silica catalyst was employed in a specially designed FBR setup, leading to carbon yields exceeding $70\,\mathrm{g_C}/\mathrm{g_{cat}}$. The carbon product primarily consists of carbon nanofibers with a purity of at least 96%, characterized by TEM, TGA, and XPS tests, displaying fish-bone structures. The impact of various operating conditions was examined, revealing that lower temperatures promote higher carbon production despite a lower maximum reaction rate, as the catalyst deactivation is delayed. Lowering the methane concentration decreases the maximum reaction rate, lifetime, and carbon yield. However, the presence of hydrogen, while decreasing the maximum reaction rate, leads to a higher carbon yield due to prolonged catalyst lifetime. A kinetic model was developed to describe the maximum reaction rate and deactivation factor. This model describes the TCD reaction rate over the temperature range of $550-600\,^{\circ}\mathrm{C}$ with an average error in initial kinetic rate of 10% and deactivation factors up to 17%.

6.1.2 Numerical modeling of TCD

In **Chapter 3** the Multi-Grain Model (MGM) was developed to model the heat and mass transfer inside catalyst particles coupled with the decomposition reaction of methane. The reaction rate model and deactivation factor from Amin [6] were used in this chapter which were slower than the kinetic rate equation presented in Chapter 2. The effect of operating conditions and model parameters was investigated by sensitivity analyses and it was found that for the taken kinetic model in this chapter the heat and mass transfer rates do not limit the carbon production rate and consequently the reaction is the rate-limiting step of the process. However, it was also shown that if a catalyst is made with one thousand times higher ratio of kinetics rate to the mass and heat transfer rates (either by increasing the reaction rate or decreasing the mass and heat transfer rates), the heat and mass transfer limitations will affect the final carbon yield. It was found that, the presence of hydrogen causes a decrease in the reaction rate, however a higher carbon yield is achieved due to delayed deactivation of the catalyst. This fact is in agreement with experimental findings respected in the literature and Chapter 2. Moreover, increasing the operating temperature leads to a faster initial reaction rate and faster catalyst deactivation and hence an optimal, process dependent, temperature exists.

MGM was coupled with the comprehensive Computational Fluid Dynamics - Discrete Element Method model in **Chapter 4** to investigate the impact of particle growth on hydrodynamics, heat transfer, and mass transfer rates within a reactor. The accuracy and reliability of the CFD-DEM-MGM model were rigorously assessed by conducting a thorough verification process, involving a meticulous comparison of its simulation results with established analytical solutions, particularly focusing on the two-way heat and mass transfer coupling. To assess the model's capabilities and effectiveness in replicating dynamic behavior, a simulation was conducted on a fluidized bed reactor containing catalyst particles undergoing an arbitrary reaction. Initially, the reactor exhibited uniform particle size growth due to effective solid mixing. However, as the particle size increased, changes in fluidization behavior and a reduction in solids mixing rate were observed, eventually leading to complete defluidization of the bed. Consequently, a particle size gradient was observed along the reactor's height. For the chosen arbitrary reaction, external mass transfer limitations remained negligible, despite a slight increase in the Damköhler number. However, internal mass transfer limitations were found to be important. Nonetheless, the presented results demonstrate that the model effectively captures the coupling between hydrodynamics in a fluidized bed, particle growth, and the influences of mass and heat transfer.

In **Chapter 5**, the CFD-DEM-MGM model was specifically adapted and tailored for the ThermoCatalytic Decomposition (TCD) process, utilizing kinetics derived in Chapter 2. The model was employed to simulate two distinct cases: Case-1, representing a batch solid flow configuration, and Case-2, simulating a continuous solid flow scenario. In the continuous case, the limited residence time of the particles resulted in less growth and deactivation compared to the batch case. However, despite the catalyst deactivation observed in Case-1, Case-2 exhibited relatively high rates of carbon production and gas conversion. The presence of larger and heavier catalyst particles induced significant alterations in the hydrodynamics of the fluidized bed reactor (FBR). Notably, in Case-1, a considerable decrease in the frequency of bubble formation was observed during the later stages of the process. In contrast, removing large catalyst particles and introducing fresh catalyst particles in Case-2 facilitated the breakdown of larger bubbles, maintaining a consistently high frequency of bubble formation. Moreover, Case-2 exhibited enhanced horizontal solids mixing, attributed to the intensified local solid circulation within the reactor. Evaluation of the second Damkohler number and Thiele modulus revealed that while external mass transfer limitations remained negligible, internal diffusion limitations impacted the overall process yield, particularly in the continuous solid flow scenario.

6.2 Outlook

The ThermoCatalytic Decomposition (TCD) of methane in a fluidized bed reactor has gained significant attention as a promising approach for the simultaneous production of hydrogen and carbon nanomaterials. Looking ahead, several key aspects and areas of development can be identified to advance this field of research and optimize the TCD process in a fluidized bed reactors:

Further research is needed to comprehensively understand the deactivation mechanisms that limit catalyst performance over time. Investigating factors such as catalyst sintering and carbon deposition will be crucial to develop more accurate kinetic models and design strategies for lifetime improvement. Exploring the use of carbon materials, and other unconventional materials as catalysts has been studied. However, it is essential to enhance the sustainability of the TCD process further. Developing catalysts compatible with the desired applications of the carbon nanomaterials produced will contribute to a more environmentally friendly and economically viable TCD process.

Optimizing the design of fluidized bed reactors for TCD is crucial for achieving higher process efficiency and productivity. Computational modeling, such as the CFD-DEM-MGM model, coupled with experimental validation, can provide insights into the reactor hydrodynamics, solid mixing, and heat and mass transfer phenomena. This approach enables engineers to investigate different reactor concepts, such as continuous flow configurations, and determine the optimal operating conditions and solid flow rates. In this thesis, a high space velocity is chosen to enhance the catalyst mobility and prevent reactor wall damage caused by carbon deposition, but it limits the overall gas conversion. Overcoming this limitation on an industrial scale can be achieved through appropriate process design and probably partial recycling of the gas stream.

Conducting techno-economic and feasibility studies will be vital to evaluate the viability and scalability of TCD in fluidized bed reactors. Assessing the costs, energy requirements, and environmental impact of large-scale hydrogen and carbon nanomaterial production will provide valuable insights for decision-making and guide the development of economically sustainable TCD processes. This should be coupled with exploring opportunities for process integration and synergy can enhance the overall efficiency and sustainability of the TCD process. For instance, waste heat recovery, utilization of produced hydrogen, and integration with renewable energy sources can significantly improve energy efficiency and reduce the environmental footprint of the process.

The developed CFD-DEM-MGM model and the findings presented in this study hold promise for other processes such as polymerization, where both external and internal particle properties significantly impact process performance.

In general, the thermocatalytic decomposition of methane in fluidized bed reactors holds great potential for sustainable hydrogen and carbon nanomaterial production. Continued research efforts focusing on catalyst deactivation mechanisms, sustainable catalyst development, reactor design optimization, techno-economic assessments, and process integration will pave the way for the practical implementation of TCD in various industrial applications, contributing to a more sustainable and carbon-neutral future.

References

References

[1] Sánchez-Bastardo, N., Schlögl, R., Ruland, H. Methane Pyrolysis for CO2-Free H2 Production: A Green Process to Overcome Renewable Energies Unsteadiness. *Chemie Ingenieur Technik*, 92(10):1596–1609, 2020. ISSN 1522-2640. doi:10.1002/CITE.202000029.

[2] Abbas, H. F., Wan Daud, W. M. Hydrogen production by methane decomposition: A review. *International Journal of Hydrogen Energy*, 35(3):1160–1190, 2010. ISSN 0360-3199. doi:10.1016/J.IJHYDENE.2009.11.036.

[3] Younessi-Sinaki, M., Matida, E. A., Hamdullahpur, F. Kinetic model of homogeneous thermal decomposition of methane and ethane. *International Journal of Hydrogen Energy*, 34(9):3710–3716, 2009. ISSN 0360-3199. doi:10.1016/J.IJHYDENE.2009.03.014.

[4] Parfenov, V. E., Nikitchenko, N. V., Pimenov, A. A., Kuz'min, A. E., Kulikova, M. V., Chupichev, O. B., Maksimov, A. L. Methane Pyrolysis for Hydrogen Production: Specific Features of Using Molten Metals. *Russian Journal of Applied Chemistry*, 93(5):625–632, 2020. ISSN 16083296. doi:10.1134/S1070427220050018/TABLES/2.

[5] Parkinson, B., Matthews, J. W., McConnaughy, T. B., Upham, D. C., McFarland, E. W. Techno-Economic Analysis of Methane Pyrolysis in Molten Metals: Decarbonizing Natural Gas. *Chemical Engineering & Technology*, 40(6):1022–1030, 2017. ISSN 1521-4125. doi:10.1002/CEAT.201600414.

[6] Amin, A., Epling, W., Croiset, E. Reaction and deactivation rates of methane catalytic cracking over nickel. *Industrial and Engineering Chemistry Research*, 50(22):12460–12470, 2011. ISSN 08885885. doi:10.1021/ie201194z.

[7] Korányi, T. I., Németh, M., Beck, A., Horváth, A. Recent Advances in Methane Pyrolysis: Turquoise Hydrogen with Solid Carbon Production. *Energies 2022, Vol. 15, Page 6342*, 15(17):6342, 2022. ISSN 1996-1073. doi:10.3390/EN15176342.

[8] Catalan, L. J., Rezaei, E. Coupled hydrodynamic and kinetic model of liquid metal bubble reactor for hydrogen production by noncatalytic thermal decomposition of methane. *International Journal of Hydrogen Energy*, 45(4):2486–2503, 2020. ISSN 0360-3199. doi:10.1016/J.IJHYDENE.2019.11.143.

[9] Rahimi, N., Kang, D., Gelinas, J., Menon, A., Gordon, M. J., Metiu, H., McFarland, E. W. Solid carbon production and recovery from high temperature methane pyrolysis in bubble columns containing molten metals and molten salts. *Carbon*, 151:181–191, 2019. ISSN 0008-6223. doi:10.1016/J.CARBON.2019.05.041.

[10] Ahmed, S., Aitani, A., Rahman, F., Al-Dawood, A., Al-Muhaish, F. Review: Decomposition of hydrocarbons to hydrogen and carbon. *Applied Catalysis A: General*, 359(1-2):1–24, 2009. ISSN 0926860X. doi:10.1016/j.apcata.2009.02.038.

[11] Hadian, M., Buist, K. A., Bos, A. N. R., Kuipers, J. A. M. Single catalyst particle growth modeling in thermocatalytic decomposition of methane. *Chemical Engineering Journal*, 421:129759, 2021. ISSN 13858947. doi:10.1016/j.cej.2021.129759.

[12] Saraswat, S. K., Pant, K. K. Synthesis of hydrogen and carbon nanotubes over copper promoted Ni/SiO2 catalyst by thermocatalytic decomposition of methane. *Journal of Natural Gas Science and Engineering*, 13:52–59, 2013. ISSN 18755100. doi:10.1016/j.jngse.2013.04.001.

[13] Douven, S., Pirard, S. L., Heyen, G., Toye, D., Pirard, J. P. Kinetic study of double-walled carbon nanotube synthesis by catalytic chemical vapour deposition over an Fe-Mo/MgO catalyst using methane as the carbon source. *Chemical Engineering Journal*, 175(1):396–407, 2011. ISSN 13858947. doi:10.1016/j.cej.2011.08.066.

[14] Ashik, U. P., Wan Daud, W. M., Hayashi, J. I. A review on methane transformation to hydrogen and nanocarbon: Relevance of catalyst characteristics and experimental parameters on yield. *Renewable and Sustainable Energy Reviews*, 76(January):743–767, 2017. ISSN 18790690. doi:10.1016/j.rser.2017.03.088.

[15] Parmar, K. R., Pant, K. K., Roy, S. Blue hydrogen and carbon nanotube production via direct catalytic decomposition of methane in fluidized bed reactor: Capture and extraction of carbon in the form of CNTs. *Energy Conversion and Management*, 232:113893, 2021. ISSN 0196-8904. doi:10.1016/J.ENCONMAN.2021.113893.

[16] Srilatha, K., Bhagawan, D., Shiva Kumar, S., Himabindu, V. Sustainable fuel production by thermocatalytic decomposition of methane – A review. *South African Journal of Chemical Engineering*, pp. 156–167, 2017. ISSN 10269185. doi:10.1016/j.sajce.2017.10.002.

[17] Ashik, U. P., Wan Daud, W. M., Abbas, H. F. Production of greenhouse gas free hydrogen by thermocatalytic decomposition of methane - A review. *Renewable and Sustainable Energy Reviews*, 44:221–256, 2015. ISSN 18790690. doi:10.1016/j.rser.2014.12.025.

[18] Pham, C. Q., Siang, T. J., Kumar, P. S., Ahmad, Z., Xiao, L., Bahari, M. B., Cao, A. N. T., Rajamohan, N., Qazaq, A. S., Kumar, A., Show, P. L., Vo, D. V. N. Production of hydrogen and value-added carbon materials by catalytic methane decomposition: a

review. *Environmental Chemistry Letters 2022 20:4*, 20(4):2339–2359, 2022. ISSN 1610-3661. doi:10.1007/S10311-022-01449-2.

[19] Qian, J. X., Chen, T. W., Enakonda, L. R., Liu, D. B., Mignani, G., Basset, J. M., Zhou, L. Methane decomposition to produce COx-free hydrogen and nano-carbon over metal catalysts: A review. *International Journal of Hydrogen Energy*, 45(15):7981–8001, 2020. ISSN 0360-3199. doi:10.1016/J.IJHYDENE.2020.01.052.

[20] Toebes, M. L., Bitter, J. H., Jos Van Dillen, A., De Jong, K. P. Impact of the structure and reactivity of nickel particles on the catalytic growth of carbon nanofibers. *Catalysis Today*, 76(1):33–42, 2002. ISSN 09205861. doi:10.1016/S0920-5861(02)00209-2.

[21] Henao, W., Cazaña, F., Tarifa, P., Romeo, E., Latorre, N., Sebastian, V., Delgado, J. J., Monzón, A. Selective synthesis of carbon nanotubes by catalytic decomposition of methane using Co-Cu/cellulose derived carbon catalysts: A comprehensive kinetic study. *Chemical Engineering Journal*, 404:126103, 2021. ISSN 1385-8947. doi:10.1016/J.CEJ.2020.126103.

[22] Schoemaker, S. E., Welling, T. A., Wezendonk, D. F., Reesink, B. H., van Bavel, A. P., de Jongh, P. E. Carbon nanofiber growth from methane over carbon-supported NiCu catalysts: Two temperature regimes. *Catalysis Today*, p. 114110, 2023. ISSN 0920-5861. doi:10.1016/J.CATTOD.2023.114110.

[23] Yadav, M. D., Dasgupta, K., Patwardhan, A. W., Kaushal, A., Joshi, J. B. Kinetic study of single-walled carbon nanotube synthesis by thermocatalytic decomposition of methane using floating catalyst chemical vapour deposition. *Chemical Engineering Science*, 196(xxxx):91–103, 2019. ISSN 00092509. doi:10.1016/j.ces.2018.10.050.

[24] Yadav, M. D., Patwardhan, A. W., Joshi, J. B., Dasgupta, K. Kinetic study of multi-walled carbon nanotube synthesis by thermocatalytic decomposition of methane using floating catalyst chemical vapour deposition. *Chemical Engineering Journal*, 2018. ISSN 1385-8947. doi:10.1016/J.CEJ.2018.09.056.

[25] Saraswat, S. K., Sinha, B., Pant, K. K., Gupta, R. B. Kinetic Study and Modeling of Homogeneous Thermocatalytic Decomposition of Methane over a Ni-Cu-Zn/Al2O3 Catalyst for the Production of Hydrogen and Bamboo-Shaped Carbon Nanotubes. *Industrial and Engineering Chemistry Research*, 55(45):11672–11680, 2016. ISSN 15205045. doi:10.1021/acs.iecr.6b03145.

[26] Welling, T. A. J., Schoemaker, S. E., de Jong, K. P., de Jongh, P. E. Carbon Nanofiber Growth Rates on NiCu Catalysts: Quantitative Coupling of Macroscopic and Nanoscale In Situ Studies. *The Journal of Physical Chemistry C*, 2023. ISSN 1932-7447. doi:10.1021/acs.jpcc.3c02657.

[27] Borghei, M., Karimzadeh, R., Rashidi, A., Izadi, N. Kinetics of methane decomposition to COx-free hydrogen and carbon nanofiber over Ni-Cu/MgO catalyst. *International Journal of Hydrogen Energy*, 35(17):9479–9488, 2010. ISSN 03603199. doi:10.1016/j.ijhydene.2010.05.072.

[28] Latorre, N., Romeo, E., Villacampa, J. I., Cazaña, F., Royo, C., Monzón, A. Kinetics of carbon nanotubes growth on a Ni–Mg–Al catalyst by CCVD of methane: Influence of catalyst deactivation. *Catalysis Today*, 154(3-4):217–223, 2010. ISSN 0920-5861. doi:10.1016/J.CATTOD.2010.03.065.

[29] Hadian, M., Marrevee, D. P. F., Buist, K. A., Reesink, B. H., Bos, A. N. R., Bavel, A. P., Kuipers, J. A. M. Kinetic study of thermocatalytic decomposition of methane over nickel supported catalyst in a fluidized bed reactor. *Chemical Engineering Science*, 260:117938, 2022. ISSN 0009-2509. doi:10.1016/J.CES.2022.117938.

[30] Helveg, S., Lopez-Cartes, C., Sehested, J., Nature, P. H., 2004, u. Atomic-scale imaging of carbon nanofibre growth. *Nature*, 427(6973):426–429, 2004.

[31] Peng, Z., Somodi, F., Helveg, S., Kisielowski, C., catalysis, P. S. J. o., 2012, u. High-resolution in situ and ex situ TEM studies on graphene formation and growth on Pt nanoparticles. *Journal of catalysis*, 286:22–29, 2012.

[32] Muradov, N. Thermocatalytic CO2-Free Production of Hydrogen from Hydrocarbon Fuels. Technical report, Florida Solar Energy Center, Florida, 2003. doi:10.2172/828215.

[33] Qian, J. X., Enakonda, L. R., Wang, W. J., Gary, D., Del-Gallo, P., Basset, J. M., Liu, D. B., Zhou, L. Optimization of a fluidized bed reactor for methane decomposition over Fe/Al2O3 catalysts: Activity and regeneration studies. *International Journal of Hydrogen Energy*, 44(60):31700–31711, 2019. ISSN 0360-3199. doi:10.1016/J.IJHYDENE.2019.10.058.

[34] Torres, D., De Llobet, S., Pinilla, J. L., Lázaro, M. J., Suelves, I., Moliner, R. Hydrogen production by catalytic decomposition of methane using a Fe-based catalyst in a fluidized bed reactor. *Journal of Natural Gas Chemistry*, 21(4):367–373, 2012. ISSN 10039953. doi:10.1016/S1003-9953(11)60378-2.

[35] Pinilla, J. L., Moliner, R., Suelves, I., Lázaro, M. J., Echegoyen, Y., Palacios, J. M. Production of hydrogen and carbon nanofibers by thermal decomposition of methane using metal catalysts in a fluidized bed reactor. *International Journal of Hydrogen Energy*, 32(18):4821–4829, 2007. ISSN 0360-3199. doi:10.1016/J.IJHYDENE.2007.08.013.

[36] Pinilla, J. L., Suelves, I., Lázaro, M. J., Moliner, R., Palacios, J. M. Parametric study of the decomposition of methane using a NiCu/Al2O3 catalyst in a fluidized bed reactor. *International Journal of Hydrogen Energy*, 35(18):9801–9809, 2010. ISSN 0360-3199. doi:10.1016/J.IJHYDENE.2009.10.008.

[37] Weizhong, Q., Tang, L., Zhanwen, W., Fei, W., Zhifei, L., Guohua, L., Yongdan, L. Production of hydrogen and carbon nanotubes from methane decomposition in a two-stage fluidized bed reactor. *Applied Catalysis A: General*, 260(2):223–228, 2004. ISSN 0926-860X. doi:10.1016/J.APCATA.2003.10.018.

[38] Shah, N., Ma, S., Wang, Y., Huffman, G. P. Semi-continuous hydrogen production from catalytic methane decomposition using a fluidized-bed reactor. *International Journal of Hydrogen Energy*, 32(15):3315–3319, 2007. ISSN 0360-3199. doi:10.1016/J.IJHYDENE.2007.04.040.

[39] Dipu, A. L. Methane decomposition into COx-free hydrogen over a Ni-based catalyst: An overview. *International Journal of Energy Research*, 45(7):9858–9877, 2021. ISSN 1099-114X. doi:10.1002/ER.6541.

[40] Łamacz, A., Łabojko, G. CNT and H2 Production during CH4 Decomposition over Ni/CeZrO2. II. Catalyst Performance and Its Regeneration in a Fluidized Bed. *ChemEngineering 2019, Vol. 3, Page 25*, 3(1):25, 2019. ISSN 2305-7084. doi:10.3390/CHEMENGINEERING3010025.

[41] Muradov, N. Z., Veziroğlu, T. N. “Green” path from fossil-based to hydrogen economy: An overview of carbon-neutral technologies. *International Journal of Hydrogen Energy*, 33(23):6804–6839, 2008. ISSN 0360-3199. doi:https://doi.org/10.1016/j.ijhydene.2008.08.054.

[42] Muradov, N., Chen, Z., Smith, F. Fossil hydrogen with reduced CO2 emission: Modeling thermocatalytic decomposition of methane in a fluidized bed of carbon particles. *International Journal of Hydrogen Energy*, 30(10):1149–1158, 2005. ISSN 0360-3199. doi:10.1016/J.IJHYDENE.2005.04.005.

[43] Nezam, I., Zhou, W., Gusmão, G. S., Realff, M. J., Wang, Y., Medford, A. J., Jones, C. W. Direct aromatization of CO2 via combined CO2 hydrogenation and zeolite-based acid catalysis. *Journal of CO2 Utilization*, 45:101405, 2021. ISSN 2212-9820. doi:10.1016/J.JCOU.2020.101405.

[44] Ra, E. C., Kim, K. Y., Kim, E. H., Lee, H., An, K., Lee, J. S. Recycling Carbon Dioxide through Catalytic Hydrogenation: Recent Key Developments and Perspectives. *ACS Catalysis*, 10(19):11318–11345, 2020. ISSN 21555435. doi:10.1021/ACSCATAL.0C02930.

[45] Pudukudy, M., Kadier, A., Yaakob, Z., Takriff, M. S. Non-oxidative thermocatalytic decomposition of methane into COx free hydrogen and nanocarbon over unsupported porous NiO and Fe2O3 catalysts. *International Journal of Hydrogen Energy*, 41(41):18509–18521, 2016. ISSN 03603199. doi:10.1016/j.ijhydene.2016.08.160.

[46] Wang, G., Jin, Y., Liu, G., Li, Y. Production of hydrogen and nanocarbon from catalytic decomposition of methane over a Ni-Fe/Al2O3 catalyst. *Energy and Fuels*, 27(8):4448–4456, 2000. ISSN 08870624. doi:10.1021/ef3019707.

[47] Reshetenko, T. V., Avdeeva, L. B., Ismagilov, Z. R., Chuvilin, A. L., Ushakov, V. A. Carbon capacious Ni-Cu-Al2O3 catalysts for high-temperature methane decomposition. *Applied Catalysis A: General*, 247(1):51–63, 2003. ISSN 0926860X. doi:10.1016/S0926-860X(03)00080-2.

[48] Avdeeva, L., Kochubey, D., Novgorodov, B., Goncharova, O., Shaikhutdinov, S., Zaikovskii, V., Plyasova, L. Coprecipitated Ni-alumina and Ni-Cu-alumina catalysts of methane decomposition and carbon deposition. II. Evolution of the catalysts in reaction. *Applied Catalysis A: General*, 141(1-2):117–129, 1996. ISSN 0926860X. doi:10.1016/0926-860x(96)00026-9.

[49] Li, Y., Chen, J., Qin, Y., Chang, L. Simultaneous Production of Hydrogen and Nanocarbon from Decomposition of Methane on a Nickel-Based Catalyst. *Energy and Fuels*, 14(6):1188–1194, 2000. ISSN 08870624. doi:10.1021/ef0000781.

[50] Guevara, J. C., Wang, J. A., Chen, L. F., Valenzuela, M. A., Salas, P., García-Ruiz, A., Toledo, J. A., Cortes-Jácome, M. A., Angeles-Chavez, C., Novaro, O. Ni/Ce-MCM-41 mesostructured catalysts for simultaneous production of hydrogen and nanocarbon via methane decomposition. *International Journal of Hydrogen Energy*, 35(8):3509–3521, 2010. ISSN 03603199. doi:10.1016/j.ijhydene.2010.01.068.

[51] Suelves, I., Pinilla, J. L., Lázaro, M. J., Moliner, R., Palacios, J. M. Effects of reaction conditions on hydrogen production and carbon nanofiber properties generated by methane decomposition in a fixed bed reactor using a NiCuAl catalyst. *Journal of Power Sources*, 192(1):35–42, 2009. ISSN 03787753. doi:10.1016/j.jpowsour.2008.11.096.

[52] Kuvshinov, G. G., Mogilnykh, Y. I., Kuvshinov, D. G. Kinetics of carbon formation from CH4–H2 mixtures over a nickel containing catalyst. *Catalysis Today*, 42(3):357–360, 1998. ISSN 0920-5861. doi:10.1016/S0920-5861(98)00115-1.

[53] Zavarukhin, S. G., Kuvshinov, G. G. The kinetic model of formation of nanofibrous carbon from CH 4-H2 mixture over a high-loaded nickel catalyst with consideration for the catalyst deactivation. *Applied Catalysis A: General*, 272(1-2):219–227, 2004. ISSN 0926860X. doi:10.1016/j.apcata.2004.05.044.

[54] Kunii, D., Levenspiel, O. *Fluidization Engineering*. Elsevier, second edi edition, 2013. ISBN 0409902330.

[55] Luxembourg, D., Flamant, G., Laplaze, D. Solar synthesis of single-walled carbon nanotubes at medium scale. *Carbon*, 43(11):2302–2310, 2005. ISSN 0008-6223. doi:10.1016/J.CARBON.2005.04.010.

[56] Hu, H., Zhao, B., Itkis, M. E., Haddon, R. C. Nitric Acid Purification of Single-Walled Carbon Nanotubes. *ACS Publications*, 107(50):13838–13842, 2003. doi:10.1021/jp035719i.

[57] Li, J., Zhang, Y. A simple purification for single-walled carbon nanotubes. *Physica E: Low-Dimensional Systems and Nanostructures*, 28(3):309–312, 2005. ISSN 13869477. doi:10.1016/j.physe.2005.03.022.

[58] Lehman, J. H., Terrones, M., Mansfield, E., Hurst, K. E., Meunier, V. Evaluating the characteristics of multiwall carbon nanotubes. *Carbon*, 49(8):2581–2602, 2011. ISSN 00086223. doi:10.1016/j.carbon.2011.03.028.

[59] Dresselhaus, M. S. Nanotechnology: New tricks with nanotubes. *Nature*, 391(6662):19–20, 1998. ISSN 00280836. doi:10.1038/34036.

[60] De Jong, K. P., Geus, J. W. Carbon Nanofibers: Catalytic Synthesis and Applications. *Catalysis Reviews - Science and Engineering*, 42(4):481–510, 2000. ISSN 01614940. doi:10.1081/CR-100101954.

[61] Meng, L., Sun, Q., Wang, J., Ding, F. Molecular dynamics simulation of chemical vapor deposition graphene growth on Ni (111) surface. *Journal of Physical Chemistry C*, 116(10):6097–6102, 2012. ISSN 19327447. doi:10.1021/jp212149c.

[62] Shibuta, Y., Elliott, J. A. A molecular dynamics study of the graphitization ability of transition metals for catalysis of carbon nanotube growth via chemical vapor deposition. *Chemical Physics Letters*, 472(4-6):200–206, 2009. ISSN 00092614. doi:10.1016/j.cplett.2009.03.010.

[63] Yadav, M. D., Dasgupta, K., Patwardhan, A. W., Kaushal, A., Joshi, J. B. Kinetic study of single-walled carbon nanotube synthesis by thermocatalytic decomposition of methane using floating catalyst chemical vapour deposition. *Chemical Engineering Science*, 196:91–103, 2019. ISSN 00092509. doi:10.1016/j.ces.2018.10.050.

[64] Ashik, U. P., Wan Daud, W. M., Abbas, H. F. Methane decomposition kinetics and reaction rate over Ni/SiO2 nanocatalyst produced through co-precipitation cum modified StÖber method. *International Journal of Hydrogen Energy*, 42(2):938–952, 2017. ISSN 03603199. doi:10.1016/j.ijhydene.2016.09.025.

[65] Demicheli, M. C., Ponzi, E. N., Ferretti, O. A., Yeramian, A. A. Kinetics of carbon formation from CH4-H2 mixtures on nickel-alumina catalyst. *The Chemical Engineering Journal*, 46(3):129–136, 1991. ISSN 03009467. doi:10.1016/0300-9467(91)87004-T.

[66] Snoeck, J. W., Froment, G. F., Fowles, M. Kinetic study of the carbon filament formation by methane cracking on a nickel catalyst. *Journal of Catalysis*, 169(1):250–262, 1997. ISSN 00219517. doi:10.1006/jcat.1997.1635.

[67] Sharif Zein, S. H., Mohamed, A. R., Talpa Sai, P. S. Kinetic Studies on Catalytic Decomposition of Methane to Hydrogen and Carbon over Ni/TiO 2 Catalyst . *Industrial & Engineering Chemistry Research*, 43(16):4864–4870, 2004. ISSN 0888-5885. doi:10.1021/ie034208f.

[68] Alizadeh, A., McKenna, T. F. Particle Growth during the Polymerization of Olefins on Supported Catalysts. Part 2: Current Experimental Understanding and Modeling Progresses on Particle Fragmentation, Growth, and Morphology Development. *Macromolecular Reaction Engineering*, 12(1), 2018. ISSN 18628338. doi:10.1002/mren.201700027.

[69] McKenna, T. F., Soares, J. B. Single particle modelling for olefin polymerization on supported catalysts: A review and proposals for future developments. *Chemical Engineering Science*, 56(13):3931–3949, 2001. ISSN 00092509. doi:10.1016/S0009-2509(01)00069-0.

[70] Chiovetta, M. G., Estenoz, D. A. Behavior of Active Sites in a Changing, Supported Metallocene Catalyst Particle: Modeling Monomer Transport and Kinetics. *Macromolecular Materials and Engineering*, 289(11):1012–1026, 2004. ISSN 1438-7492. doi:10.1002/mame.200400069.

[71] Ferrero, M. A., Chiovetta, M. G. Catalyst fragmentation during propylene polymerization. III: Bulk polymerization process simulation. *Polymer Engineering and Science*, 31(12):886–903, 1991. ISSN 0032-3888. doi:10.1002/pen.760311208.

[72] Ferrero, M. A., Chiovetta, M. G. Catalyst fragmentation during propylene polymerization: Part I. The effects of grain size and structure. *Polymer Engineering and Science*, 27(19):1436–1447, 1987. ISSN 0032-3888. doi:10.1002/pen.760271903.

[73] Ferrero, M. A., Chiovetta, M. G. Catalyst fragmentation during propylene polymerization: Part II. Microparticle diffusion and reaction effects. *Polymer Engineering & Science*, 27(19):1448–1460, 1987. ISSN 15482634. doi:10.1002/pen.760271904.

[74] Vannice, M. A. *Kinetics of catalytic reactions*. Springer US, New York, 2005. ISBN 0387246495. doi:10.1007/b136380.

[75] De Jong, J. F., Dang, T. Y. N., Van Sint Annaland, M., Kuipers, J. A. M. Comparison of a Discrete Particle Model and a Two-Fluid Model to experiments of a fluidized bed with flat membranes. *Powder Technology*, 230:93–105, 2012. ISSN 0032-5910. doi:10.1016/J.POWTEC.2012.06.059.

[76] Golshan, S., Sotudeh-Gharebagh, R., Zarghami, R., Mostoufi, N., Blais, B., Kuipers, J. A. M. Review and implementation of CFD-DEM applied to chemical process systems, 2020. doi:10.1016/j.ces.2020.115646.

[77] Mu, L., Buist, K. A., Kuipers, J. A. M., Deen, N. G. Scaling method of CFD-DEM simulations for gas-solid flows in risers. *Chemical Engineering Science: X*, 6:100054, 2020. ISSN 2590-1400. doi:10.1016/J.CESX.2019.100054.

[78] Norouzi, H. R., Zarghami, R., Sotudeh-Gharebagh, R., Mostoufi, N. *Coupled CFD-DEM Modeling: Formulation, Implementation and Application to Multiphase Flows*. John Wiley & Sons, 2016. ISBN 9781119005315. doi:10.1002/9781119005315.

[79] Finotello, G., Padding, J. T., Buist, K. A., Schijve, A., Jongsma, A., Innings, F., Kuipers, J. A. M. Numerical investigation of droplet-droplet collisions in a water and milk spray with coupled heat and mass transfer. *Drying Technology*, 38(12):1597–1619, 2019. ISSN 15322300. doi:10.1080/07373937.2019.1651732.

[80] Zhuang, Y. Q., Chen, X. M., Luo, Z. H., Xiao, J. CFD–DEM modeling of gas–solid flow and catalytic MTO reaction in a fluidized bed reactor. *Computers & Chemical Engineering*, 60:1–16, 2014. ISSN 0098-1354. doi:10.1016/J.COMPCHEMENG.2013.08.007.

[81] Lu, L., Gao, X., Shahnam, M., Rogers, W. A. Bridging particle and reactor scales in the simulation of biomass fast pyrolysis by coupling particle resolved simulation and coarse grained CFD-DEM. *Chemical Engineering Science*, 216:115471, 2020. ISSN 0009-2509. doi:10.1016/J.CES.2020.115471.

[82] Wang, J., Ku, X., Yang, S. Simulation of Biomass Pyrolysis in a Rotary Drum by Coupling CFD-DEM with a One-Dimensional Thermally Thick Model. *Energy & Fuels*, 36(7):3665–3679, 2022. ISSN 0887-0624. doi:10.1021/ACS.ENERGYFUELS.2C00050.

[83] Oyedeji, O. A., Brennan Pecha, M., Finney, C. E., Peterson, C. A., Smith, R. G., Mills, Z. G., Gao, X., Shahnam, M., Rogers, W. A., Ciesielski, P. N., Brown, R. C., Parks, J. E. CFD–DEM modeling of autothermal pyrolysis of corn stover with a coupled particle- and reactor-scale framework. *Chemical Engineering Journal*, 446:136920, 2022. ISSN 1385-8947. doi:10.1016/J.CEJ.2022.136920.

[84] Pecha, M. B., Thornburg, N. E., Peterson, C. A., Crowley, M. F., Gao, X., Lu, L., Wiggins, G., Brown, R. C., Ciesielski, P. N. Impacts of Anisotropic Porosity on Heat Transfer and Off-Gassing during Biomass Pyrolysis. *Energy and Fuels*, 35(24):20131–20141, 2021. ISSN 15205029. doi:10.1021/ACS.ENERGYFUELS.1C02679/ASSET/IMAGES/LARGE/EF1C02679{_}0008.JPEG.

[85] Lu, L., Gao, X., Shahnam, M., Rogers, W. A. Simulations of biomass pyrolysis using glued-sphere CFD-DEM with 3-D intra-particle models. *Chemical Engineering Journal*, 419:129564, 2021. ISSN 1385-8947. doi:10.1016/J.CEJ.2021.129564.

[86] Li, Z., Janssen, T. C. E., Buist, K. A., Deen, N. G., van Sint Annaland, M., Kuipers, J. A. M. Experimental and simulation study of heat transfer in fluidized beds with heat production. *Chemical Engineering Journal*, 317:242–257, 2017. ISSN 1385-8947. doi:10.1016/J.CEJ.2017.02.055.

[87] Sarkar, S., van der Hoef, M. A., Kuipers, J. A. M. Fluid-particle interaction from lattice Boltzmann simulations for flow through polydisperse random arrays of spheres. *Chemical Engineering Science*, 64(11):2683–2691, 2009. ISSN 00092509. doi:10.1016/j.ces.2009.02.045.

[88] Beetstra, R., Van Der Hoef, M. A., Kuipers, J. A. M. Drag force of intermediate reynolds number flow past mono- And bidisperse arrays of spheres. *AIChE Journal*, 53(2):489–501, 2007. ISSN 15475905. doi:10.1002/aic.11065.

[89] Patil, A. V., Peters, E. A. J. F., Kuipers, J. A. M. Comparison of CFD-DEM heat transfer simulations with infrared/visual measurements. *Chemical Engineering Journal*, 277:388–401, 2015. ISSN 13858947. doi:10.1016/j.cej.2015.04.131.

[90] Hoomans, B. P. B., Kuipers, J. A. M., Briels, W. J., Van Swaaij, W. P. M. Discrete particle simulation of bubble and slug formation in a two-dimensional gas-fluidised bed: A hard-sphere approach. *Chemical Engineering Science*, 51(1):99–118, 1996. ISSN 00092509. doi:10.1016/0009-2509(95)00271-5.

[91] Cundall, P. A., Strack, O. D. A discrete numerical model for granular assemblies. *Geotechnique*, 29(1):47–65, 1979. ISSN 17517656. doi:10.1680/GEOT.1979.29.1.47.

[92] Buist, K. A., Seelen, L. J. H., Deen, N. G., Padding, J. T., Kuipers, J. A. M. On an efficient hybrid soft and hard sphere collision integration scheme for DEM. *Chemical Engineering Science*, 153:363–373, 2016. ISSN 0009-2509. doi:10.1016/J.CES.2016.07.030.

[93] Kloss, C., Christoph, G., Hager, A., Amberger, S., Pirker, S. Models , algorithms and validation for opensource DEM and CFD-DEM. 12:140–152, 2012.

[94] Anzelius, A. Über erwärmung vermittels durchströmender medien. *ZAMM-Journal of Applied Mathematics and Mechanics/Zeitschrift für Angewandte Mathematik und Mechanik*, 6(4):291–294, 1926. ISSN 0044-2267.

[95] Bateman, H. Partial differential equations of mathematical physics. *Partial Differential Equations of Mathematical Physics*, 1932.

[96] Hougen, O. A., Watson, K. M., Ragatz, R. A. *Chemical process principles. 3. Kinetics and catalysis*. Wiley, 1947.

[97] Bird, R. B., Stewart, W. E., Lightfoot, E. N. *Transport phenomena*. John Wiley & Sons, New York, 2nd edition, 2001.

[98] Delparish, A., W. N. de Leeuw den Bouter, A., Yercan, A., van der Schaaf, J., Fernanda Neira d'Angelo, M. Bringing the promises of microreactors and gold catalysis to lignocellulosic biomass valorization: A study on oxidative transformation of furfural. *Chemical Engineering Journal*, 452:138903, 2023. ISSN 1385-8947. doi:10.1016/J.CEJ.2022.138903.

[99] Amin, A. M., Croiset, E., Constantinou, C., Epling, W. Methane cracking using Ni supported on porous and non-porous alumina catalysts. *International Journal of Hydrogen Energy*, 37(11):9038–9048, 2012. ISSN 03603199. doi:10.1016/j.ijhydene.2012.02.001.

[100] Delparish, A., Kanungo, S., Van Der Schaaf, J., Neira D'Angelo, M. F. Towards coupling direct activation of methane with in situ generation of H2O2. *Catalysis Science & Technology*, 9(18):5142–5149, 2019. ISSN 20444761. doi:10.1039/C9CY01304K.

[101] Delparish, A., Avci, A. K. Intensified catalytic reactors for Fischer-Tropsch synthesis and for reforming of renewable fuels to hydrogen and synthesis gas. *Fuel Processing Technology*, 151:72–100, 2016. ISSN 0378-3820. doi:10.1016/J.FUPROC.2016.05.021.

[102] Ammendola, P., Chirone, R., Ruoppolo, G., Russo, G., Solimene, R. Some issues in modelling methane catalytic decomposition in fluidized bed reactors. *International Journal of Hydrogen Energy*, 33(11):2679–2694, 2008. ISSN 0360-3199. doi:10.1016/J.IJHYDENE.2008.03.033.

[103] de Munck, M. J., Dullemond, M., Peters, E. A., Kuipers, J. A. Experimental gas-fluidized bed drying study on the segregation and mixing dynamics for binary and ternary solids. *Chemical Engineering Journal*, 465:142756, 2023. ISSN 1385-8947. doi:10.1016/J.CEJ.2023.142756.

[104] Buist, K. A., Baltussen, M. W., Peters, E. A. J. F. F., Kuipers, J. A. M. H. Multiscale Modeling of Multiphase Flows. *Multiphase Flows for Process Industries*, pp. 95–202, 2022. doi:10.1002/9783527812066.CH3.

[105] Patil, P., Shrivastava, S. K. Fast dissolving oral films: an innovative drug delivery system. *Structure*, 20(70):50–500, 2014.

[106] de Munck, M. J., van Gelder, J. B., Peters, E. A., Kuipers, J. A. A detailed gas-solid fluidized bed comparison study on CFD-DEM coarse-graining techniques. *Chemical Engineering Science*, 269:118441, 2023. ISSN 0009-2509. doi:10.1016/J.CES.2022.118441.

[107] Stołecki, K., Michalska, K., Narowski, R., Gołębiowski, A. Effectiveness diffusion coefficient in nickel catalyst grain determined by measurements of catalytic reaction rate. *Annales UMCS, Chemistry*, 65(-1):3–6, 2011. ISSN 0137-6853. doi:10.2478/v10063-010-0010-6.

Appendices

A

Weisz-Prater Criterion

According to Weisz-Prater criterion, C_{WP}, using the given kinetic parameters (Taken from Amin et al. [6]) the mass transfer limitation can be neglected compared with reaction kinetics limitations, if equation A.1 holds [74].

$$C_{WP} = \frac{Rate.(dp/2)^2}{D_{eff}.M_b} \leq 3\beta \tag{A.1}$$

$$\eta = 1 - \frac{n\beta}{4} \tag{A.2}$$

where $Rate$ is the observed rate, D_{eff} is effective diffusivity, M_b is the concentration of the reactant outside the porous particle, β maximum decrease in concentration gradient in pores, η is effectiveness factor, and n is the order of the reaction. The reaction is considered first order (following equation 2.3) and the observed rate of reaction is obtained from experimental results. Using the other parameters as is presented in Table A.1, it is found:

$$C_{WP} = 0.42 \leq 0.6$$

This confirms that the diffusional mass transfer limitation can just be neglected. However, with larger particles, it can become important as it has effect on the carbon yield and lifetime of the catalyst, see section 2.4.1.

Table A.1 Parameters used to calculate C_{WP}

Parameter	Value
Rate	141.179 mol/m^3/s
D_{eff} [107]	1.36×10^{-6} m^2/s
M_b	100 vol.%CH_4=14.37 mol_{CH_4}/m^3
d_p	500 μm
T	575 °C
η	0.95
n	1

Publications and Contributions

Journal publications

- Hadian, M., Buist, K. A., Kuipers, J. A. M. (2023), An overview of production of hydrogen and carbon nanomaterials via thermocatalytic decomposition of methane. Current Opinion in Chemical Engineering, 2023.
- Hadian, M., Marrevee, D. P. F., Buist, K. A., Reesink, B. H., Bos, A. N. R., Bavel, A. P., Kuipers, J. A. M. (2022), Kinetic study of thermocatalytic decomposition of methane over nickel-supported catalyst in a fluidized bed reactor. Chemical Engineering Science, 260, 117938.
- Hadian, M., Buist, K. A., Bos, A. N. R., Kuipers, J. A. M. (2021). Single catalyst particle growth modeling in thermocatalytic decomposition of methane. Chemical Engineering Journal, 421, 129759.
- Hadian M., de Munck M. J. A., Buist K. A., Bos A. N. R., Kuipers J. A. M., (2023), Modeling of a catalytic fluidized bed reactor via coupled CFD-DEM with MGM: from intra-particle scale to reactor scale. *Submitted to Chemical Engineering Science*.
- Hadian M., Ramírez J. G., de Munck M. J. A., Buist K. A., Bos A. N. R., Kuipers J. A. M., (2023), Comparative analysis of a batch and continuous fluidized bed reactors for thermocatalytic decomposition of methane: a CFD-DEM-MGM approach. *Submitted to Chemical Engineering Journal*.

Conference oral presentations

- Hadian, M., Marrevee, D. P. F., Buist, K. A., Reesink, B. H., Bos, A. N. R., Bavel, A. P., Kuipers, J. A. M., Kinetic study of CO2-free production of carbon nanomaterials and hydrogen from methane in a fluidized bed reactor, 17th Netherlands Process Technology Symposium (NPS17), Delft, Netherlands, 2022.

- Hadian, M., Marrevee, D. P. F., Buist, K. A., Reesink, B. H., Bos, A. N. R., Bavel, A. P., Kuipers, J. A. M., Thermocatalytic decomposition of methane in a fluidized bed – Experimental study of fluidization of growing catalyst particles, 11th International Conference on Multiphase Flow (ICMF 2023), Kobe, Japan, 2023.

- Hadian, M., de Munck M. J. A., Buist, K. A., Kuipers, J. A. M., Modeling a fluidized bed of growing catalyst particles: coupling CFD-DEM with MGM, 11th International Conference on Multiphase Flow (ICMF 2023), Kobe, Japan, 2023.

- Hadian, M., Buist, K. A., Kuipers, J. A. M., Thermocatalytic Decomposition of Methane in a Fluidized Bed Reactor: Proof of Concept, AIChE Fluidization XVII, Edinburgh, Scotland, UK, 2023.

Acknowledgements

My Journey would not have been possible without the help of many, and has created very fond memories. It is not possible to put them all into words, but I try my best.

Dear prof. Kuipers, dear Hans, I remember that I had only one interview with you, but it was for another project. Shortly after, you invited me to your office and offered me instead, this interesting and challenging project, which I loved. Thank you for trusting me and giving me this opportunity. You inspired me with your knowledge, experience, management, and personality. I was fortunate to have dedicated regular project meetings alongside our wonderful CFD-DEM cluster meeting. I was always impressed by your eagle-eye view on the different disciplines of science and engineering from the past, to the very moment and even to the future. Your feedback and comments were always a valuable source of insight, ideas and inspiration. I want to express my deep gratitude. I am so honored that I have worked with you.

Dear Kay, I enjoyed working with you as my co-promoter and daily supervisor. With you, everything went easy and smooth for me. I could express myself and my thoughts freely with you, and I always got positive and constructive feedback. You are a great scientist and chemical engineer in different disciplines, which was a very solid support for me. In addition, and more importantly, you are a great person who cares about others. I will not forget all your efforts to oppose any possible point of discrimination, all the nice talks we had, and your kind support when I needed it. I cannot thank you enough for all this.

I was so glad to have even more support from experts coming from industrial partners of the project, Shell and BASF. Dear René, Bennie and Sander, we met every three weeks online and occasionally in Utrecht and I appreciate all the valuable insights I gained from our interactions. René, you always challenged me from a point of view that I had not thought

about it, spotting the possible wrong turns and trying to redirect me. Bennie, with the knowledge and enthusiasm you have about catalysts, it was always joyful to have longer discussions with you about them. You are so kind that once, you even drove to Eindhoven to bring a catalyst sample for me! Sander, your comprehensive view of different projects and connecting related elements to each other as possible points of collaboration was amazing to observe.

I would also like to thank the committee members prof. van Geem, prof. de Jongh, prof. Smeulders, prof. van Sint Annaland, prof. Gallucci and prof. Rebrov for their time and effort spent on reviewing this thesis and attending the defense. It is greatly appreciated. Martin and Fausto, you were also my previous supervisors and I learned a lot from you. You helped me to settle down in the Netherlands. I remember that at the very beginning, you asked me to join the outing organizer team to integrate faster with my new colleagues.

I would like to thank my bachelor and master students, whom I enjoyed supervising and working with them. Stan, you are a hard worker and did a great job. Danny, you were very enthusiastic and I really enjoyed all our chats about the project and video games. Jacco, despite the many uncertainties in the project, you managed to do your challenging project. Gertjan, it was very tough to, during the Covid's strict measures, times dive deep into two numerical models and try to couple them, but you did it. I wish you all the best for your future careers! Daan you introduced iron catalysts to the reactor. Charles, your bimetallic catalysts were so good that I can literally say that the experiments were on fire! An unforgettable memory.

I would also like to thank Frank and Maike. While you were not directly supervising my project, I took advantage of your valuable inputs and help during our constructive CFD-DEM cluster meetings and also C++ meetings, for which I am grateful. Larry, Herbert, Joop, Joost, Thijs, and Jorris thank you for your valuable technical support and for being available whenever I needed you during my project. It was not possible to do this project without your help. Ada and Carola, with your kindness and carefulness, you were beyond a secretary and took care of many things. I appreciate all your help. Judith, you also were a great help with your extensive experience and I appreciate it.

I would like to acknowledge ARC-CBBC and industrial partners of the "Small Molecule Activation" project, Shell and BASF, for allowing me to perform this research and for their continual support. In the "Small Molecule Activation" project, we had several meetings and also collaborations: Prof. Weckhuysen, prof. van Blaaderen, prof. Hensen, prof. de Jong, prof. de Jongh, dr. Vollmer, dr. Kosinov, dr. Berben, dr. Munnik, dr. Zuidema, dr. Unsal, and dr. Terörde thank you for the many interesting meetings we had, your advice and questions have ensured the relevance of this flagship project and its results. The ARC-CBBC office and

its nice people were one of the remarkable aspects of the last four years. I must begin with Hannah. I admit that I still do not know your exact role in ARC-CBBC because you take so many responsibilities. You facilitate the environment and opportunities for the researchers to progress, and I appreciate all your efforts. I want to also thank the other administration staff of ARC-CBBC, including Julien, Anna-Eva, Juliet, Jeroen, Masja, Marijke, Ànita and Anita!

I also had nice colleagues on this project. Hao, Harith, Haissam and Sebastian, your presentations were interesting in project meetings. I remember clearly the talks that I had with Sebastian during meetings, summer school and the podcast and I cannot believe that we do not have him with us anymore! Suzan and Tom, I really enjoyed all the collaborations that we had and I gained new insights and learned a lot from you about catalysis. Thank you very much. I would like to thank Mijram, and Rim as well for their help and friendly chats.

Martijn, with your great knowledge of multi-phase phenomena, remarkable programming skills, and helping mentality, you were a solid support for me in this project and I am very grateful to you. Juangi, your contribution was significant in my project, but your help was not limited to the project, because you are a great person, mate! Thanks to both of you our CFD-DEM meetings and also the Edinburgh Journey were unforgettable.

Amirhossein, you are a very honest person and a good friend. Ali, the more I knew you, the more I liked you. With the two of you we shared lots of fun moments, from football on weekends (plus chai and sweets), to Japan, which was very Shinkansen! Let's keep meeting and playing football. Arvin, you have a superpower, which is being able to be funny. I won't forget all the laughs that we had together. I was lucky enough to share the office with amazing office mates. Cristina, Vivek, Francesco, Stefan and Michella and Lijing, you were always there to help or just to chat and take a break. You really made office work easier and more enjoyable. Cristina and Vivek we laughed, got sad, gossiped and enjoyed our time together. It felt like much more than working next to each other, we found a nice connection. David, I enjoyed the many times we came to your place and had fun. Merve, you are the kindest person possible. Noah, Claire, Danny, Sherwin, Aniket and Samaneh, Leon, Kun, Marzieh, Jiangtao, and Alperen thank you so much for your support and all the fun we shared during the coffee and lunch breaks. I must also mention my gratitude to my former colleagues, Tim, Evan, Maxim, Dario, Satish, Hossein, Jiangtao, Ramon, Solomon, Alessandro, Milan, Aitor, Alba, Niek, Giulia, Jose, Alexei, Maria, Nerea, Alvaro, and Haryo. Your presence was heartwarming in the early years that I was living abroad. With some of you, we are still in touch and we will keep it like that. Ramon, I like any time that we talk about football or work. Solomon, I will still meet you regularly to play football and more. Thank you Jadi who taught me Git, Tmux, and even some non-technical personal developments. If I forgot any name on this list, please forgive me and know I had no whatsoever intent to do so.

Arash (Helmi), you were and are like a supportive brother and a true friend. Whenever I need professional advice, you are my first and most reliable reference, and you help me generously and without any hesitation. But you are much more than that and you always unfold a new corner of the meaning of life. I am very lucky to have you as my friend. Arash (Amooyi), I met you on my first day in the Netherlands, and since then you have been such a good and energetic friend who could level up my mood. You are such a fantastic engineer, with great ideas, and great execution. Niki and you are such a warm and friendly couple that we can spend all the weekends with you. Even Neely loves your home. Amin, I may have spent a comparable amount of time in your and my offices purely because I enjoy spending time with you. We had uncountable discussions about politics, football, movies, The Office jokes, preparing op-ed pieces, et al. I hope that we find the opportunity to do it again in the future. You are also a great footballer and I must admit, a professional in FPL. However, I beat you once. You and Yasaman are a great and friendly couple. Rouzbeh, although you came later to the group, but boosted to become an indispensable part of the friendship community. You are so funny that I often cannot say if you are making a joke or not. I am sure your new home will become a nice and warm place for us, next to Arash and Niki (after all that destruction and construction). Hamid, you are a great and hard-working scientist and kind person and I am pleased to know you. I am looking forward to meeting you again. Arnab, my true Gunner mate, our friendship started so smoothly, that I do not remember the beginning. I enjoyed all our discussions before/after each match and our exciting moments during the last season. Maybe this one is ours; who knows? I want to thank you all for all these remarkable moments and memories.

I must appreciate my paranymphs, Cristina and Juan, for being much more than a colleague and as they were true friends in tough moments. Having you two on my side in my defense is such a nice feeling. Thank you so much also for helping me to arrange some of the things on this day.

Baba and Maman, it is difficult to describe my love for you two. You have always believed in me and encouraged me to thrive and you have supported me with your unconditional love in every decision that I have made. My brother and sister, you have always cared for me and given me priority on yourself since my first day in life. Ali, Fatemeh, Azadeh and Nazanin thank you for supporting me and giving me unlimited love. I am lucky to have such a caring family. Baba Ali and Maman Farah, you are so supportive and kind and always make me feel proud. I love you so much and I am very grateful to have you and for your endless help. Without the support and inspiration that you all gave me, I might not be the person I am today.

I would like to thank Neely, who follows me wherever I go in the house, and misses me if I am not around. Unbelievably, he tries to care more if I am not feeling well. He always makes me smile with his cute face and acts.

I kept the last words in this thesis to express my gratitude to the most special one, Mahdokht. With your strong support and encouragement, you were both the engine and fuel for me during this project. You are kind, beautiful and brave. You kept my heart warm and gave me hope whenever I was disappointed, from the very beginning to the end. I could never have completed this work without you and your love. Thanks to you, I learned more about myself as a person and my goals in life. You simply made me grow into a better and more complete person. Thanks a million times.

Curriculum Vitae

Morteza was born on February 10, 1990, in Tabas, Iran. He completed his education at Pouya High School in Tabas before relocating to Tehran to enroll at Sharif University of Technology (SUT). He successfully earned his B.Sc. in Chemical Engineering in 2012, conducting his B.Sc. research project on "Simulation of Polyacrylamide Production Plant in the open-source software (DWSIM)" in the process engineering field. His academic journey continued with an M.Sc. in Chemical Engineering - Environmental Engineering at SUT, where he focused on his thesis, "Experimental study of effective factors on removing heavy metals from oily produced water using iron nanoparticles" under the guidance of Prof. J. Shayegan.

After conclusion of his master's degree in 2014 he started as a researcher at the University of Tehran (UT), Iran. In November 2017, as part of his research pursuit, he became a guest researcher at Eindhoven University of Technology (TU/e) in the Netherlands, concentrating on "Membrane-assisted Chemical Looping Reforming in Elevated Pressure." During this time, he was guided by Prof. R. Sotudeh-Gharebagh, Prof. R. Zarghami, Prof. F. Gallucci, and Prof. M. van Sint Annaland.

In February 2019, Morteza commenced his PhD project within the Multi-scale Modelling of Multiphase Flows group led by prof. dr. ir. Hans Kuipers. His work on the project centered on "Small Molecule Activation" was funded by the Advanced Research Center of Chemical Building Blocks Consortium (ARC-CBBC). He delved into the thermocatalytic decomposition of methane in fluidized bed reactors. The culmination of his research findings is presented in this dissertation. Since July 2023, Morteza has been employed as a process engineer in the Technology team, in the unit of Renewable Chemistries at Avantium in Amsterdam, Netherlands.

Insight into the cover design:

A real photo of the particles extracted from
the experimental fluidized bed reactor.

The poem on the back cover:

Like a river down the valley’s slope,
it meets the rock ahead,
Be fluid in your stride.
No miracles from the lifeless spread,
Live on, stay alive with pride.

Hushang Ebtehaj (Sayeh)

به سان رود که در نشیب دره
سر به سنگ می زند رونده باش
امید هیچ معجزه ای ز مرده
نیست زنده باش

ه.الف.سایه

ISBN: 978-94-6469-577-9